BUOYANCY-INDUCED, COLUMNAR VORTICES WITH APPLICATION TO POWER GENERATION

A Dissertation
Presented to
The Academic Faculty

by

Mark William Simpson

In Partial Fulfillment
of the Requirements for the Degree
Doctor of Philosophy in Mechanical Engineering

Georgia Institute of Technology
December 2015

BUOYANCY-INDUCED, COLUMNAR VORTICES WITH APPLICATION TO POWER GENERATION

Approved by:

Dr. Ari Glezer, Advisor
School of Mechanical Engineering
Georgia Institute of Technology

Dr. Robert X. Black
School of Earth and Atmospheric Sciences
Georgia Institute of Technology

Dr. Marc K. Smith
School of Mechanical Engineering
Georgia Institute of Technology

Dr. Bojan Vukasinovic
School of Mechanical Engineering
Georgia Institute of Technology

Dr. Arne J. Pearlstein
Department of Mechanical Science and Engineering
University of Illinois at Urbana-Champaign

Date Approved: November 11, 2015

Dedicated to my parents,
Bill and Kathy

ACKNOWLEDGEMENTS

I am deeply indebted to my advisor, Professor Ari Glezer. I could not have completed the work presented here without his guidance and teaching throughout our many years together. Thank you, Ari, for continuously pushing me to achieve more, I am truly grateful. I am further indebted to Professor Arne Pearlstein for his attention to detail in assisting with the quality and direction of this work. I would also like to thank the remaining members of my thesis committee Drs. Robert Black, Marc Smith, and Bojan Vukasinovic for their time in helping to guide this research.

To the members of the Fluid Mechanics Research Laboratory, past and present, thank you for the years of camaraderie. From my first day to my last, I have never stopped learning from you. A great deal of this work would not have been possible without the lessons you graciously, and sometimes unknowingly, taught me and for that I cannot thank you enough. In particular, I would like to extend a special thank you to John Kearney who was always a buoy filled with optimism and insight whenever I needed either.

The field investigations were accomplished only through the extraordinary efforts of several people. Specifically, I would like to thank John Culp for the immense amount of time and energy he spent ensuring the success of the testing expeditions. I would also like to thank Ari Glezer and Arne Pearlstein for their assistance during each our many trips into the desert and Abraham Gissen, John Kearney, Thomas Boziuk, and Thomas Lambert for taking time from their own dissertation work to assist in the

construction of the various outdoor facilities. In addition, I would like to thank Dan Haas and DMB Inc. for graciously providing the testing location and facilities in Mesa, AZ.

Portions of this research were made possible with the support of ARPA-E.

TABLE OF CONTENTS

LIST OF FIGURES

SUMMARY

Buoyancy-induced, columnar vortices (dust devils) that are driven by thermal instabilities of ground-heated, stratified air in areas with sufficient insolation convert the potential energy of low-grade heat in the near-surface air layers into a vortex flow with significant kinetic energy. A variant of the naturally-occurring vortex is deliberately triggered and anchored within an azimuthal array of vertical, stator-like flow vanes that form an open-top enclosure and impart tangential momentum to the radially entrained air. The induced flow within the enclosure may be ultimately exploited for power generation by coupling the vortex to a vertical-axis turbine.

The fundamental mechanisms associated with the formation, evolution, and dynamics of an anchored, buoyancy-driven columnar vortex that is formed within such an enclosure over a heated ground-plane are investigated in laboratory experiments. Specific emphasis is placed on the dependence of the vortex cellular structure and vorticity production and sustainment mechanisms on the thermal resources and the magnitude and direction of the entrained flow that is regulated by the flow vanes. Manipulation of vorticity concentrations and advection are exploited in order to modify and optimize the available mechanical energy within the induced flow field and, therefore, the extractable power. Finally, anchored vortices are formed in the natural environment within a scaled field prototype of the flow enclosure using only insolation as the source of buoyancy. These field tests demonstrated formation and sustainment of energetic columnar vortices that enable tapping the gravitational potential energy of the unstable air layers for power generation.

CHAPTER I

INTRODUCTION

1.1 Literature Review

Buoyancy-induced, columnar vortices occur throughout the lowest part of the atmospheric boundary layer as a result of thermal instabilities of ground-heated, stratified air in areas with sufficient insolation. These buoyancy-induced vortices, often referred to as dust devils, effectively convert the low-grade heat available in the air layer over the warm surface into a concentrated fluid motion with significant kinetic energy. Field investigations of naturally-occurring dust devils reported vortices with diameters measuring up to 50 meters, with tangential and vertical wind speeds that can each exceed 50 km/hr (Fitzjarrald 1973; Sinclair 1973; Renno 2004).

While the formation (or triggering) of naturally-occurring dust devil vortices requires a sufficiently large thermal stratification, the considerable kinetic energy contained within the vortex column cannot be accounted for by buoyancy alone (Carroll and Ryan 1970). The axial fluxes of kinetic and thermal energy in the columnar vortex are at least an order of magnitude larger than the corresponding fluxes in nonrotating plumes that form under the same thermal conditions (Kaimal and Businger 1970), and these increases are attributable to the presence of axial vorticity within the vortex core. As noted by Maxworthy (1973), and later by Kanak (2000), naturally-occurring vortices can evolve from spontaneous occurrences of atmospheric, rising plumes that are accompanied by the addition of axial vorticity that becomes

concentrated within the vortex cores and induces rotation about their axes. The production of axial vorticity within dust devil vortices is not well understood. Proposed mechanisms have included concentration of ambient, pre-existing eddies aided by wind shear (Morton 1966), and the tilting of ambient horizontal vorticity by near-surface wind (Maxworthy 1973). However, a number of investigators (Sinclair 1969; Carroll and Ryan 1970; Hess and Spillane 1990) have demonstrated that naturally-occurring dust devils readily form in near-calm conditions. More recent investigations conjectured that the axial vorticity within the vortex column is generated through the tilting of horizontal vorticity produced by the radial entrainment of a nominally-circular buoyant starting plume within the air layer over the heated ground-plane (Kanak et. al. 2000; Kanak 2005) or generated baroclinically within the convective boundary layer due to a combination of thermal stratification and radial pressure gradients induced by atmospheric convective cells (Zhao et al. 2004).

Atmospheric vortices such as tornadoes (Snow 1982; Brady and Szoke 1989; Varaksin et al. 2011; Rotunno 2013) and waterspouts (Renno and Bluestein 2001; Gaya et al. 2001) have been thoroughly investigated. These more intense flows, while similarly scaled and dynamically related, derive their energy from latent heat transfer of the atmosphere and oceans, respectively, and not the sensible heat flux from the sun-heated ground (Hess et al. 1988). Numerical studies (Smith and Leslie 1976; Zhao et al. 2004) and field measurements (Sinclair 1969; Fitzjarrald 1973; Sinclair 1973; Renno 2004) of naturally occurring dust devils have provided significant insight into the structure of the vortex column and the flow dynamics. However, understanding of the vortex formation and sustainment mechanisms (Niino et al. 2006; Ohno and

Takemi 2010) and prediction of the vortex cellular structure and scale (Kurgansky 2006; Pathare et al. 2010) is still scant, and their dependence on the environmental conditions is not well understood (Ryan and Carroll 1970; Kurgansky et al. 2011). Several investigations have sought to determine the dependence of the cross-sectional scale of the vortex (as measured by the diameter of the core) on the global ambient conditions with somewhat mixed results. While Ryan (1972) found good agreement between the magnitude of the thermal gradient in the superadiabatic layer (0.3 m to 10 m) and the distribution of core diameter of dust devil vortices, the more recent investigation of Oke et al. (2007) found no such correlation. In a later investigation, Lorenz (2009) used data from visual surveys and pressure measurements of dust devil vortices to show that the formation density is inversely-correlated with both the near-surface thermal gradient and vortex diameters. On the other hand, Renno and Bluestein (2001) conjecture that the characteristic diameter of atmospheric convective vortices is ultimately governed by the atmospheric vorticity rather than by the distribution of the thermal resources. This assertion is supported by the numerical simulations of Kurgansky (2006) who successfully predicted the size distribution of observed naturally-occurring dust devil vortices in a convectively unstable atmospheric boundary layer using the circulation of the ambient wind velocity. To address these questions, several investigators have modeled the vortex flow with the goal of predicting its strength and scale, and have shown good agreement with existing field measurements (Logan 1971; Smith and Howells 1983a; Fiedler 1998; Renno et al. 1998).

Atmospheric columnar vortices can be classified by a distinctive structural feature that has been referred to as single- or two-cell vortex cores (Mullen and

Maxworthy 1977). In the absence of significant ambient wind, columnar vortices typically form with a single-cell core structure in which upward axial velocity along with nominal solid-body rotation persist throughout the vertical extent of the vortex column (Snow 1982). Interaction with sufficient ambient wind can lead to the formation of a two-cell structure by increasing the axial circulation of the columnar vortex (Rotunno 2013), with downward spiraling axial air motion (downdraft) being induced along the axis of rotation by low pressure along the centerline (Sinclair 1973). This recirculating downdraft cell is bounded from below by the surface-induced upward vortex flow that forms a second, updraft cell that axially engulfs the downdraft cell (Maxworthy 1972). With sufficient axial circulation**,** the downdraft cell can extend to the surface to form a stable, attached two-cell structure (Lugt 1989). Kaimal and Businger (1970) conjectured that the two-cell structure is a general characteristic of well-developed natural dust devils, while Metzger (1999) asserted that the two-cell structure is more likely to form in areas with rough terrain which can alter the pressure along the vortex centerline. The cellular nature of naturally-occurring, dust devil vortices has been recorded in a number of earlier works. Fitzjarrald (1973a) used a stationary setup equipped with cup anemometers to measure the radial distributions of axial velocity in a series of single-cell vortices, while Sinclair (1973) used hotwire anemometry at a number of elevations attached to a mobile boom to measure the axial velocity of dust devil vortices and reported evidence of both single- and two-cell vortex structures. A numerical investigation of naturally occurring dust devil vortices by Zhao et al. (2004) indicated that during the maturation of the vortex core, its cellular structure can evolve between single- and two-cells, given sufficient time and thermal forcing by the heated

ground-plane. The analytical investigation of Fiedler (1998) suggests that the onset of a two-cell vortex structure only occurs in the presence of sufficient ambient angular momentum, and is supported by the later work of Renno (2008) who showed that the two-cell structure readily forms at sufficiently high vortex core swirl numbers.

The present investigation is concerned with a variant of free, naturally-occurring dust devil vortices, and focuses on buoyant columnar vortices that are deliberately triggered and anchored within open-top enclosures formed by azimuthal arrays of flow vanes. The ultimate objective is to provide a thermomechanical link for harvesting low-grade waste heat by coupling the anchored vortex to a vertical-axis turbine (Glezer and Simpson 2014). The power generation concept takes advantage of the self-sustaining mechanisms associated with stationary, buoyancy-driven columnar vortices that convert near-surface thermal energy into significant kinetic energy through an induced radial pressure gradient that produces continued entrainment into the enclosure. The use of natural convection through the triggering of a buoyantly driven columnar vortex has frequently been proposed for a range of scales to convert low-temperature, thermal energy from either solar (Lucier 1981; Zhang et al. 2015) or industrial (Michaud 1999) sources into useful mechanical energy for the renewable production of electric power (Jacobs and Lasier 1984). In common to each of these power generation methods is the generation of a stationary vortex for the production of renewable electricity.

Controlled laboratory experiments in the absence of ambient wind have yielded significant insight into the structure of anchored tornado-like (i.e., isothermal) columnar vortices. These types of vortices are typically formed by using induced suction above the formation volume (although the pressure distribution in the flow is limited by the suction

source), while regulating the rate of radial entrainment of ambient air around its periphery. Ward (1972) used this approach to investigate an isolated columnar vortex, and varied the magnitude and direction of the entrainment velocity using an azimuthal array of vertical adjustable flat vanes. He demonstrated control of the axial penetration of the reverse axial flow through variations in circulation of the entrained flow and noted that downdraft along the vortex centerline was more prevalent at large vane angles (relative to the radius). The cellular structure of columnar vortices was also investigated by Church et al. (1979) and later by Fiedler and Rotunno (1986) using a rotating cylindrical screen to induce axial circulation within an open-top cylindrical volume above a solid ground surface. Fiedler and Rotunno showed that for a given volume flow rate through the facility (induced by suction from above) the cellular structure depends on a horizontal swirl number that measures the ratio of the tangential (v) and radial (u) velocity components of the entrainment into the enclosure (cf. Chapter 6). For sufficiently low v/u the vortex has a single-cell core and as v/u is increased a two-cell vortex forms and has opposite direction axial velocity along the axis of rotation. Tornado-like columnar vortices within a rotating cylindrical boundary were also investigated numerically by Nolan and Farrell (1999) who prescribed v/u in their simulations and confirmed the dependence of the cellular structure on this horizontal swirl ratio. Using numerical simulations of the experiments Ward (1972), Harlow and Stein (1974) demonstrated that sufficiently high axial circulations induced by either large vane angles or axial momentum flux led to downdraft and the formation of a two-cell structure. Both formation parameters regulate the radial entrainment into the enclosure and affect resistance across the array of vanes, which alters the pressure field of the

induced flow field. Several additional investigators have modeled a columnar vortex flow with the goal of predicting the mechanistic triggering of the cellular structure for single- (Barcilon 1967a; Barcilon 1967b; Logan 1971) and two-cell (Kuo 1966; Bellamy-Knights 1970; Kendall 1978) vortices and showed good agreement with existing field measurements.

The flow field induced beneath a columnar vortex formed above a horizontal, rigid boundary has been investigated in a number of theoretical studies (Barcilon 1967a; Barcilon 1967b; Carrier et al. 1971). Rotunno (1980) modeled the convective swirling boundary layer, prescribing vorticity only in the boundary layer upstream of the vortex core and reproduced the outer flow and boundary layer obtained in previous numerical investigations with good agreement. The characteristic features of the near-surface flow of a columnar vortex induced by suction from above were investigated experimentally by Baker (1981), including the development and growth of the spiraling momentum boundary layer that supplies the vortex core with mass and vorticity. The pressure field and surface pressure distributions induced by the swirling boundary layer were measured in a similar experimental apparatus by Greely et al. (2003) with particular emphasis on the strength of the central stagnation point and its role in the vertical advection of axial momentum into the vortex column. Control of the characteristic scales and vorticity production of the induced vortex through regulation of the ground-plane radial entrainment has been contemplated in several previous investigations (Davies-Jones 1973, Church et. al 1977). In their experimental study, Church et al. (1979) demonstrated the evolution of a suction vortex from a single-cell columnar structure into to a multi-vortex formation within the core region through

adjustments to the horizontal swirl ratio of the radial entrainment within the momentum boundary layer. Their investigation demonstrates the coupling between the geometry of the azimuthal vane array and the complex pressure and vorticity fields that can be induced within the flow.

Manipulation of the swirling momentum and thermal boundary layers to affect the structure and strength of the columnar vortex aloft has been examined in a limited number of studies. In a suction-induced experiment, Dessens (1972) demonstrated an increase in the magnitude of the core updraft velocity and core Reynolds number by increasing the surface roughness of the ground-plane normal to the vortex axis of rotation and, therefore, the production of horizontal vorticity within the momentum boundary layer. In a later experimental study of the same design, Neakrase and Greely (2010) considered the effects of surface roughness on the formation of suction-induced columnar vortices, and showed that amplification of the surface roughness led to increased vortex size and decreased tangential velocity. Numerical investigations of concentrated vortices formed above a solid surface have demonstrated significant control over the size and structure through adjustments to the friction imposed along the lower boundary (Bode et al. 1975; Bode and Smith 1975; Smith and Howells 1983b). Bode et al. (1975) demonstrated that the meridional and axial circulations of the induced vortex are increasing and decreasing functions of surface friction, respectively, and a balance between the axial and azimuthal kinetic energies is adjusted through the drag affected by the ground-plane on the momentum boundary layer.

Several laboratory investigations of anchored, buoyancy driven columnar vortices have been conducted and yielded considerable insight into their structure. In these

investigations, the vortices are formed in the absence of ambient wind within a cylindrical volume over a heated surface that is open at the top and is azimuthally bounded by a stator-like array of flow vanes to impart tangential momentum to the entrained ambient air (Fitzjarrald 1973, Mullen and Maxworthy 1977). Fitzjarrald (1973) used such a setup to measure distributions of the tangential velocity and temperature within the enclosure, and observed that adjustments to the angle of the flow vanes also resulted in the formation of negative axial velocity along the vortex centerline. In a later study, Mullen and Maxworthy (1977) measured distributions of the temperature and tangential velocity outside of the core of the columnar vortex and used smoke visualization to show details of the formation and structure of single- and two-cell vortex cores depending on the angle of the surrounding stator-like array.

1.2 Thesis Objectives and Overview

Although naturally-occurring and anchored buoyancy-induced vortices have been the subject of several earlier investigations, the fundamental mechanisms that govern their formation, as well as the importance of and sensitivity to formation parameters such as the thermal forcing by the heated ground-plane and regulation of radial entrainment, are not fully understood. As noted already, current knowledge is pieced together from sparse field investigations of naturally-occurring vortices, and a few earlier laboratory investigations that were limited by the diagnostic tools that were available at the time. Therefore, the overarching goals of the present experimental investigation are to elucidate and characterize in detail the flow and formation mechanisms of buoyantly driven columnar vortices in a laboratory setting, and to further understanding of the conversion of thermal to kinetic energy within the induced flow

field. With these goals in mind, the primary objectives of this thesis are to: ***i.*** Explore the flow mechanisms that lead to the formation of a single-cell columnar vortex in a controlled laboratory environment with specific emphasis on vorticity dynamics and on key features of the vortex structure and flow field, ***ii.*** Understand the mechanisms and boundary conditions that affect the sustainment of the cellular structure in the stable, single- and attached two-cell limits, ***iii.*** Modify the ground-plane boundary layer to control vorticity redistribution within the vortex and thereby intensify its volumetric flow rate and mechanical energy, and ***iv.*** Explore the proposed thermomechanical link in field tests of anchored vortices driven by insolation-induced buoyancy.

As in most laboratory investigations of atmospheric flows, the present laboratory experiments clearly cannot capture the characteristic formation parameters of natural vortices. Rather, they are designed to isolate crucial aspects of the formation and vorticity dynamics of the natural vortices in an experimental setup that mimics the salient large-scale features and dynamics of the atmospheric flows (e.g., Morton 1966; Cermak and Arya 1970; Maxworthy 1981). While the time-averaged three-dimensional flow and temperature fields of the anchored vortex are measured in detail [using high resolution stereo-particle image velocimetry (SPIV) and thermocouple thermometry, cf. Chapter 3] it is noted that the unsteady evolution of the flow makes it virtually impossible to distinguish between inherent large- and small- (turbulent) scale fluctuations in these data.

An overview of the cellular structure of the columnar vortex and its dependence on the formation parameters is discussed in Chapter 4. Using a similarity analysis of the flow within the vortex column (Chapter 2), the structure, dynamics, and distribution of

momenta and kinetic energy flux of the inner and outer flow domains of the vortex column are described. Based on this similarity analysis, the updraft flow field of single-cell vortices is investigated in Chapter 5, where vortex sustainment mechanisms based on analysis of its vorticity dynamics are also discussed. Two-cell structural changes that are brought about by the appearance of a downdraft flow cell along the vortex core including the vorticity dynamics and similarity characteristics are discussed in Chapter 6. Manipulation and redistribution of vorticity concentrations and advection are exploited for increasing the flow rate through, and the available mechanical energy within, the induced flow field, and the resulting structural changes to the flow field are described in Chapter 7. Finally, Chapter 8 reports how the knowledge gained in the laboratory experiments is used to demonstrate formation and sustainment of an anchored columnar vortex in the natural environment using only insolation as the source of buoyancy.

CHAPTER II

DIMENSIONAL CONSIDERATIONS

The three-dimensional flow field of a stationary, columnar vortex (Mullen and Maxworthy 1977) that forms above a heated surface within an enclosure bounded by an azimuthal array of stator-like vertical flow vanes consists of three primary, coupled domains (Figure 2.1): ***i.*** Spiraling momentum and surface thermal boundary layers that advect heated air and vorticity into the core of the columnar vortex; ***ii.*** an inner, thermally-driven vertical vortex core; and ***iii.*** an outer annular flow that is bounded by a helical shear layer and the vanes along its inner and outer edges, respectively, and by the spiraling boundary layer from below. Entrained, surface-heated ambient air within and above the boundary layer sustains the vortex and acquires tangential momentum as it passes through the angled vanes. As conjectured by Rotunno (1980), the spiraling wall boundary layer that is entrained through the azimuthal array of vanes concentrates horizontal vorticity into an initial thermal plume, where it is buoyantly tilted vertically to form the axial vorticity within the core of a columnar vortex. Once rotation begins, the columnar vortex is strengthened and sustained by the generation of additional radial vorticity within the boundary layer that is continuously advected towards the centerline and tilted axially by the buoyancy-driven air motions. This formation mechanism requires only sufficient surface heating to trigger the buoyant instability, without the need for ambient eddies or wind shear, and is sustained as long as heating continues.

The flow domain is described using cylindrical coordinates (r, θ, z) such that the z-axis is coincident with the centerline of the columnar vortex, and the corresponding velocity field is denoted by (u, v, w). Using the Boussinesq approximation, variations in fluid properties due to temperature are assumed to be small and are neglected, except when they contribute to buoyancy effects. Following the formulation of Rajaratnam (1976) for a free axisymmetric swirling jet, the axisymmetric continuity and radial and axial momentum equations that describe the vertical flow near the centerline and sufficiently far from the ground-plane are given by:

$$\frac{\partial(ru)}{\partial r} + \frac{\partial(rw)}{\partial z} = 0 \tag{2.1}$$

$$\frac{v^2}{r} = \frac{1}{\rho}\frac{\partial p}{\partial r} \tag{2.2}$$

$$u\frac{\partial w}{\partial r} + w\frac{\partial w}{\partial z} = -\frac{1}{\rho}\frac{\partial p}{\partial z} + g' + \frac{1}{\rho r}\frac{\partial(r\tau_{rz})}{\partial r} \tag{2.3}$$

with the addition of the adjusted gravitational acceleration or weight deficiency, $g' = \frac{\rho_\infty - \rho(r,z)}{\rho_\infty} g$ (ρ_∞ is the ambient air density and constant) to account for the effects of buoyancy (Turner 1973), and $\tau_{rz} = \mu\frac{\partial w}{\partial r}$ is the shear stress.

The axial momentum equation (2.3) can be rewritten following the steps included in Appendix A to produce

$$\frac{d}{dz}\int_0^\infty (\rho w^2 + p) r dr = \int_0^\infty \rho g' r dr. \tag{2.4}$$

From the radial momentum equation (2.2) the pressure term in equation (2.4) can be rewritten in terms of the tangential velocity using the boundary conditions $\frac{\partial p}{\partial z}(r \to \infty, z) = 0$ and $\frac{\partial p}{\partial z}(0, z)$ is finite,

$$\int_0^\infty \frac{\partial p}{\partial z} r dr = \left|\frac{r^2}{2}\frac{\partial p}{\partial z}\right|_0^\infty - \int_0^\infty \frac{r^2}{2}\frac{\partial}{\partial r}\left(\frac{\partial p}{\partial z}\right) dr = -\int_0^\infty \frac{r^2}{2}\frac{\partial}{\partial z}\frac{\partial p}{\partial r} dr = -\int_0^\infty \frac{r^2}{2}\frac{\partial}{\partial z}\left(\frac{\rho v^2}{r}\right) dr \tag{2.5}$$

and the axial momentum within the vortex column becomes

$$\frac{d}{dz}\int_0^\infty \rho\left(w^2 - \frac{1}{2}v^2\right) r dr = \int_0^\infty \rho g' r dr. \tag{2.6}$$

Equation (2.6) shows that the axial momentum flux along the vortex core varies as long as local temperature differences result in a nonzero weight deficiency, g'. Since the integrand of the integral on the right-hand side of equation (2.6) is positive definite, it follows that, in the absence of viscous effects, the axial momentum flux must increase in the vertical direction.

As the vortex structure evolves above the heated surface, the formation of a helical shear layer between the thermally-driven core (*ii*) and the outer flow (*iii*) results in radial entrainment of ambient air into the vortex column. Following the approach formulated by Morton et al. (1956) for thermal plumes, the entrainment process can be modeled in terms of a mean horizontal inflow on time scales larger than the eddy turnover time, and well above the ground-plane boundary layer, the entrainment rate at the edge of the vortex core is taken to be proportional to a characteristic vertical velocity, $u_e = \alpha\overline{w}$, at a fixed height from the surface. This corresponds to assuming that the radial distribution of the axial velocity is characterized by the radius of the vortex core R (cf. Figure 2.1). Using this relationship, the continuity equation (2.1) defines a ray that coincides with the edge of the vortex core and emanates from an imaginary source beneath the heated surface along which

$$\frac{R}{z} \sim \left.\frac{u_e}{\overline{w}}\right|_{r=R} = \alpha \tag{2.7}$$

where the entrainment coefficient, α, (Taylor 1945) is proportional to the rate of entrainment of ambient air at the edge of vortex core. In the analysis of thermal plumes and jets, this coefficient is ubiquitous for quantifying radial entrainment (Turner 1962;

Turner 1969; van den Bremer and Hunt 2014). Equation (2.7) indicates that the radial extent of the vortex core is linearly proportional to elevation and this proportionality is used to define dimensionless similarity coordinates for the vortex flow.

The buoyantly-induced, columnar vortex can be thought of as a superposition of a momentum-driven swirling jet and a nonrotating thermal plume, and therefore it stands to reason that the flow field of the anchored vortex should also demonstrate axial similarity. The dependence of the velocity and weight deficiency distributions on the similarity variables $\eta = r/R$ and $\zeta = \alpha z/R$ above the boundary layer (demonstrated experimentally in Chapter 5) allows these distributions to be written as

$$\begin{aligned} w(r/R, \alpha z/R) &= w(1, \zeta) f(\eta) \\ v(r/R, \alpha z/R) &= v(1, \zeta) h(\eta) \\ g'(r/R, \alpha z/R) &= g'(0, \zeta) m(\eta) \end{aligned} \tag{2.8}$$

where $R(z)$ is the radial location at which the tangential velocity has a maximum, varies with elevation, and denotes the characteristic radius of the vortex core. The radial and axial velocities are scaled by their respective maximum values at $\eta = 1$ ($r = R$), and the weight deficiency is scaled by its value at the vortex centerline ($\eta = 0$). As noted above, the radial variations of $f(\eta)$, $h(\eta)$, and $m(\eta)$ are obtained experimentally. The axial momentum equation (2.6) can be rewritten in similarity form using equation (2.8) as

$$\frac{\alpha}{R}\frac{d}{d\zeta}\int_0^\infty \rho[w(1,\zeta)^2 f(\eta)^2 - \frac{1}{2} v(1, \zeta)^2 h(\eta)^2] R^2 \eta d\eta = \int_0^\infty \rho g'(0, \zeta) m(\eta) R^2 \eta d\eta. \tag{2.9}$$

At each axial elevation, the coefficients of the similarity parameters are invariant and the axial momentum equation (2.9) can be written for a specific elevation $\zeta = Z$ as

$$\frac{d}{d\zeta}\int_0^\infty [2f(\eta)^2 - S(Z)^2 h(\eta)^2] \eta d\eta = [Fr(Z)]^{-2} \int_0^\infty m(\eta) \eta d\eta, \tag{2.10}$$

where the swirl number $S(Z) = v(1,Z)/w(1,Z)$ is the ratio of the tangential and axial velocity components at the core radius, and $Fr(Z) = [\alpha \cdot w^2(1,Z)/2g' \cdot R(Z)]^{1/2}$ is an adjusted Froude number that measures the ratio of the axial kinetic energy to the buoyant, gravitational potential energy in the buoyantly-driven flow. In the two limits: $Fr = 0$ when $w = 0$ characterizes stratified but motionless fluid, and $Fr \rightarrow \infty$ when the flow is purely momentum-driven. In the latter limit, equation (2.10) describes the flow of an isothermal, swirling jet. The tangential velocity at $\eta = 1$ ($r = R$) can be expressed in terms of the angular velocity of the solid-body rotation of the vortex core, Ω, so the swirl number is rewritten as $S(Z) = \Omega R/w(1,Z)$. In the present investigation, the vortex strength is described by the core Reynolds number, $Re = \Gamma_z/(2\pi\nu)$ where Γ_z is the axial circulation of the vortex column obtained from PIV measurements (cf. Chapter 3) and ν is the kinematic viscosity.

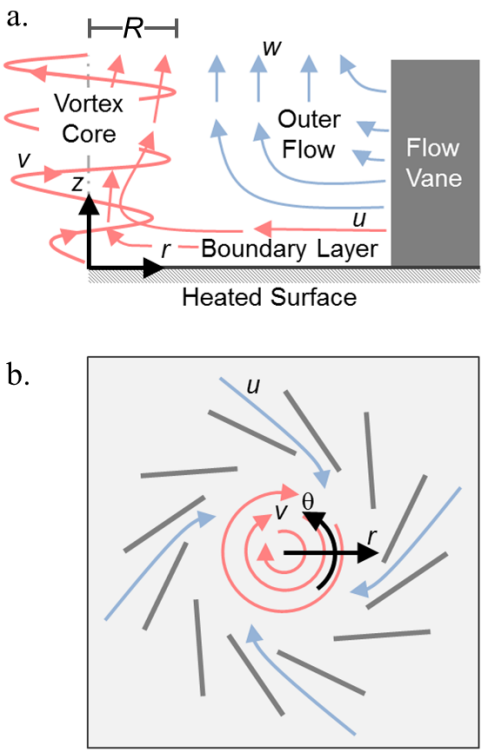

FIGURE 2.1. Schematic representation of the location of the three primary domains of the buoyancy-induced flow field in the (*a*) *r*-*z* and (*b*) *r*-θ planes with experimental coordinate frame (r, θ, z) and velocity field (u, v, w).

CHAPTER III

EXPERIMENTAL METHODOLOGY

3.1 Anchored Buoyancy-Induced, Columnar Vortex Facilities

The present laboratory experiments are designed to elucidate the dynamics and characterize the formation of a buoyant columnar vortex that is deliberately formed and anchored within an open-top cylindrical enclosure over a heated ground-plane. The cylindrical enclosure is azimuthally bounded by an array of vertical, stator-like flow vanes that regulate the magnitude and direction of the radially entrained flow and, therefore, its tangential momentum. The primary formation parameters (i.e., the Grashof number Gr and, for a given vane geometry, the entrainment angle φ) affect the balance between the axial pressure variation (affected by the radial pressure gradient of the rotating flow) and the buoyancy force.

The present investigations were completed using two similar laboratory facilities: 1-m and 3.7-m scale heated surfaces. Each facility includes a smooth horizontal aluminum ground-plane that is heated from below by a resistance heater. Located atop of the heated surface is a regularly-space array of planar azimuthal flow vanes which induce the formation of the anchored, columnar vortex. The individual details of each facility are detailed in this section.

1 m Scale Laboratory Facility

The primary laboratory investigations of the formation and evolution of a stationary (anchored) buoyancy-driven columnar vortex were conducted in a meter-scale

facility (Figure 3.1). The vortex is centered above the heated ground-plane and the flow is described using a cylindrical (r, θ, z) coordinate system as shown in Figure 2.1. The z-axis coincides with the centerline of the column vortex, as shown in Figure 3.1c. Ground heating is simulated by a planar circular ($0.66\ \mathrm{m}^2$) 4.8 kW controllable silicon-rubber resistance heater that is attached to the bottom surface of a 2 cm thick square aluminum plate measuring $L_p = 1$ m on the side. The heater is affixed to the underside of the heated surface using a silicone heat-sink compound and insulated from below by a 3 cm thick slab of mineral wool.

The set temperature of the heated ground-plane T_p is monitored at the center of the plate (r = 0) and is kept steady by using a PID controller (Watlow Series 96 temperature controller) to regulate the power to the heater. The surface temperature distribution can be monitored using an array of thermocouple sensors embedded within the aluminum plate 1 mm below the surface, and once the center temperature is stable, the spatial variation of the surface temperature is less than 3% of the set point within the azimuthal vane array. Therefore, the ground-plane is approximated as a constant temperature surface. The ambient air temperature in the room is controlled by the laboratory ventilation system. The nominally-steady entrained air flow above the heated ground-plane is heated by mixed natural and forced convection. Natural convection is characterized by the Grashof number $Gr = g\beta\left(T_p - T_\infty\right)L^3/\upsilon^2$ where β is the coefficient of thermal expansion, $L = A/P = L_p/4$ is the hydraulic diameter of the surface, and the fluid properties (e.g., the kinetic viscosity ν) are calculated at $T_{film} = (T_p + T_\infty)/2$ (e.g., $Gr = 9.7 \cdot 10^7$ for $T_p = 100^\circ$C). Forced convection within the boundary layer over a constant temperature heated surface depends on the local Reynold number of the radial

entrainment into the vortex core. The respective relative magnitudes of the free and forced convective heat transfer over a constant temperature surface can be estimated by the ratio $Gr/Re_x^2(r)$ (Kays *et. al*, 2005). The boundary layer Reynolds number $Re_x = \bar{U}_e \Delta r/\nu$ at the entrance to the azimuthal vanes ($r/R_i = 1$) is estimated from the average velocity across the boundary layer thickness δ, $\bar{U}_e = Q/2\pi r\delta$ where $Q = 2\pi \int_0^\delta urdz$ is the volume flow rate of the near-surface air layer into the vortex core computed from PIV measurements (cf. Chapter 5). For $T_p = 100°C$ and $\varphi = 30°$, $\delta = 1.2$ cm and $Q = 3.9 \cdot 10^{-4}$ kg/s yielding $Re_x \approx 330$ at $r/R_i = 1$. At the entrance of the azimuthal vane array $Gr/Re_x^2 = 875$ and natural convection is the dominant heat transfer mode. Therefore, the Grashof number adequately characterizes the available thermal resources and is used through the present investigation to describe the thermal characteristics of the experimental facility.

The surface temperature, T_p, is adjustable from ambient to 150°C producing a maximum Grashof number of $11.6 \cdot 10^7$. The rising air is captured using an adjustable laminar-flow hood (2 m x 2 m) located 2 m above the heated surface (Figure 3.1b). Disturbances to the anchored vortex flow are minimized through controlling the axial flow rate through the hood by adjustments to the plenum pressure. The entrained flow is directed through an array of twelve adjustable vanes distributed azimuthally around the center of the plate. Each vane is hinged 45 cm from the centerline of the heated surface, and imparts angular momentum to the air flow that is entrained by the central, buoyancy-driven vortex. Smoke visualization of the self-sustained vortex core is shown in Figure 3.1c. To provide optical access to the internal volume of the enclosure, select vanes are replaced with 1.6 mm thick optically clear glass (cf. Figure 3.5i).

3.7 m scale laboratory facility

Additional investigations are conducted atop of a planar square (13.5 m^2) heated surface (Figure 3.2a) constructed from a 3 x 3 array of 2 cm thick, 1.22 m-square aluminum plates. Ground heating is supplied by a 3 x 3 array of planar square (1.4 m^2) 5 kW controllable silicone rubber heaters attached to the underside of each individual plate using silicone heat-sink compound and insulated from below by a 3 cm thick slab of mineral wool. Power delivered to the heated surface is regulated using on-off controllers (Solo 4824 temperature controller) based on the embedded temperature measurements (1.0 mm depth from the surface at the center of each plate) and the surface temperature of each plate is monitored and controlled individually. The ambient air temperature T_∞ is controlled using the laboratory ventilation system. The surface temperature, T_p, is adjustable from ambient to 100°C, producing a maximum Grashof number of $43 \cdot 10^8$. The azimuthal array contains twelve adjustable vanes that are equally spaced around the center of the plate and hinged at a radius of 83 cm. Half of the azimuthally distributed vanes are constructed from optically clear glass. Smoke visualization of the self-sustained (baseline) anchored vortex is demonstrated in Figure 3.2b.

3.2 Vane Geometry

The geometry of the vane array is set such that the facility has a 12-fold symmetry about the centerline axis. Each vane (1.5 mm thick) is attached to and allowed to pivot about a vertical post (6 mm and 19 mm in diameter for the 1-m and 3.7-m scale facilities, respectively) extending from, and normal to, the heated surface. The aspect ratio of each vane is its length l (defined as the distance from the pivot location to the inner vertical edge, namely 35 cm and 65 cm for the 1 m and 3.7 m scale facilities, respectively)

divided by the height h from the heated surface to the upper horizontal edge (Figure 3.3a). The volume of the enclosure is defined by the height of the vane array h (0.6 m and 0.9 m for the 1 m and 3.7 m scale facilities, respectively) and the internal diameter of the enclosure D_i, defined as the distance been the inner vertical edges of diametrical opposite vanes. The vane angle is defined relative to the radial direction and can vary in the range $0° < \varphi < 60°$. The combination of these parameters defines a horizontal spacing s between neighboring vanes extending perpendicular from one vane to the inner vertical edge of the counterclockwise adjacent vane (cf. Figure 3.3a). For a given vane geometry, D_i and s are also affected by variations in φ.

In addition to the prismatic array shown schematically in Figure 3.3a (hereafter referred to as the baseline geometric configuration), a hybrid-type vane geometry is constructed and examined in Chapter 7. The hybrid geometry consists of into two vertical tiers (each with thickness 1.5 mm). The upper vane and a lower vane have a common pivot location (Figure 3.3b). The lower-tier vanes of length l_h and height h_h are designed to extend radially into the enclosure volume formed by the upper-tier such that their angle φ_h (defined from the radial inward direction) is less than φ creating an enclosure diameter $D_h < D_i$ (Figure 3.3b). Above an elevation h_h, the upper vanes are geometrically identical to the baseline case. Geometric adjustments are made to the lower-tier ($0 < z < h_h$) to affect changes to the flow field.

3.3 Diagnostics and Data Acquisition

Stereo particle image velocity, in horizontal (x-y; r-θ) and vertical (x-z; r-z) measurement planes, is used to investigate the three-dimensional flow field induced within the azimuthal array of flow vanes. These high-resolution measurements are

augmented through temperature data recorded by rakes of thermocouples. The following sections are a description of the diagnostic equipment and post-processing procedures.

Temperature Measurements

Radial temperature distributions in the core of the vortex and outer flow are measured at multiple elevations using a rake of 16 type-T (copper-constantan) thermocouple sensors, spaced 1 cm apart for $r \leq 8$ cm and 2 cm apart for $r > 8$ cm (Figure 3.4a). The rake is constructed from airfoil-shaped stainless steel tubing (chord = 19 mm, max thickness = 9.5 mm) and the thermocouple bead protrudes from a 19 mm long (1.6 mm diameter) circular, stainless steel tube which projects from the leading edge of the airfoil. The most inner thermocouple is aligned such that its location corresponds to the geometric center of the azimuthal vane array. Boundary layer temperature distributions are measured at multiple radial stations using a vertical rake of eight type-T thermocouple sensors equally-spaced 3 mm apart within $3 \leq z \leq 24$ mm (Figure 3.4b). The body of the vertical rake is constructed using stereolithography (SLA) and the thermocouple bead protrudes from a 19 mm long (1.6 mm diameter) circular, stainless steel tube. High-Alumina ceramic insulation (0.6 mm thick) is affixed to the base of the rake to inhibit thermal conduction from the heated surface to the array of thermocouples. Temperature at points on the ground-plane are measured by thermally adhering a type-T thermocouple to the upper side of the heated surface and ambient temperature, T_∞, is recorded at a distance h above an outer edge of the heated surface. Temperature data is sampled at 1 Hz using a Fluke Hydra 2620 data acquisition unit and time-averaged over 600 samples.

Measurements using Stereo Particle Image Velocimetry

The three-dimensional, time-averaged flow field within the vortex enclosure is measured using high-resolution, low-speed (10 Hz) stereo particle image velocimetry in horizontal (r-θ) and vertical (r-z) planes. Measurements are obtained in the same manner for both facilities. A typical horizontal SPIV configuration is shown schematically in Figure 3.5. A detailed description of the SPIV system and corresponding post-processing are presented in this section.

The SPIV system consists of commercially available LaVision hardware, including two identical 1600 x 1200 pixel, 14-bit CCD cameras, a programmable timing unit, 20 cm x 20 cm calibration plate, and two Scheimpflug adapters. The light sheet is generated by an Nd:YAG laser (Figure 3.5c). Two light sources are used: a Continuum Surelite SL I-20-PIV (160 mJ, 532 nm, 10 Hz repetition frequency) and a Quantel EverGreen 200 (200 mJ, 532 nm, 10 Hz repetition frequency) during the 1 m and 3.7 m scale testing, respectively. The laser beam is reflected to the height of the measurement plane through a series of Nd:YAG laser line mirrors (Figure 3.5d) and the elevation of the light sheet (from the heated surface) is controlled through a mechanical axial traverse (Figure 3.5e). The beam is focused with a convex bi spherical lens (Figure 3.5f, f = 1.5 m) and spread into a 1-2 mm thick light sheet (Figure 3.5h) using a cylindrical lens (Figure 3.5g, f = 25 mm). The cylindrical lens is mounted by rotational stage to provide a horizontal or vertical light sheet depending on its orientation. The light sheet enters into the facility through azimuthal vanes constructed from optically clear glass (Figure 3.5i) illuminating the measurement plane. The remaining vanes and heated

surface are painted matte black to limit laser reflection interference and provide additional contrast between the particles and background.

The CCD cameras (Figure 3.5j) are mounted with overlapping fields of view in an angular displacement configuration on 3-axis gimbals and attached to tripods to allow for elevation adjustments. Each camera is set to a nominal angle of θ_c = 20-35° (depending on the measurements) from the direction normal to the imaging plane in a forward-backward-scattering setup (i.e., the cameras are on the same side of the light sheet). The angular displacement of each camera sensor with respect to the imaging plane is corrected using a Scheimpflug adapter. In the vertical measurement plane configuration, azimuthal vanes on one side of the array are replaced with glass panes to provide optical access for the cameras into the enclosure. Calibration is completed using a two-level gridded calibration target (20 cm x 20 cm with $\Delta x = \Delta y = 2$ cm spacing). A mapped-stereo algorithm using a pin-hole calibration method in LaVision DaVis 8.1 is used to determine image distance from each camera sensor for calculation of the velocity field.

The measurements in a horizontal (x-y; r-θ) plane are acquired using identical 35 mm lenses producing a planar measurement domain of 320 x 241 mm and 560 x 415 mm (denoted by the dashed outline in Figure 3.5) with a spatial resolution of 5 and 3 pixels per mm for the 1 m and 3.7 m scale facilities, respectively. Similarly, the measurements in a vertical (x-z; r-z) plane are acquired using 105 mm lenses producing a planar measurement domain of 90 x 67 mm and spatial resolution of 18 pixels per mm. The ambient flow (outside of the array vanes) is seeded using a glycol-water theatrical fog (Rosco Fog Fluid) so that particles are entrained naturally into the vane enclosure.

SPIV Processing

Velocity data are computed from the PIV images using a commercial algorithm (DaVis 8.1) that uses a standard double-frame FFT cross-correlation method (e.g., Adrian and Westerweel 2011). Sample raw images of the seeded flow field in a horizontal (x-y; r-θ) plane are displayed in Figure 3.6a. Particle contrast in each raw image is enhanced through the subtraction of a seven-image temporal Gaussian average of pixel intensity at each spatial location within the recorded frame. For measurements recorded in the vertical (x-z; r-z) plane, a geometric mask is applied to remove interference associated with laser reflections from the heated surface. Multi-pass processing is completed using four successive correlation passes with incrementally smaller interrogation windows (64 x 64 pixels to 32 x 32 pixels). Each interrogation window is overlapped by 50% and a circular Gaussian weighting function is applied to reduce the error associated with the entrance and exit of particles between frames. Each interrogation window contains particle density of 15-30 particles depending on the SPIV configuration. Before each pass, dewarping and image deformation corrections are applied to correct for image distortion, applying an identical interrogation grid to each camera. The double-frame FFT cross-correlation algorithm is first applied between image pairs from the individual cameras, generating a two-component, in-plane vector field. After each pass, the out-of-plane component is calculated, and vectors deemed spurious from the reconstruction are rejected during subsequent passes. After the final pass, the in-plane velocity field of each camera is used to reconstruct the three-component vector by using a system of four linear equations and three unknowns (u, v, w) to find a vector that distributes the error evenly over all three components

(Calluaud and David 2004). Vector rejection is applied on the instantaneous vector field based on the magnitude of the correlation peak (Q ratio < 3), vector magnitude ($|\vec{V}|$ > 1.5), and local RMS compared to neighboring vector RMS ($\vec{V}'_n > 1.5\vec{V}'_{n+1}$). All PIV data are time-average and include 750 individual image pairs to provide sufficient data to allow temporal convergence at each spatial location. The spatial average of the root-mean-square deviation of pixel displacement, $\frac{1}{\Delta A}\int \sqrt{\frac{1}{n}\sum(\vec{x}')^2}\, dA$, outside of the vortex core (cf. Figure 2.1) where flow fluctuations are reasonably small, is calculated for each measurement plane. The mean deviation of pixel displacement for the measurements included within this investigation is found to be 0.238 pixels corresponding to an average upper bound of 4.43% error in the measured velocity magnitude for the current SPIV configuration and accounts for both inherent flow fluctuations and experimental measurement error.

The vortex core in each horizontal (r-θ) plane is offset relative to the center of the image to extend the radial domain of the measurements (Figure 3.7a). The vortex centerline (r = 0) is located by comparing the velocity magnitude, $|\vec{V}| = (u^2+v^2+w^2)^{1/2}$, which has a local minimum along the vortex centerline (Figure 3.7a), with the second eigenvalue (λ_2) of the symmetric tensor ($\bar{\bar{\Lambda}}^2 + \bar{\bar{\omega}}^2$) where

$$\bar{\bar{\Lambda}} = \tfrac{1}{2}\left[\nabla\vec{V} + \left(\nabla\vec{V}\right)^T\right] \tag{3.1}$$

$$\bar{\bar{\omega}} = \tfrac{1}{2}\left[\nabla\vec{V} - \left(\nabla\vec{V}\right)^T\right] \tag{3.2}$$

are the rate-of-strain and vorticity tensors, respectively, and is minimum at the location of lowest pressure in a two-dimensional plane (Figure 3.7b: the λ_2-criterion, Jeong and Hussain 1995; Haller 2005). The locations of the minima from these calculations are

compared to identify the vortex centerline and the data are mapped from the measurement coordinate frame (x, y) to a polar-grid (r, θ). Radial distributions of the velocity vector, $\vec{V} = (u, v, w)$, are obtained using an azimuthal-average from $-\pi/12$ to $\pi/12$, to account for the twelve-fold symmetry associated with the array of flow vanes. The direction $\theta = 0°$ is prescribed as the azimuthal location which provides the shortest distance between the vortex centerline ($r = 0$) and the right edge of the ground-plane. A sample data slice in the x-y measurement plane is displayed in Figure 3.7c. These data are interpolated onto the r-θ plane (Figure 3.7d) with $\Delta r = \Delta x$ resolution, from which an azimuthal average is calculated to obtain radial distributions (Figure 3.7e). Throughout the thesis, radial distributions obtained from PIV data will be presented as shown in Figure 3.7e.

The time-averaged vorticity components $\omega_z = \frac{1}{r}\left(\frac{\partial(rv)}{\partial r} - \frac{\partial u}{\partial \theta}\right)$ and $\omega_\theta = \left(\frac{\partial u}{\partial z} - \frac{\partial w}{\partial r}\right)$ that are normal to the r-θ and r-z measurement planes, respectively, are calculated before the velocities are mapped to the polar grid using a circulation method at each point (Raffel et al. 2007)

$$\overline{\omega}_{i,j} = \frac{\oint \vec{V} d\vec{l}}{4dxdy} = \frac{\int u_{i,j-1}dx + \int v_{i+1,j}dy - \int u_{i,j+1}dx - \int v_{i-1,j}dy}{4dxdy} \tag{3.3}$$

where dx and dy are the resolution of the SPIV data. Vorticity components which are tangent to the measurement planes [ω_θ and (ω_r, ω_z), for the r-θ and r-z respectively] are calculated using a second-order, central-difference method where azimuthal derivatives are neglected and out-of-plane gradients are calculated using parallel measurement planes when available. The propagation of the error in pixel displacement (due to experimental

error and inherent flow fluctuations) results in a mean error in the calculated vorticity of 10.9% over all flow fields included within this investigation.

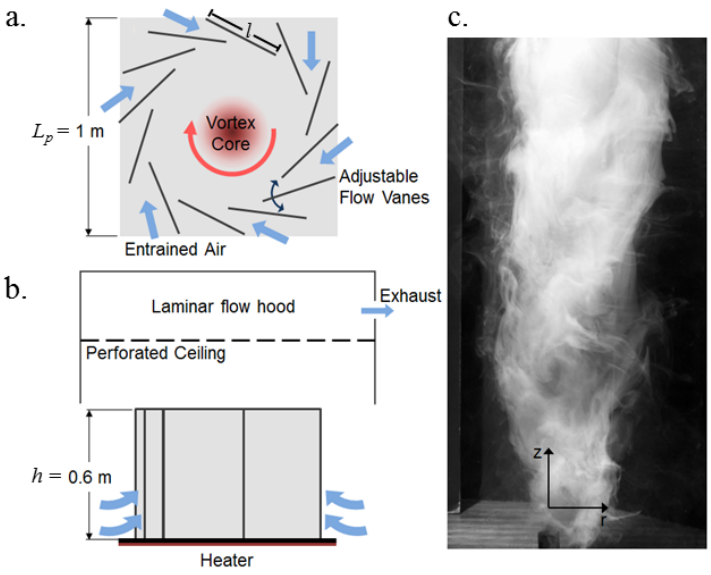

FIGURE 3.1. The 1 m scale buoyancy-induced, columnar vortex facility: (*a*, *b*) top and side views of experimental setup showing heated surface, adjustable azimuthal flow vanes, and laminar flow hood with schematic representation of entrainment and vortex core and (*c*) smoke visualization of the laboratory vortex (the image field of view measures 20 cm x 45 cm).

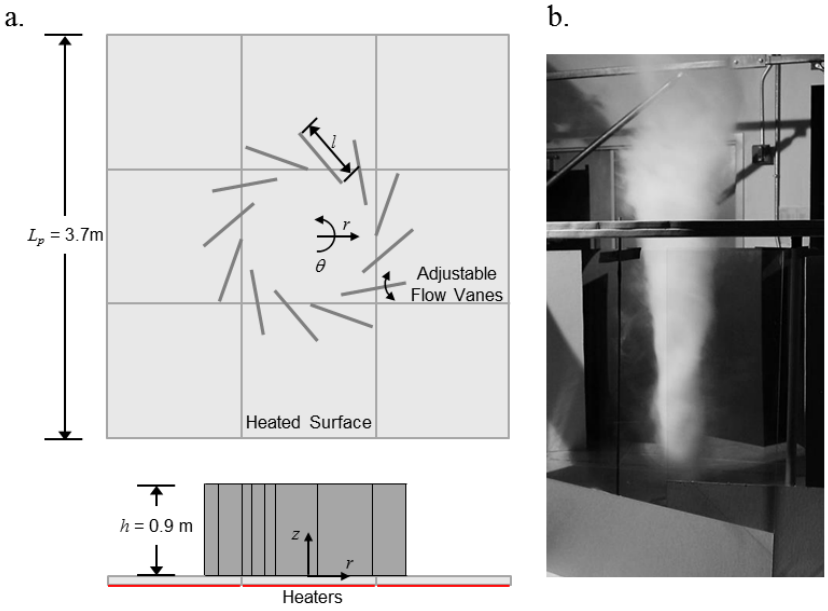

FIGURE 3.2. The 3.7 m scale buoyancy-induced, columnar vortex facility: (*a*) top and side views of experimental setup showing heated surface and adjustable azimuthal flow vanes and (*b*) smoke visualization of the laboratory vortex (the image field of view measures 70 cm x 150 cm).

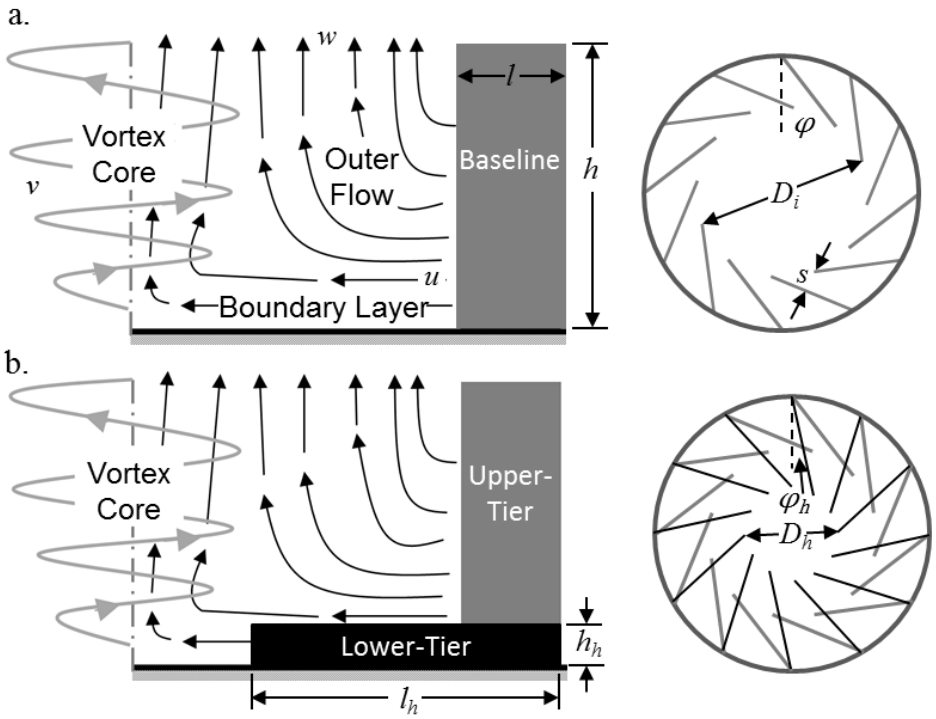

FIGURE 3.3. Schematic representation of the side and top view of the azimuthal array of flow vanes for the (*a*) baseline and (*b*) hybrid vane geometries.

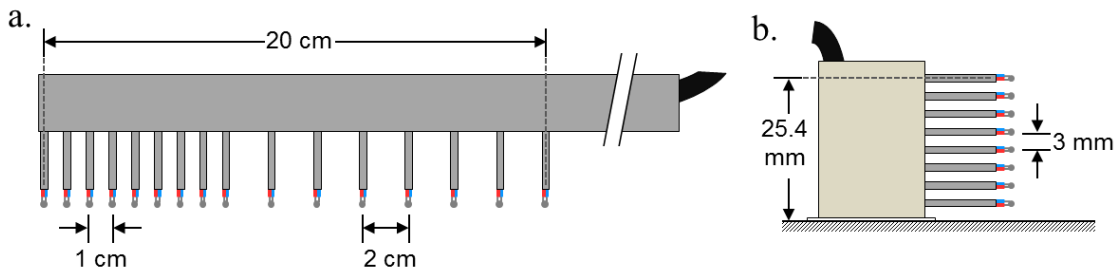

FIGURE 3.4. Schematic of the (*a*) radial (top view) and (*b*) axial (side view) type-T thermocouple rakes.

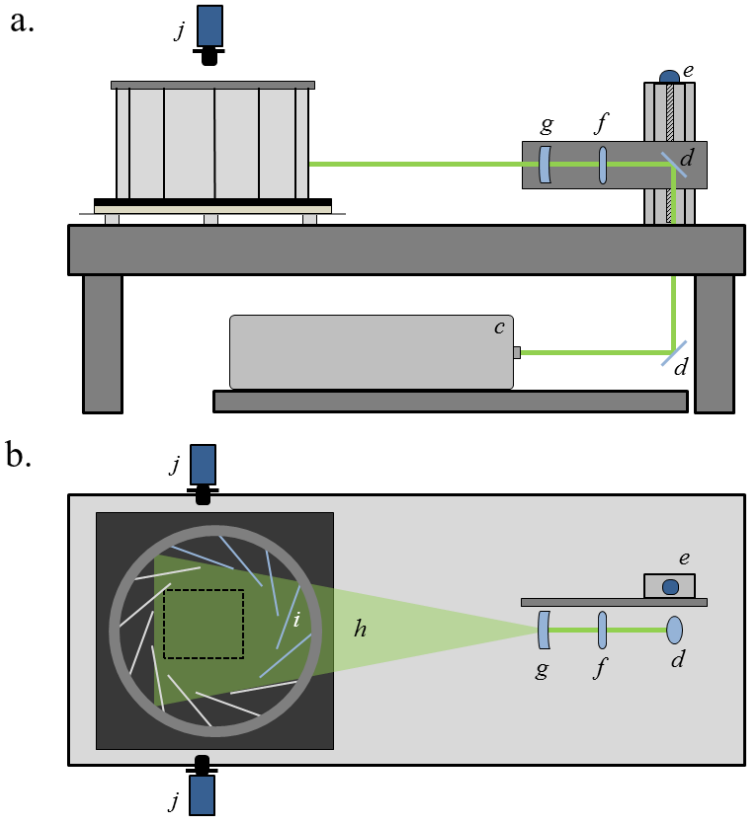

FIGURE 3.5. (*a*) Side and (*b*) top-view of SPIV setup in which light is emitted from an Nd:YAG laser (*c*) and reflected to the elevation of the measurement plane via mirrors (*d*), concentrated by a spherical lens (*f*) and spread by a cylindrical lens (*g*) into the light sheet (*h*). The elevation of the sheet is controlled by a mechanical axial traverse (*e*). The laser light access, as well as optical access from the side for (*r*-*z*) measurements, is provided by optically clear glass vanes (*i*) and images are recorded with two CCD cameras (*j*) suspended above the facility. A typical (*r*-θ) field of view is denoted by the dashed line.

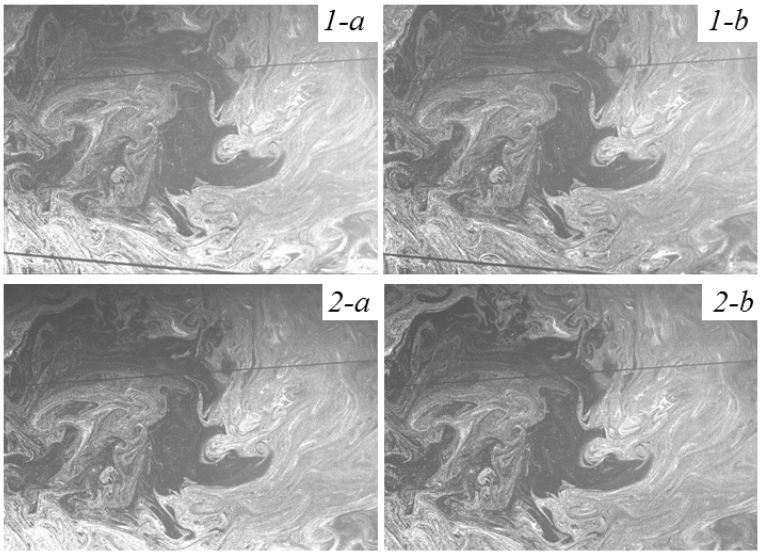

FIGURE 3.6. First (*a*) and second (*b*) frame of a sample raw PIV image displaying particle seeding for SPIV cameras 1 and 2.

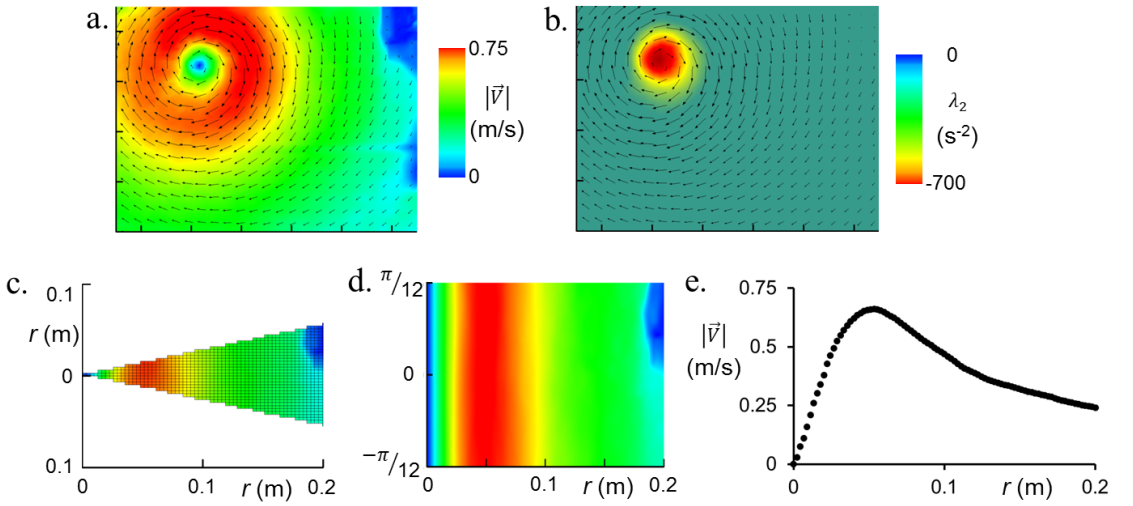

FIGURE 3.7. Color raster plot of (*a*) velocity magnitude and (*b*) λ_2–criterion overlaid with vectors of the in-plane velocity for a representative time-averaged SPIV field. (*c*) π/6-slice of velocity magnitude data in the (*x*-*y*) measurement plane is mapped to (*d*) an (*r*-θ) plane to produce (e) azimuthally-averaged radial profiles.

CHAPTER IV

CELLULAR STRUCTURE OF COLUMNAR VORTICES

The spiraling flow within the vortex core of an isothermal or buoyancy-driven columnar vortex (cf. Figure 2.1) that forms in a nominally quiescent unbounded environment has two stagnation points along the vortex centerline, which characterize the structure of the core (Snow, 1982). The primary stagnation point is located on the surface at the center of the radially-converging, spiraling momentum boundary layer while the secondary ("free") stagnation point appears aloft, where the rising air begins to diverge laterally. The vertical motion that transports the radial surface flow and entrainment to higher elevations through the core of the vortex results from an imbalance between the rotation-induced low pressure along the vortex centerline and a vertical force, such as buoyancy. In the absence of significant circulation over a relatively featureless terrain, atmospheric columnar vortices typically form with a predominantly single-cell core structure in which an updraft cell of positive axial flow persists from the fixed stagnation point on the ground-plane to the free stagnation point far above the near-surface motions (Figure 4.1a). Sufficient axial circulation (e.g., Karstens et al. 2010) or wind shear coupled with complex surface topography (e.g., Metzger 1999) in buoyancy-induced vortices (e.g., dust devils) can modify the flow in the vortex core, and lead to migration of reverse axial flow along the axis of symmetry, accompanied by downward translation of the free stagnation point (Snow 1982). The downdraft along the vortex axis forms a cylindrical cell of spiraling, axially-recirculating flow that is bounded

from below and circumferentially by the updraft cell of the surface-induced vortex flow (Rotunno 2013) and, in the presence of sufficient axial circulation, can descend to the elevation of and attach to the ground-plane, as shown schematically in Figure 4.1b. The appearance of the recirculating downdraft cells has been reported in both naturally-occurring, isothermal (Brandes 1978; Wurman and Gill 2000) and buoyancy-induced (Sinclair 1969 and 1973; Bluestein et al. 2004) columnar vortices.

The formation of the downdraft cell was also observed in several laboratory experiments, where variations in the angular velocity and entrainment were simulated by spinning cylindrical shells (Maxworthy 1972), azimuthal arrays of adjustable vertical vanes (Ward 1972), and surface roughness (Neakrase and Greely 2010). The laboratory experiments with buoyancy-induced, columnar vortices by Fitzjarrald (1973b) and Mullen and Maxworthy (1977), and isothermal, suction-induced columnar vortices by Maxworthy et al. (1985), demonstrated that the elevation of the free stagnation point can be continuously regulated by adjusting the direction and magnitude of the entrained flow until the stagnation point is translated and attaches to the ground-plane (Lugt 1989). In the present investigation, the cellular structure of anchored buoyancy-induced columnar vortices that form over a heated ground-plane are investigated in detail by regulating the entrained flow through adjustments to the azimuthal array of vertical vanes and to the ground-plane heating that induces buoyancy. For a given temperature difference, a single-cell vortex, characterized by a central stagnation point on the surface (*d* in Figure 4.1a) and a free stagnation point above the vane array such that a continuous updraft cell exists throughout the volume of the vane enclosure, is typically formed at low vane angles (with respect to the inward radial direction), for which the tangential

momentum of the entrained flow and pressure drop across the vane array are small. At moderate vane angles, increasing the vane angle increase the angular velocity of the vortex core and the spacing between adjacent vanes decreases, resulting in a larger pressure drop that limits entrainment into the enclosure. Both effects lead to a reduction in the rotation-induced pressure within the core of the vortex and increase the magnitude of the centerline axial pressure gradient. This leads to the formation of a detached two-cell vortex with a recirculating downdraft cell that advects cool air from aloft and a translation of the free stagnation point, located along the axis of rotation at the intersection of the flow surface between the up- and downdraft cells, downwards. Finally, when the vane angle is sufficiently large, the downdraft cell extends to the ground-plane, and the stagnation point that forms on the flow axis between the two cells in the vortex core migrates to the heated surface (*e* in Figure 4.1b) forming an attached two-cell vortex. A bifurcation circle (Perry and Chong 1987, *c*-*c*' in Figure 4.1b) forms at the junction of the flow interface between the recirculating downdraft and updraft cells.

The dependence of the formation of the three core regimes, namely single-cell, detached two-cell, and attached two-cell vortices in the 1 m scale facility (cf. Chapter 3), is mapped at two elevations for a range of vane angles φ ($\varphi = 0$ when the vanes are radial) and Grashof numbers *Gr* using SPIV measurements of the axial velocity along the centerline of the vortex column. The instantaneous axial velocity component along the centerline $w(z, t; r = 0)$ is predominantly upward ($w > 0$) and downward ($w < 0$) in single-cell and two-cell vortices, respectively. Near the elevation of the free-stagnation point for a detached two-cell vortex, *w* changes sign along the axis of symmetry. Figure 4.2a shows a time record of the axial velocity at a fixed elevation above the surface

($z/h = 0.17$) for each of the three flow regimes (this elevation is selected to coincide with the height of the free stagnation point of the detached two-cell vortex) normalized ($\hat{w} = w/\Omega R$) by the angular velocity ($\Omega = 15$ s^{-1}) and core radius ($R = 4.5$ cm) of the single-cell vortex. For single- and attached two-cell vortices, $\hat{w}$ is nearly invariant and $\bar{\hat{w}} = 0.235$ and -0.175 with nominal RMS fluctuations of 0.034 and 0.041, respectively. However, the instantaneous flow in the vicinity of the time-averaged detached two-cell vortex exhibits significant oscillations of the axial velocity $\bar{\hat{w}} = -0.0577$ with an RMS of 0.212 (nearly six times the RMS of the single- and attached two-cell structures).

Maps of the vortex structure in the 1 m scale facility in terms of φ and Gr ($5° < \varphi < 55°$, $4.8 \cdot 10^7 \leq Gr \leq 11.6 \cdot 10^7$) for fixed vane geometry ($l = 0.35$ m, $h = 0.6$ m) using color raster plots of the time-averaged centerline ($r = 0$) axial velocity $\bar{w}$ above the heated surface are shown in Figures 4.2b and c for $z/h = 0.17$ and 0.34, respectively.. At these elevations, the free stagnation point on the interface between the up- and downdraft cells on the centerline is marked by $\bar{w} = 0$ (shown using a dashed contour). When $\bar{w} > 0$, the vortex at this elevation is either single-cell or detached two-cell, while for $\bar{w} < 0$ the vortex is either detached or attached two-cell. These maps show that the induced vortex intensifies with increasing Gr, as is evident by the increase in the magnitude of the up- or downdraft axial velocity for a given vane angle. For a constant Gr, the free stagnation point forms for lower vane angles at higher elevations, indicating that the axial height of the tip of the downdraft cell decreases (or the depth of the cell increases) with increasing φ. At a given elevation, the height of the free stagnation point decreases monotonically with Gr. Detailed investigations at $\varphi = 30°$ and 50° revealed the formation of a single-cell structure throughout the height of the vane array and an attached two-cell

structure, respectively. As vane angle has been shown to influence the cellular structure of the anchored, columnar vortex (Mullen and Maxworthy 1977), it is expected that for all $\varphi \leq 30°$ a single-cell structure (Figure 4.1a) is maintained below the height of the azimuthal vane array and for $\varphi \geq 50°$, an attached two-cell structure is maintained (Figure 4.1b). Therefore, the elevation of the free stagnation point occurs between $0 < z/h < 1$ within the range $30° < \varphi < 50°$, and the vortex core is classified as detached two-cell (Figure 4.2b and c). Corresponding color raster maps of the radial integral of the enthalpy ($\mathcal{H} = 2\pi \int \rho c_p \Delta T r dr$) thermally characterizing the flow field are shown in Figures 4.2d and e. While $\mathcal{H}$ increases with *Gr* for fixed φ, as additional thermal energy is supplied to the induced flow field, $\mathcal{H}$ is also *higher* in the presence of downdraft (larger φ) despite the fact that the downdraft flow is cooler. The increase results from a redistribution of thermal energy to distal locations from the vortex axis, and is due to the confinement of the buoyant flow to the annular updraft cell (cf. Figure 4.1b). Note the net decrease in enthalpy for all φ and *Gr* between $z/h = 0.17$ and 0.34, regardless of the cellular structure, as the air is cooled by entrainment and mixing of cooler air along the helical shear layer between the vortex core and outer flow.

The characteristic structures of a single-cell, detached two-cell, and attached two-cell vortices highlighted in Figure 4.2 ($\varphi = 30°$, 40°, and 50°, respectively, at $Gr = 9.7 \cdot 10^7$) are demonstrated in Figures 4.3a-c using time- and azimuthally averaged (cf. Chapter 3) radial distributions of the tangential and axial velocity components and of the temperature. The axial and tangential velocity components are each normalized by the angular velocity ($\Omega = 15$ s^{-1}) and core radius ($R = 4.5$ cm) of the single-cell vortex at $\varphi = 30°$, $\hat{w}(r/R_i) = w/(\Omega R)_{30°}$ and $\hat{v}(r/R_i) = v/(\Omega R)_{30°}$, and the temperature is scaled

with T_∞ and T_p according to $\hat{T}(r/R_i) = (T - T_\infty)/(T_p - T_\infty)$. These distributions are measured at $z/h = 0.17$ and the internal radius of the vane enclosure for $\varphi = 30°$, 40° and 50° (R_i = 24.6, 28.7, and 33.1 cm, respectively). The distributions of the axial velocity $\hat{w}(r/R_i)$ (Figure 4.3a) show the primary features of the vortex core. For $\varphi = 40°$, $\hat{w}(0) \approx 0$, indicating that the time-averaged stagnation point separating the downdraft and updraft cells is located near $z/h = 0.17$. For a smaller vane angle of $\varphi = 30°$, $\hat{w} > 0$ at all r/R_i, indicating that the vortex has a single-cell structure at this elevation. For a larger vane angle, $\varphi = 50°$, $\hat{w}(0) < 0$ (as discussed for Figure 4.2b, this is an attached two-cell structure). For the attached two-cell structure, the axial velocity reverses sign at $r/R_i = 0.12$, and the downdraft along the vortex centerlines leads to a reduction of the axial velocity and axial momentum flux ($\dot{P}_{50°} = 0.55\dot{P}_{30°}$) throughout the enclosure due to the formation of a helical counter-current shear layer within the recirculating downdraft cell. The radial distributions of the tangential velocity (Figure 4.3b) show that as the downdraft intensifies, the radial spreading of the vortex increases and the core radii (as measured by the location of peak tangential velocity) are $R_{40°} = 1.4R_{30°}$ and $R_{50°} = 2.2R_{30°}$. These data also show that $v(r)$ does not change sign with the reverse axial flow, and that the downdraft and updraft cells have the same sense of rotation, although the angular velocity within the recirculating downdraft cell is lower ($\Omega_{downdraft} = 0.77\Omega_{updraft}$). Despite the significant increase in core radius, it is noteworthy that the maximum tangential velocity remains nominally invariant for each of the representative cellular structures ($\hat{v}_{max,50°} = 1.04\hat{v}_{max,30°}$). The single-cell and detached two-cell vortices have similar radial temperature distributions (Figure 4.3c) but $\hat{T}(r < R_i)$ at $\varphi = 40°$ is nominally 10% larger than at 30°. For the attached two-cell structure, the

downdraft of cool air from aloft reduces the normalized temperature at the centerline and the maximum temperature is shifted radially to $r/R_i \approx 0.2$. However, despite the reduction in temperature within the recirculating downdraft cell, the temperature in the outer flow increases such that the thermal energy within the vane enclosure increases monotonically with azimuthal vane angle (cf. Figures 4.2d and e).

The dependence of the axial vorticity distributions in the horizontal plane (r-θ) on the cellular structure of the vortex core (i.e., single-cell, detached two-cell, or attached two-cell) is investigated at z/h = 0.17 ($Gr = 9.7 \cdot 10^7$). Color raster plots of the time-average axial vorticity concentrations $\hat{\omega}_z$ normalized by the angular velocity of a single-cell vortex at $\varphi = 30°$ ($\Omega = 15$ s^{-1}) and overlaid with radial distributions of time-averaged tangential velocity are shown in Figures 4.4a through c. The rectangular measurement domain measures R_i x $0.5R_i$ and the z axis is located at the origin. It should be noted that as φ increases from 30° to 50°, the inner radius of the enclosure R_i increases from $0.41h$ to $0.55h$ and the size of the measurement domain is enlarged accordingly. The distribution of axial vorticity within the detached two-cell vortex ($\varphi = 40°$) for which the free stagnation point is near the elevation of the measurement plane (z/h = 0.17), is similar to the corresponding distribution within the single-cell vortex. That is a local minimum ($\hat{\omega}_z < 0$) occurs at the vortex centerline, with a monotonic radial decrease in magnitude to zero in the outer flow. However, the magnitude of the axial vorticity on the centerline of the detached two-cell vortex is significantly lower than in the single-cell core ($\hat{\omega}_{z,40°} = 0.46\hat{\omega}_{z,30°}$) as the angular velocity, Ω, decreases with the spreading of the vortex core (cf. Figure 4.3b). As the axial extent (depth) of the downdraft cell increases ($\varphi = 50°$), the magnitude of the axial

vorticity along the centerline continues to decrease ($\hat{\omega}_{z,50^\circ} = 0.31\hat{\omega}_{z,30^\circ}$), as is evident from the annular distribution of $\hat{\omega}_z$ in Figure 4.4c, for which the inner radius $r/R_i = 0.23$ marks the interface between the up- and recirculating downdraft cells of the vortex core (cf. Figure 4.1b). The axial vorticity within the updraft cell of either cellular structure originates from the vertical tilting of near-surface radial vorticity within the swirling momentum boundary layer (Rotunno 1980). Within the vortex core, vortex lines spiral helically and are stretched axially by the buoyantly accelerating flow. The axial vorticity concentrations within the vortex column are tilted radially and azimuthally by the axial gradients of the radial and tangential velocity components, respectively, affected by the radial spreading of the core. These effects are intensified significantly with the increased lateral spreading of the core due to the axial migration of the downdraft cell. As the irrotational fluid within the downdraft cell is drawn from aloft, its rotation is affected by azimuthal shear interaction with the surrounding updraft cell, and axial vorticity diffuses radially into the recirculating flow domain. As a result of the enhanced radial spreading of the vorticity concentrations in the presence of the downdraft cell, the magnitude of the axial vorticity distribution decreases.

Some thermal and flow characteristics that depict the fundamental structural differences between the momentum and thermal boundary layer of single-cell ($\varphi = 30^o$) and attached two-cell vortices ($\varphi = 50^o$) for the *same* temperature difference ($Gr = 9.6 \cdot 10^7$) are shown for reference in color raster plots of normalized temperature distributions [$\hat{T} = (T - T_\infty)/(T_p - T_\infty)$] superposed with velocity vectors (measured using SPIV) in Figures 4.5a and b, respectively. The measurement domain is the *r-z* plane and is bounded from below by the heated ground-plane and on the left by the

vortex axis ($0 < z/h < 0.025$, $0 < r/R_i < 0.8$). In the single-cell vortex (Figure 4.5a), the thermal and momentum boundary layers of the entrained flow (cf. Figure 2.1) spiral towards the centerline, where a central stagnation point forms on the surface at $r/R_i = 0$. The boundary layer flow is turned axially upward near the centerline, and the spiraling updraft cell begins to spread radially near the top edge of the measurement domain. Even though the Grashof number is unchanged, the flow field and temperature distribution within the attached two-cell vortex, $\varphi = 50^o$, are quite different (Figure 4.5b). To begin with, the radial velocity of the entrained flow at a constant r/R_i is higher within the momentum boundary layer ($u(\varphi = 50^o) = 2.3u(\varphi = 30^o)$ at $r/R_i = 0.6$ and $z/h = 0.5 \cdot 10^{-2}$) and the thermal boundary layer along the heated surface is thinner ($\hat{T} = 0.3$ at $r/R_i = 0.6$ for $z/h = 0.98 \cdot 10^{-2}$ and $0.87 \cdot 10^{-2}$ for the single- and attached two-cell, respectively). The presence of the recirculating downdraft cell is evident in the formation of the flow interface between the down- and updraft cells, and is indicated by the dashed projection of the stream surface that originates from the off-axis bifurcation circle at $r/R_i = 0.16$. The flows within the updraft and outer downdraft cells turn axially upward along this flow interface. The two streams mix in the vicinity of the bifurcation circle (cf. c-c' in Figure 4.1b), and the heated fluid is driven by buoyancy along the flow interface between the cells. The temperature distributions show the presence of cooler fluid, both within the downdraft cell and in the outer flow above the thermal boundary layer. The structure of single- and two-cell vortices and their dependence on the formation parameters are discussed in more detail in Chapters 5 and 6, respectively.

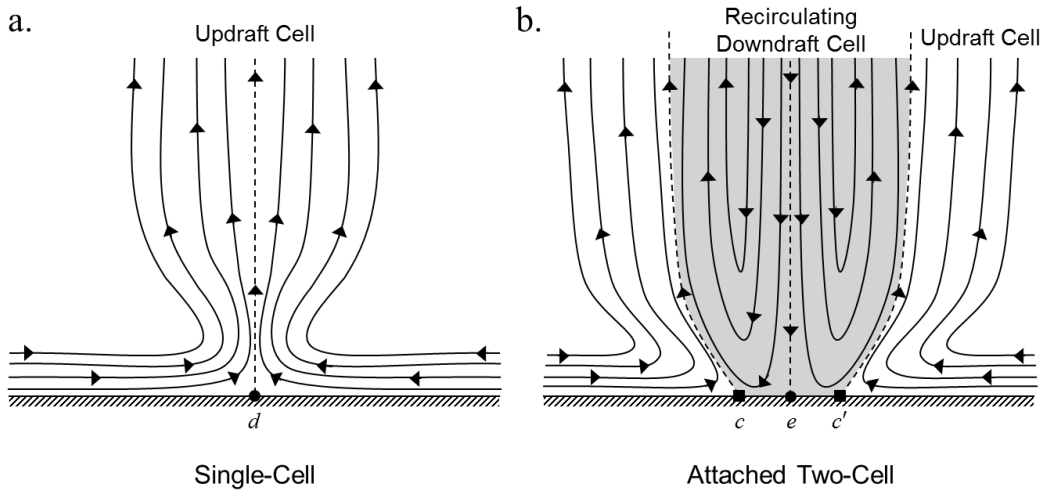

FIGURE 4.1. Schematic representation of the projected streamlines in the (*r*-*z*) plane (showing the radial (*u*) and axial (*w*) velocity components) of (*a*) a single-cell and (*b*) an attached two-cell columnar vortex. The downdraft cell of the two-cell structure is highlighted in grey. Points *d* and *e* represent surface stagnation points for each structure, while *c*-*c′* denotes two points along the bifurcation line centered about the axis of rotation and formed at the interface between the radially entrained and recirculating downdraft flows.

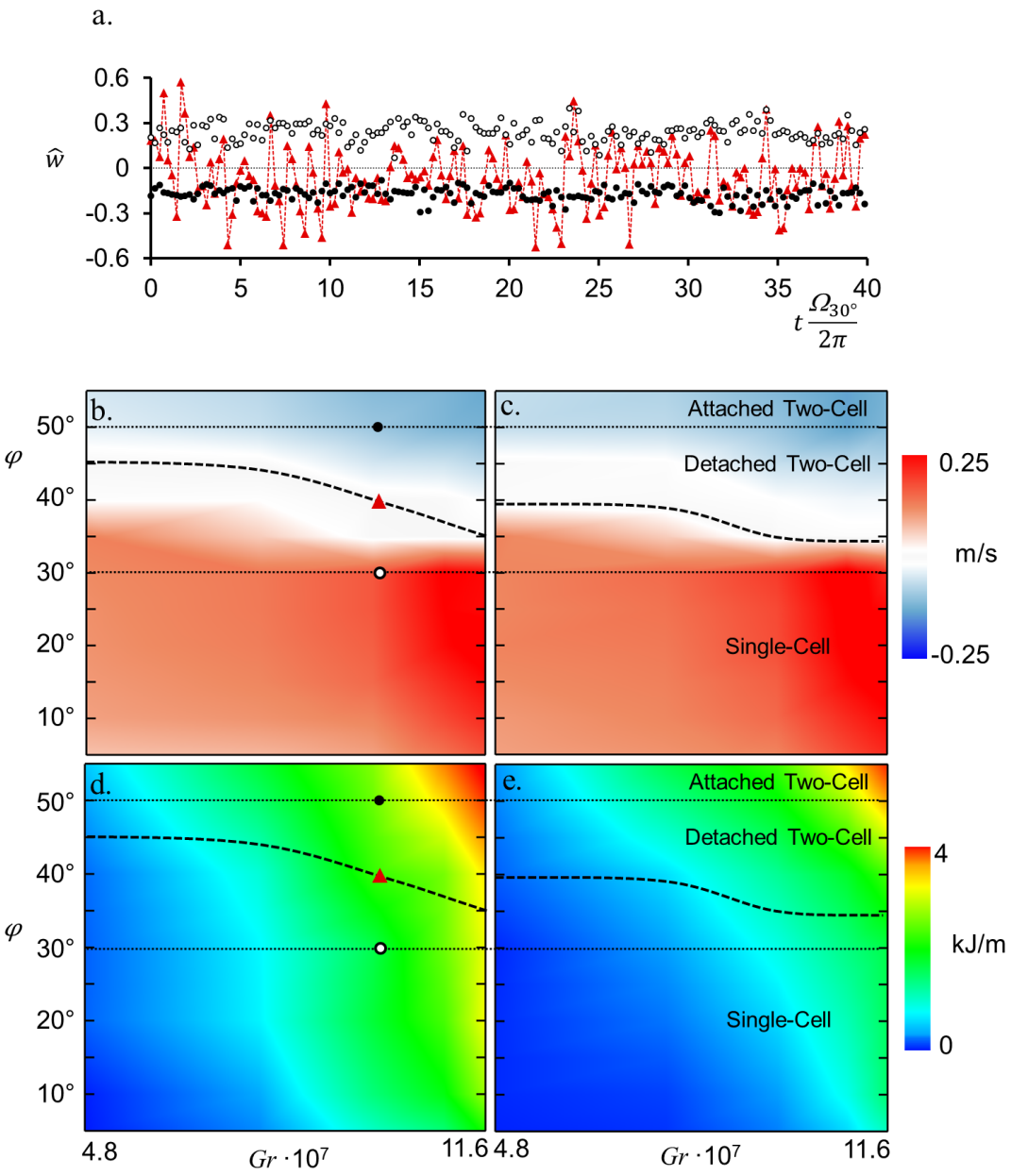

FIGURE 4.2. (*a*) Time traces of the axial velocity along the axis of rotation ($r = 0$) in the presence of single-cell (○) and attached two-cell (●) flows, and near the flow interface between the up- and downdraft cells of a detached two-cell vortex (▲). Color raster plots of the variation with φ and Gr of the time-averaged axial velocity $\overline{w}$ (*b*, *c*) at $r = 0$ and enthalpy $\mathcal{H}$ (*d*, *e*) for $z/h = 0.17$ (*a*, *b,* and *d*) and 0.34 (*c* and *e*). The location of $\overline{w} = 0$ (--) and the experimental regimes defined as single-cell [$\varphi < 30°$], detached two-cell [$30° < \varphi < 50°$], and attached two-cell [$\varphi > 50°$] (···) are denoted with dashed lines. Overlaid symbols (*b* and *d*) correspond to the respective time traces of centerline axial velocity in (*a*).

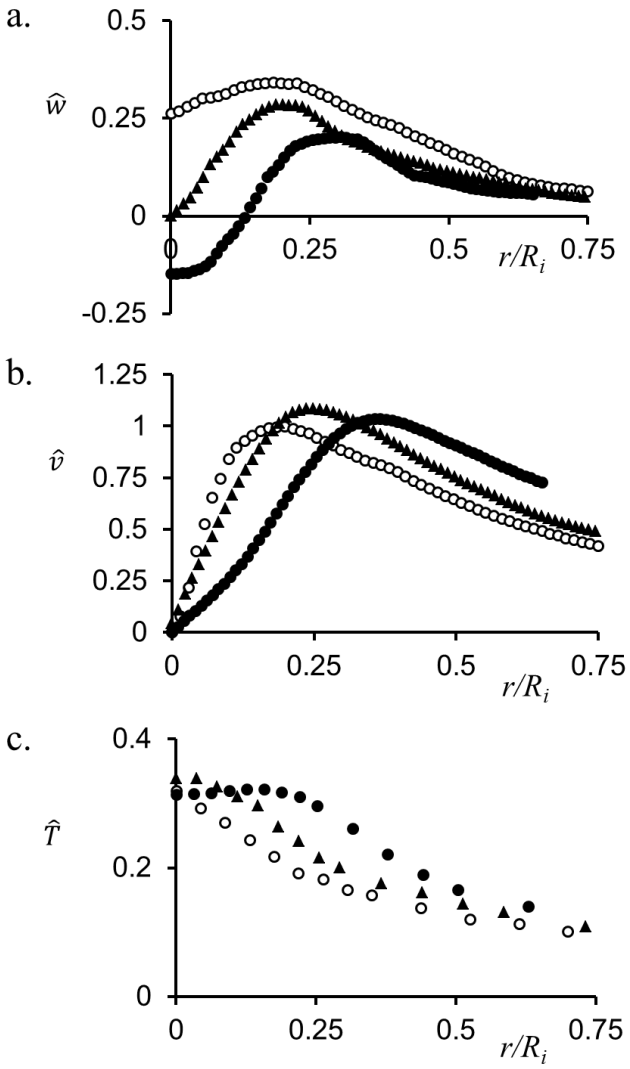

FIGURE 4.3. Radial distributions of the time- and azimuthally-averaged, normalized (*a*) axial and (*b*) tangential velocity and (*c*) temperature of single-cell [$\varphi = 30°$] (○), detached two-cell [$\varphi = 40°$] (▲), and attached two-cell [$\varphi = 50°$] (●) vortices at $z/h = 0.17$ for $Gr = 9.7 \cdot 10^7$.

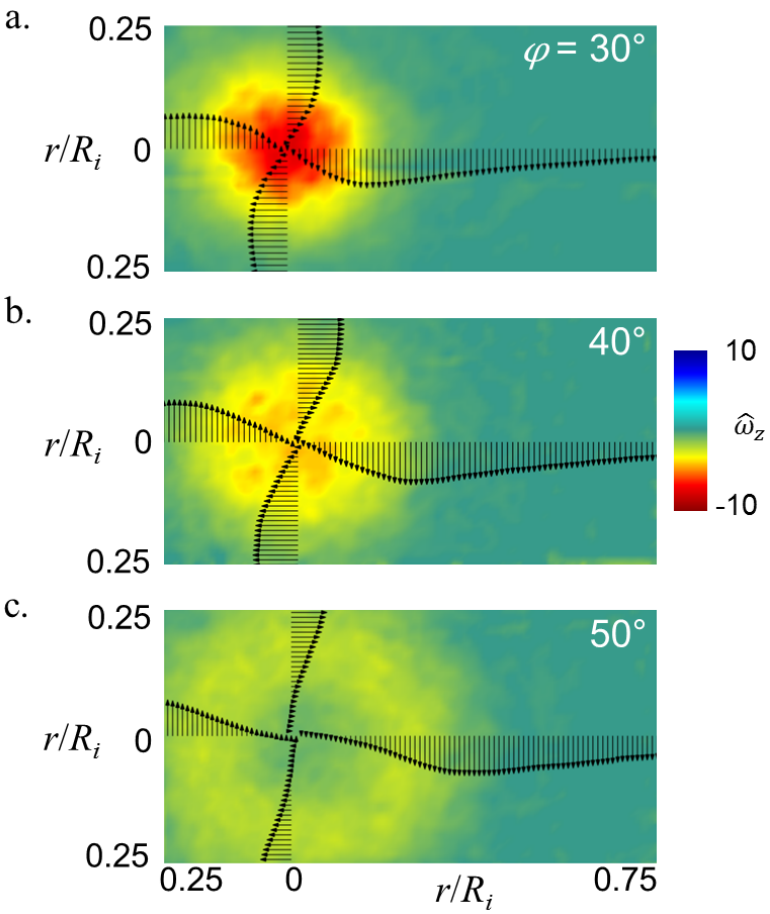

FIGURE 4.4. Time-averaged color raster plot of axial vorticity superposed with radial distributions of tangential velocity vectors of (*a*) single-cell [$\varphi = 30°$], (*b*) detached two-cell [$\varphi = 40°$], and (*c*) attached two-cell [$\varphi = 50°$] vortices at $z/h = 0.17$ for $Gr = 9.7 \cdot 10^7$.

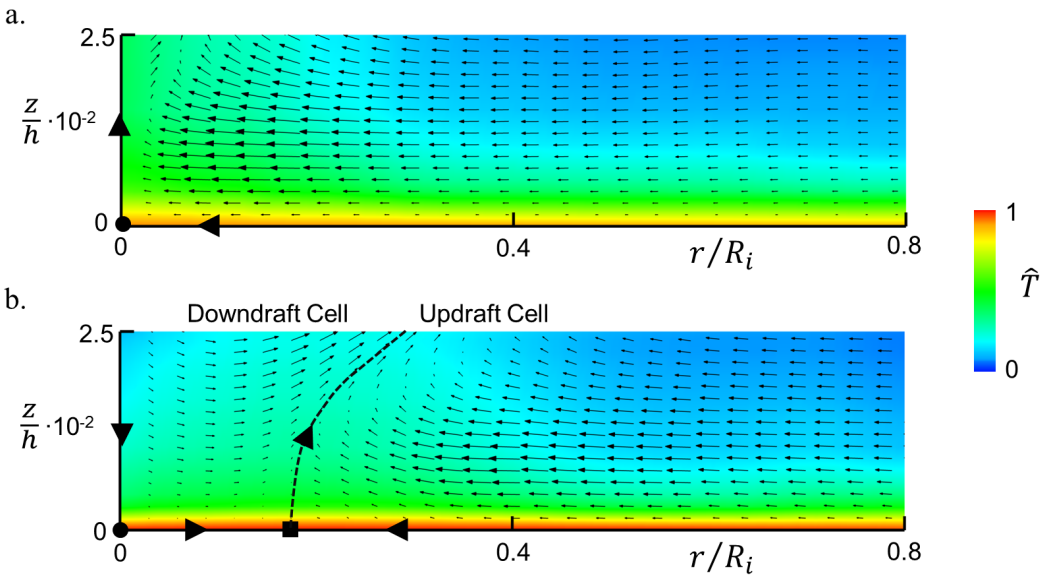

FIGURE 4.5. Color raster plot of normalized temperature superposed with velocity vectors in the *r*-*z* plane [$0 < z/h < 0.025$, $0 < r/R_i < 0.8$] for (*a*) single-cell vortex ($\varphi = 30°$) and (*b*) attached two-cell vortex ($\varphi = 50°$) [$Gr = 9.7 \cdot 10^7$, $T_p = 100°C$]. The central and off-axis stagnation points are marked by (●) and (■), and the flow interface between the up- and recirculating downdraft cells is marked by a dashed line.

CHAPTER V

SINGLE-CELL BUOYANCY-INDUCED, COLUMNAR VORTICES

The flow field of a single-cell buoyancy-induced, columnar vortex, characterized by continuous positive axial flow throughout the height of the cylindrical volume bounded by the vertical flow vanes (cf. Chapter 4), is separated into two primary domains, namely, the vortex column consisting of the core and surrounding outer flow, and the momentum and thermal boundary layers near the heated surface (cf. Figure 2.1). These data are acquired using the 1 m scale facility (cf. Chapter 3) and initially attention is restricted to a vortex engendered for the formation parameters $\varphi = 30°$ and $Gr = 9.7 \cdot 10^7$ ($T_p = 100°C$). In the following section, the flow field of the single-cell vortex column is characterized, while the flow structure within the surface boundary layer is described in §5.2. The effects of the primary control parameters (e.g., Gr and φ) on the flow field while a single-cell core structure is maintained (cf. Figure 4.2b and c) are discussed in §5.3.

5.1 The Vortex Column

The evolution of the vortex core is first explored for the nominal vortex ($\varphi = 30°$ and $Gr = 9.7 \cdot 10^7$) well above the surface layer at an elevation of $z = 10$ cm ($z/h = 0.17$, $\zeta = 0.12$ where $\zeta = \alpha z/R$ [cf. Chapter 2]) in the r-θ plane. Time- and azimuthally-averaged radial distributions of the normalized tangential ($\hat{v}$), radial ($\hat{u}$), and axial ($\hat{w}$) velocity components (normalized by ΩR for a core angular velocity $\Omega = 15$ s^{-1} and core radius $R = 4.5$) and air temperature $\hat{T} = (T\text{-}T_\infty)/(T_p\text{-}T_\infty)$ are shown in

Figures 5.1a and b. Note that each distribution extends radially past the inner vertical edge of the vanes ($\eta = 5.44$ where $\eta = r/R$ [cf. Chapter 2]), into the space between adjacent vanes to $\eta = 5.66$ (cf. Figure 3.1).

The base flow is dominated by the (clockwise, as viewed from above) tangential velocity which at $\eta = 1$ is 3.2 and 27 times as large as $\hat{w}$ and $\hat{u}$, respectively. Within the inner vortex core ($\eta < 0.5$), the tangential velocity varies nearly linearly, with η resembling solid-body rotation, and then begins to level off before reaching its maximum (at $\eta = 1$), followed by a monotonic decay similar to a potential vortex ($\hat{v} \propto \eta^{-1}$). The presence of a wall jet of entrained flow emanating from each azimuthal flow vane is evident within the domain $4.5 < \eta < 5.7$ leading to a local maximum of the tangential velocity at $\eta = 4.9$. When $\eta < 4.5$, the structure of the anchored vortex is similar to that of a free, unbounded columnar vortex. The wall jet imparts angular momentum into the outer flow and disrupts the monotonic decrease of $\hat{v}$ near the inner edge of the vane array. Therefore, the tangential velocity within the outer flow of the columnar vortex is simultaneously affected by the angular momentum of its inner core ($\eta < 1$) and of the entrained flow through the vanes ($\eta > 4.5$). The axial velocity component $\hat{w}$ is positive throughout the measurement domain, and has a local maximum at $\eta = 0.85$, slightly within the vortex core, and a local minimum at $\eta = 0$. The axial velocity decays within the outer flow near the inner edge of the vanes, so that the tangential entrainment jet is nominally two-dimensional $(\hat{u}, \hat{v}, 0)$. The radial velocity component $\hat{u}$ is an order of magnitude smaller than $\hat{v}$ and $\hat{w}$ and changes sign at $\eta = 1.8$, such that $\hat{u} > 0$ for $\eta < 1.8$ indicates the radial spreading of the vortex core, and $\hat{u} < 0$ for $\eta > 1.8$ denotes inward radial entrainment of fluid. Based on the distribution of the tangential velocity

component and the time-averaged location at which $\hat{u} = 0$, it is argued that the annular domain $1 < \eta < 1.8$ is a transition region through the helical shear layer between the inner vortex core, which undergoes solid-body rotation, and the outer flow, which is characteristic of a free vortex. Therefore, $\eta = 1.8$, where $\hat{u} = 0$, marks the time- and azimuthally-averaged radial division between the spreading vortex column and the outer flow.

Figure 5.1b shows the radial temperature distribution within the vortex column measured using the radial array of thermocouple sensors (cf. Figure 3.4a). For the surface temperature of T_p = 100°C ($\hat{T} = 1$), the maximum air temperature, located at the vortex centerline ($\eta = 0$, $\zeta = 0.12$), is 47.6°C ($\hat{T} = 0.32$) and the largest radial thermal gradients lie within the vortex core and annular transition domain ($0 < \eta < 1.8$). Within the outer flow, the temperature continues to decrease and approaches a minimum of $\hat{T} = 0.09$ at $\eta = 5.31$. The elevated temperature at this radial location, compared to the laboratory ambient, indicates that within the vane enclosure significant mixing occurs between surface-heated air that rises into the vortex core and spreads radially, warm (but cooler) air advected from the outer edge of the surface thermal boundary layer, and ambient air (at approximately $\hat{T} = 0$) entrained through the flow vanes above the boundary layer.

The radial pressure gradient induced by the rotation of the vortex core and outer flow is computed from the measured three-dimensional flow field using the radial Navier-Stokes equation in cylindrical coordinates following the procedure of Honohan (2003) and Liu and Katz (2006). In these calculations, the spatial resolution is limited by the SPIV measurements ($\Delta x = \Delta y =$ 3.2 mm) yielding $\Delta\eta = 0.07$ at $\zeta = 0.12$. It is

assumed that the axial gradient of the radial velocity $\partial u/\partial z$ is negligible, and fluid properties are axisymmetric and depend only on the local temperature, measured using a radial array of thermocouple sensors and interpolated onto the SPIV grid. These data show that the radial pressure gradient, $\partial p/\partial \eta$, increases monotonically with η from 0 at the centerline to a local maximum at $\eta = 0.65$, and decreases asymptotically to zero near the edge of the measurement domain. The measured tangential velocity distribution, along with equation (2.2), is used to integrate the radial gradient to obtain a radial distribution of the pressure, $C_p(\eta) = \Delta p/[\frac{1}{2}\rho_f(\Omega R)^2]$ (Figure 5.2), where density, ρ_f, is defined using the film temperature (T_f, cf. Chapter 3), and Ω and R are the angular velocity and radius of the vortex core at $\zeta = 0.12$ respectively. The minimum pressure occurs at the vortex centerline, and monotonically increases with increasing η, asymptotically approaching $C_p = -0.25$ at $\eta = 4$. C_p does not vanish within the vane enclosure [$p(\eta = 5.44) < p_\infty$] due to the pressure imposed by the array of flow vanes as a result of the induced tangential velocity component of the entrained flow. Therefore, in addition to the global length scale, the vanes also impose a pressure boundary condition at $r = R_i$ that intensifies the low pressure along the centerline of the anchored vortex. We note in passing that for atmospheric vortices with sufficiently large Rossby numbers ($Ro = U/Lf = \Omega/f$, where Ω is the angular velocity of the vortex core and f is the Coriolis frequency defined as twice the rotation rate of the earth times the sine of the latitude angle) the state of the flow is referred to as a cyclostrophic balance (Holton 2004) between the local radial pressure induced by the rotating fluid column and the centrifugal force [cf. equation (2.2)]. While for a natural dust devil the Rossby number is typically

O[100-10,000] (Logan 1971), it is as high as 200,000 for the laboratory-scale nominal vortex.

Axial accelerations within the flow field are affected by the local radial temperature gradient that provides a radial buoyancy force. The radial distribution of the radial gradient of normalized temperature, $-\partial\hat{T}/\partial\eta$, shows that the temperature gradient has a local maximum near $\eta = 1$, drops sharply within $1 < \eta < 1.33$ to 0.5 $(-\partial\hat{T}/\partial\eta)_{max}$ and thereafter decreases (Figure 5.3). However, within the vortex core, where $-\partial\hat{T}/\partial\eta$ is nearly invariant ($\hat{T}$ decreases nearly linearly from $0 < \eta < 1$, cf. Figure 5.1b), $\hat{w}$ *decreases* towards the centerline (cf. Figure 5.1a). As shown in equation (2.4), the radial distribution of axial momentum depends on *both* the local $\hat{T}(\eta)$ (i.e., g') and the axial pressure gradient, $\partial C_p/\partial\zeta$. The pressure within the vortex core is lowest near the surface where the tangential velocity has a maximum and increases in the vertical direction, leading to a downward force that reduces the effect of buoyancy and leads to the reduction in axial velocity along the axis of symmetry (cf. Figure 6.3). The radial variation of the axial pressure gradient (Figure 5.3) is nonnegligible only for $\eta < 1.5$. These data indicate that the vertical pressure gradient along the centerline deflects the axial flow radially and thereby affects a local maximum of the axial velocity near $\eta \approx 1$, in contrast to nonrotating, thermal plumes which typically have an axial velocity maximum along the vertical axis of symmetry. Therefore, while the axial momentum of the columnar vortex is affected by the radial distributions of both the radial temperature and axial pressure gradients, each is dominate in a different radial domain.

The axial velocity distribution, coupled with the angular momentum of the rotating vortex column, determine the magnitude and radial distribution of kinetic energy

flux within the vortex core and the outer flow. The radial distribution of the integral of the kinetic energy flux $\dot{E} = 2\pi \int_0^r \frac{\rho}{2}\left(v^2 + w^2\right)(\vec{V} \cdot \hat{n})rdr$ through a radially-expanding, circular control surface at a fixed height ($\zeta = 0.12$) is computed and $\hat{\dot{E}} = \dot{E}/(\rho\nu g R^2)$ is shown in Figure 5.4. Within the inner domain of the vortex core, $\eta < 0.5$, the kinetic energy is negligible ($\hat{\dot{E}} < 0.04\hat{\dot{E}}_{\max}$). Near $\eta = 1$, the integral of flux increases rapidly, and for $\eta > 2$, begins to level off, reaching a nominally invariant value near $\eta = 4$. At this distance from the vortex centerline, the magnitude of the axial velocity decreases (cf. Figure 5.1a), resulting in a reduction in the flux of energy through the control surface near the outer edge of the vane enclosure. The distribution of kinetic energy therefore implies that the majority of the energy within the vane enclosure is available within the outer flow domain of the vortex column ($1 < \eta < 4$), i.e., outside the core itself ($\eta < 1$). Although the flow field maintains a considerable fluid torque outside of the annular domain ($\eta > 4$) due to the significant tangential velocity (cf. Figure 5.1a) associated with the entrained flow, the small axial velocity at $\eta > 4$ reduces the contributions of this angular momentum to $\dot{E}$.

Axial Similarity

The vertical evolution of the vortex core and surrounding outer flow is investigated by considering the axial similarity of the nominal vortex. As noted in Chapter 2, in the absence of external flow boundaries, buoyancy-induced columnar vortices can be thought of as a combination of two self-similar flows (i.e., nonrotating, thermal plumes and momentum-driven, swirling jets) and therefore, it stands to reason that a *free* buoyant, columnar vortex may also be considered self-similar, and its streamwise evolution readily compared to similar analogous flows.

The flow field of the nominal anchored, columnar vortex is investigated using radial distributions of the time- and azimuthally-averaged tangential and axial velocity components and temperature at ten equally-spaced horizontal planes, 2.5 cm apart ($\Delta z/h = 0.042$), above the heated surface starting at $z = 2.5$ cm ($z/h = 0.042$). Additional SPIV measurements are acquired in a vertical plane (r-z) at $\theta = 0°$ (corresponding to the azimuthal location between the enclosure centerline and a vane pivot; cf. Figure 5.11a) above the heated surface ($0.0015 \leq z/h \leq 0.082$, with resolution of $\Delta z/h = 0.0015$), augmented by temperature measurements using a vertical array of thermocouple sensors (placed $\Delta z/h = 0.005$ apart, cf. Figure 3.4b). These data are recorded for a single θ–plane, and the time-averaged flow is assumed to be axisymmetric, which neglects the 12-fold symmetry of the enclosure. Following the analysis in Chapter 2, the measured velocity field is used to extract the axial variation of each characteristic scale of the nominal vortex flow [cf. equation (2.8)], namely the core radius $R(z)$ (defined by the radial location of the peak tangential velocity), centerline weight deficiency $g'(0, z)$ [$g' = \frac{T-T_\infty}{T_\infty} g$], and tangential and axial velocity components at $r = R$, namely, $v(R, z)$ and $w(R, z)$ respectively. The axial variations are plotted in Figures 5.5a through d with respect to z/h, a dimensionless geometric height normalized by the height of the array of azimuthal flow vanes ($h = 0.6$ m).

Figure 5.5a shows that for $z/h > 0.038$, the vortex core radius (defined by R) increases linearly with elevation, $\partial R/\partial z = 0.056$, as the vortex core spreads radially due to entrainment along the edge of the vortex core. The characteristic height, $\delta_d = z/h = 0.038$, denotes the top of the development region that includes the surface boundary layer (cf. Figure 2.1) and the lowest extent of the nominal vortex column above

which the flow can be described as self-similar. As discussed in Chapter 2, the scaling of the continuity equation yields $R/z \propto u_e/\overline{w}|_{r=R}$ for $z > \delta_d$. Therefore, along the ray $R = \alpha z$, $u/w = \alpha$ and the entrainment coefficient, α, defined by the slope of the dashed line in Figure 5.5a, is found to be 0.056 for the nominal base flow vortex. As demonstrated by Turner (1962), for thermal plumes, α = O[0.1], indicating that the nominal buoyancy-induced columnar vortex entrains less ambient fluid along the axial extent of its periphery than a corresponding nonrotating, thermal plume. As a result of this diminished entrainment of cool ambient air into the core (above the ground-plane boundary layer), the centerline weight deficiency (i.e. centerline air temperature) decreases at a *lower* rate, $g' \propto z^{-1/4}$ (Figure 5.5b) compared to the axial dependence of a nonrotating, thermal plume above a horizontal heated surface ($g' \propto z^{-1/3}$, Turner 1969). As shown in Figure 5.5c, the peak tangential velocity decreases linearly with elevation at a rate $\partial[v(R)]/\partial(z/h)$ = -0.2, similar to nonbuoyant, swirling jets (e.g., Chigier and Chervinsky 1967). However, in contrast to the decay of the axial velocity same nonbuoyant, swirling flows ($w \propto z^{-1}$, Rajaratnam 1976) the axial velocity in the buoyant, columnar vortex continues to accelerate well above the development region, δ_d, owing to the nonzero weight deficiency within its core. The vertical evolution of axial velocity at $r = R$ ($\eta = 1$) increases like $z^{1/4}$, slower than a corresponding thermal plume ($w \propto z^{1/3}$, Turner 1969), ostensibly owing to the downward pressure force, that does not occur in nonrotating plumes, and which counters the upward force of buoyancy within the vortex core (cf. Figure 5.3).

The similarity of the nominal vortex is further investigated by examining radial distributions within the vertical domain $0.042 < z/h < 0.42$ (2.5 cm < z < 25 cm).

Figures 5.6a, b, and c show radial distributions of time- and azimuthally-averaged tangential and axial velocity components and weight deficiency in similarity coordinates [$\eta = r/R(\zeta)$, $\zeta = \alpha z/R(\zeta)$] at five equally-spaced axial elevations $\Delta z = 5$ cm apart starting at $z = 5$ cm ($\zeta \approx 0.07$). At each ζ, each velocity component is scaled by its value at $\eta = 1$, and the weight deficiency is scaled by its value at $\eta = 0$. At $\zeta = 0.07$, 0.17, 0.22, and 0.26 the radial extent of the measurement domain is $0 < \eta < 4.5$, while at $\zeta = 0.12$ the radial domain extends past the inner edge of the vanes to $\eta = 5.66$. The collapse of these data indicates that, for the nominal, anchored vortex, the axial evolution of the core and surrounding outer flow is reasonably self-similar within $0 < \eta < 4.5$, despite the length scale imposed by the array of vanes.

The radial distributions of tangential velocity in similarity coordinates (Figure 5.6a) imply that the linear variation of peak tangential velocity with ζ at $\eta = 1$ (cf. Figure 5.5c) holds for all η within the domain $0 < \eta < 4.5$. An approximate functional dependence for the radial distribution of tangential velocity, $h(\eta)$ [cf. equation (2.8)], is inspired by the tangential velocity of the Lamb-Oseen two-dimensional model of a viscous vortex, $v = \Gamma_z(1\text{-}e^{-(r/R)^2})/(2\pi r)$. Using the axial circulation of the vortex column, computed from the measured radial distribution of tangential velocity, $\Gamma_z = 2\pi \int -\partial(rv)/\partial r \, dr$, the tangential velocity distribution in similarity coordinates is given by $v(\eta,\zeta) = v(1,\zeta)h(\eta) = \Gamma_z(\zeta)\left(1 - e^{-\eta^2}\right)/2\pi\eta R(\zeta)$, plotted in Figure 5.6d along with the data measured at $\zeta = 0.12$. These data show reasonable agreement for $0 \leq \eta \leq 1.75$. Since the anchored, columnar vortex is radially confined by the vanes, the tangential velocity distribution does not vanish at large η as is predicted by

the Lamb-Oseen model. It is therefore conjectured that the slight mismatch between $h(\eta)$ and the measured distributions within the annular domain $1.75 < \eta < 4.5$, results from the azimuthal momentum contributed to the outer flow by the entrainment wall jet.

Unlike the tangential velocity, the radial distributions of the axial velocity (Figure 5.6b) exhibit some dispersion with increasing elevation for $\eta > 2$, ostensibly as a result of the variation of the entrainment through the vanes with elevation. The measured radial distributions are used to obtain a functional fit, $f(\eta)$ [cf. equation (2.8)], to describe $w(\eta, \zeta)$ based on a Gaussian function, which is frequently used to approximate the time-averaged distribution of axial velocity in nonrotating thermal plumes and jets. Since the radial distribution of the axial velocity in the columnar vortex has a maximum away from the centerline (cf. Figure 5.1), $f(\eta)$ is a shifted Gaussian centered at $\eta = 0.85$ and scaled by the radial location at which the magnitude of the normalized axial velocity, $\widehat{w}$, is e^{-1} of the peak value (i.e., at $\eta = 3$). Using this description, the axial velocity in similarity coordinates is approximated by $w(\eta,\zeta) = w(1,\zeta)f(\eta) = w(1,\zeta)e^{-(\eta-1)^2/4}$, shown in Figure 5.6e with the measured axial velocity at $\zeta = 0.12$. Good agreement is obtained over the entire measurement domain ($0 < \eta < 5.66$).

The weight deficiency of the columnar vortex is plotted in similarity coordinates in Figure 5.6c and shows good collapse for each measurement plane. Similar to the distributions of tangential velocity, the presence of the vanes prevents g' from vanishing for large η, because $T(\eta = 5.44) > T_\infty$ at all elevations within the vane enclosure volume. Due to the form of the radial distribution of weight deficiency, it is necessary to divide the fit, $m(\eta)$ [cf. Equation (2.8)], into two domains: the vortex core ($\eta < 1$) and outer flow ($1 < \eta$). Outside the vortex core, $\eta > 1$, the weight deficiency assumes a Gaussian

distribution centered about $\eta = 0$, $g'(\eta,\zeta) = g'(0,\zeta)m(\eta) = g'(0,\zeta)[\gamma\{1 - g'(5.44,\zeta)/g'(0,\zeta)\}e^{-\eta^2/4} + g'(5.44,\zeta)/g'(0,\zeta)]$, scaled by a fraction, γ, of its centerline value and offset such that $g' \to g'(5.44,\zeta)$ at the radial edge of the vane enclosure. The measured temperatures within the vortex core show a linear increase of weight deficiency, described by $g'(\eta,\zeta) = g'(0,\zeta)m(\eta) = g'(0,\zeta)\left[1 + \eta\left(g'(1,\zeta)/g'(0,\zeta) - 1\right)\right]$ for $\eta < 1$. The fit (Figure 5.6f) is in good agreement with the measured data for $\zeta = 0.12$. Typically, for nonrotating thermal plumes, it is assumed that the radial distribution of weight deficiency has a Gaussian shape (Turner 1969). Clearly, the weight deficiency of the nominal vortex deviates from this distribution when $\eta < 1$, displaying elevated temperatures within this domain compared to the inwardly extended Gaussian distribution used to describe the outer flow, with $g'(0,\zeta)_{\text{Gaussian}}/g'(0,\zeta)_{\text{actual}} = \gamma = 0.6$. Therefore, the nominal vortex displays a warmer core (cf. Figure 5.5b) than would be expected for a nonrotating plume formed under the same thermal conditions, again owing to the reduction in entrainment along the edge of the vortex core above the ground-plane boundary layer (cf. Figure 5.5a).

The radial distribution of the axial velocity at $\zeta = 0.12$ in Figure 5.6e is used to compute the corresponding distributions of the normalized axial mass ($\hat{\dot{m}} = \dot{m}/\dot{m}_{ref}$) and momentum ($\hat{\dot{P}} = \dot{P}/\dot{P}_{ref}$) fluxes through a circular control surface (r-θ) with increasing radii where $\dot{m} = \int_0^r \rho w r dA = 2\pi\rho w(1,\zeta)R^2 \int_0^\eta f(\eta')\eta' d\eta'$, and $\dot{P} = \int_0^r \rho w^2 r dA = 2\pi\rho w(1,\zeta)^2 R^2 \int_0^\eta f(\eta')^2\eta' d\eta'$ (Figures 5.7a and b). The integrals of the mass and axial momentum fluxes are each normalized by a reference flux ($\hat{\dot{m}} = \dot{m}/\dot{m}_{ref}, \hat{\dot{P}} = \dot{P}/\dot{P}_{ref}$) based on a radially-uniform distribution of the

characteristic axial velocity $w = w(\eta = 1, \zeta = 0.12)$ through the cross-section of the vortex core ($0 < \eta < 1$). While $\hat{\dot{m}}$ increases monotonically throughout the radial domain, $\hat{\dot{P}}$ increases linearly within the domain $1 < \eta < 3$ and saturates to $\hat{\dot{P}} = 2.6$ at $\eta \approx 3.5$, indicating an upper bound on the integral of the axial flux of linear axial momentum, resulting in the invariance of the integral of the kinetic energy flux for $\eta > 4$ (cf. Figure 5.4). From the expressions obtained in Figure 5.5, the axial variation of the integrals of the mass and axial momentum fluxes can be written as $2\pi\rho_0 w(R,z)R(z)^2 z^{9/4}$ and $2\pi\rho_0 w(R,z)^2 R(z)^2 z^{5/2}$, respectively, in a form similar to the expressions derived by Batchelor (1954) and Turner (1973) for turbulent, nonrotating thermal plumes in an unstably stratified environment (for which $\dot{m} \propto z^{7/3}$ and $\dot{P} \propto z^{8/3}$). The present measurements show that the axial rate of increase of the integrals of the mass and axial momentum fluxes within the nominal vortex is *smaller* than the corresponding quantity in the thermal plume, consistent with the fact that the entrainment coefficient, α, of the base flow vortex is smaller than that of a nominal nonrotating, thermal plume (cf. Figure 5.5a). This result is evident in equation (2.6), which shows that the axial gradient of the axial momentum is diminished in the presence of a nonzero tangential velocity owing to the adverse axial pressure gradient imposed due to the rotation of the core flow, which counteracts the buoyancy and ultimately leads to a reduction in the axial velocity along the axis of rotation.

The normalized axial variation of the integral of the kinetic energy flux, $\hat{\dot{E}} = \dot{E}/(\rho\nu g(4R)^2)$, through a horizontal cross-sectional surface of radius $\eta = 4$ (i.e., the location at which kinetic energy flux saturates with η, cf. Figure 5.4) is computed at ten equally-spaced axial elevations ($0.042 < z/h < 0.42$) and augmented with SPIV

measurements in an *r-z* plane ($0 < z/h < 0.08$) above the surface. These data show two distinct axial domains (Figure 5.8). Close to the surface, within $0 \le z/h \le 0.04$, $\hat{\hat{E}}$ increases rapidly from 0 to approximately 300. This sharp rise occurs as flow near the surface is turned vertically near the central stagnation point (cf. Figure 4.1a), resulting in significantly larger axial velocities than can be induced by buoyancy alone. In the second domain ($0.04 \le z/h \le 0.42$), the axial rate of change of the integral of the kinetic energy flux diminishes considerably, and the axial acceleration is dominated by buoyancy. Within this domain, the available extractable power increases nearly two-fold [$\hat{\hat{E}}(z/h = 0.05) = 1.9\hat{\hat{E}}$ $(z/h = 0.42)$], varying as $(z/h)^2$. The increase in integral of the kinetic energy flux with elevation continues as long as the axial velocity accelerates due to buoyancy [cf. equation (2.6)]. While the rotation-induced, axially-adverse pressure gradient within the core of the vortex somewhat mutes the effect of the buoyancy force and, therefore, the axial rate of increase in axial momentum flux, this pressure gradient is far weaker within the outer flow. The axial and azimuthal flows within this outer annular domain include the majority of the kinetic energy (cf. Figure 5.4) and are driven by the motions of the inner core flow and the entrainment through the vanes. This axial and azimuthal flow generates significantly more power than could be produced by natural convection alone.

As shown in equation (2.10), the axial momentum equation in similarity variables depends on two (dimensionless) parameters at each elevation $\zeta = Z$, namely, the swirl number and Froude number [$S(Z) = v(1, Z)/w(1,Z)$, and $Fr(Z) = (\alpha \cdot w^2(1,Z)/2g' \cdot R(Z))^{1/2}$]. The axial variation of $S(\zeta)$ and $Fr(\zeta)$ within the domain $0.036 < \zeta < 0.26$ (in which the vortex is self-similar, cf. Figure 5.5) is shown in Figure 5.9. These data show that

$S(\zeta)$, which measures the vertical pitch of the helical motion at the edge of the vortex core, decreases with elevation owing to the buoyancy-induced acceleration of axial velocity, $w \propto z^{1/4}$ (cf. Figure 5.5d), which is accompanied by a decrease in the tangential velocity (cf. Figure 5.5c). The rate of decrease of $S(\zeta)$ diminishes with elevation, and S decays to less than 2 within the measurement domain. Concomitantly, Fr, which measures the ratio of axial kinetic to buoyant potential energy, increases from 0.18 to 0.3 between $\zeta = 0.036$ and 0.26 as thermal energy is continually converted into mechanical (kinetic) energy. As noted in connection with the axial momentum equation (2.10), the dimensionless buoyant forcing term $\int_0^\infty m(\eta)\eta d\eta$ is scaled by Fr^{-2}, and so long as $Fr < 1$, the effect of the buoyancy is amplified. The Froude number increases with elevation, due to the decrease in weight deficiency in the vortex core, entrainment of cooler air along its vertical edge, and a net increase in the axial velocity, in turn due to buoyancy-induced axial accelerations (as long as $g' > 0$). Therefore, the effect of buoyancy in equation (2.10) diminishes with elevation as the vortex core continues to cool. Eventually $g'(0, \zeta) \rightarrow 0$, $Fr \rightarrow \infty$, and the flow is well-approximated by a nonbuoyant, swirling jet.

The radial distributions of local $S(\eta)$ and $Fr(\eta)$ are shown in Figure 5.10a and b, respectively, for $\zeta = 0.12$, and are divided into three annular regimes based on the magnitude of the swirl number. While $S(\eta)$ is computed directly from the velocity (SPIV) data (for which $\Delta\eta \approx 0.07$), the radial variation of $Fr(\eta)$ is calculated at the location of each radial temperature measurement ($\Delta\eta \approx 0.22$ for $\eta < 1.76$ and $\Delta\eta = 0.44$ for $\eta > 1.76$). Region I ($\eta < 0.5$) is the inner vortex core in which v increases faster than w and S increases nearly linearly. Within this domain, the weight deficiency and Fr have a local maximum and minimum, respectively, along the centerline. Within Region II

($0.5 < \eta < 3$) S is nearly invariant through the edge of the core (at $\eta = 1$), in the transition domain ($1 < \eta < 1.8$) [cf. Figure 5.1a], and well into the outer flow. The vertical pitch of the helically swirling flow is nearly invariant over a wide range of η. On the other hand, Fr has a local maximum at $\eta = 1$ (where $Fr = 0.21$) and thereafter decreases nearly linearly to 0.09 at $\eta = 3$. Region III ($\eta > 3$) is characterized by the effects of the entrained flow, which leads to a radial increase in the tangential velocity, while $w(\eta)$ decreases monotonically (cf. Figure 5.1a). As a result, S increases sharply and has a peak of 20.5 at $\eta = 4.9$. Fr continues to decrease with the axial velocity even as the weight deficiency remains nearly invariant with η.

5.2 Near-Surface Vortex Structure

The mechanisms that drive the formation and sustainment of the vortex core and its outer flow take place within a relatively thin [$z/h \approx$ O(0.017)] swirling boundary layer over the heated surface. It is the interaction of this boundary layer with the induced buoyant instability and near-surface pressure forces that is responsible for the conversion of the thermal energy from the heated surface to the kinetic energy associated with the vortical flow. The conversion mechanism that generates and sustains the buoyancy-induced columnar vortex is associated with the production, and eventual tilting, of the induced horizontal vorticity concentrations within the ground-plane boundary layer.

The Flow Field Near the Ground-Plane

The thermal energy and vorticity concentrations that affect the structure and dynamics of the columnar vortex originate from the boundary layer of entrained air over the heated surface. For $\varphi = 30°$ and $Gr = 9.7 \cdot 10^7$, the time-averaged flow field in an azimuthal plane passing through the centerline of the columnar vortex ($\eta = 0$) and the

pivot location of an azimuthal vane and extending to the ground-plane (Figure 5.11a) is shown in Figure 5.11b using vectors of radial and axial velocity overlaid on a raster plot of the normalized tangential velocity, $\hat{v}$, distribution. A raster plot of the corresponding normalized radial velocity, $\hat{u}$, and normalized temperature distribution, $(T\text{-}T_\infty)/(T_p\text{-}T_\infty)$, are shown in Figures 5.11c and d, respectively. These data are not azimuthally averaged and the flow field is assumed to be axisymmetric despite the twelve-fold symmetry of the vane enclosure. These SPIV measurements are taken in four segments, assembled to form the investigation domain $0 < r < 18$ cm, $0 < z < 5$ cm. The data are normalized and similarity variables are defined using the core radius (4.5 cm) and angular velocity (15 s^{-1}) of the vortex core at $z = 10$ cm ($\zeta = 0.12$) so that the interrogation domain in similarity coordinates is $0 < \eta < 4$, $0 < \zeta < 0.06$ and can readily be compared to the radial distributions of Figure 5.1. Temperature measurements are recorded at $\Delta r = 1$ cm ($\Delta\eta = 0.22$) increments using the vertical thermocouple rake over the identical radial plane ($0 < r < 18$ cm, $0 < z < 5$ cm; $0 < \eta < 4$, $0 < \zeta < 0.06$). The velocity distributions elucidate several distinguishing characteristics of the single-cell vortex flow near the surface. As the flow near the edge of the measurement domain is entrained towards the centerline, the radial velocity at the top edge of the boundary layer ($\delta = 10.1$ mm at $\eta = 4$), increases and develops a local maximum (e.g., $\delta = 8.26$ mm at $\eta = 2$) that monotonically increases and moves closer to the surface as η decreases (see also Figure 5.12). Simultaneously, the axial velocity component begins to increase at higher elevations, and closer to the centerline. As shown in Figure 5.12d, the temperature of the air above the surface increases near the centerline as heated air is advected axially,

intensifying the effect of buoyancy, which in turn contributes to the concurrent increase in the magnitude of the axial velocity.

As the entrained flow approaches the centerline, it is turned upward and accelerated axially, forming a central stagnation point on the surface beneath the vortex column at $\eta = 0$, $\zeta = 0$ (cf. Figure 4.1a). This process is accompanied by a significant thickening of the thermal layer ($\eta < 1$, Figure 5.12d) as the axial velocity leads to vertical advection of surface heated air into the vortex core. The upward turning of the flow is accompanied by a change in direction (and sign) of radial velocity, marked by the contour $u = 0$ (white) in Figure 5.11c. The turning flow contracts at $\zeta = 0.02$ ($z/h = 0.027$) and the narrowest radial extent of its edge, defined by the maximum tangential velocity located at $\eta = 0.67$ and referred to as a "vortex jump" by Mullen and Maxworthy (1977), is discussed further in connection with Figure 5.14. Following this contraction, the flow expands rapidly (as is evident by the increase of the domain in which $u > 0$), and ultimately reaches a nominally-invariant (self-similar) core radius at higher elevations, as discussed in §5.1. Below $\zeta < 0.03$ ($z/h < 0.04$) a clear division between the domains containing $u > 0$ and $u < 0$ is identified. Above this elevation, negligible radial velocity is recorded in an increasingly larger radial band as the location of zero entrainment moves radially outwards towards $\eta = 1.8$ at $\zeta = 0.12$ (cf. Figure 5.1a). As also shown in Figure 5.11b, the tangential velocity intensifies, reaches a maximum velocity at the location of the vortex contraction ($\eta = 0.67$, $\zeta = 0.02$), and then migrates radially outward as the elevation increases, from $\eta = 0.77$ at $\zeta = 0.03$ to $\eta = 0.85$ at $\zeta = 0.06$. For $\zeta > 0.03$, the radial location of v_{max} and the rate of spreading of the vortex core are determined by the entrainment coefficient, α (cf. Figure 5.5a).

The evolution of the flow near the surface is shown in axial distributions of the radial velocity at η = 1, 2, 3, and 4 (Figure 5.12). As the flow is entrained towards the base of the vortex column, the velocity distribution of the radial boundary layer evolves from a typical viscous layer (at η = 4) into a distribution reminiscent of a wall-jet (at η = 1), as a result of the vortex-induced radial pressure gradient. As discussed in §5.1, the upper vortex column is in cyclostrophic balance (i.e., $\rho v^2/r = \partial p/\partial r$). However, within the boundary layer, this force balance is modified by viscous effects at the heated surface, which slow the overlying flow, thus reducing the centripetal force, and resulting in a net radial inward force due to the induced radial pressure gradient that drives the flow near the surface. This wall-jet flow driven by radial entrainment into the vortex core is characterized by layers of vorticity concentrations of opposite sense (i.e., different directions of rotation) above and below the velocity peak that couples the surface boundary layer and the overlying flow (Wilson and Rotunno 1982). Baker (1981) showed experimentally that the combined thickness of the two vorticity layers should remain nominally invariant, while the height of the viscous layer becomes progressively smaller as the flow is entrained toward the vortex centerline. This observation is confirmed by the current measurements and denoted by the dashed line in Figure 5.12. It is noteworthy that while the flow within the boundary layer accelerates with decreasing η, the magnitude of the radial velocity above the boundary layer decreases as the flow approaches the centerline and is turned upward by the vertical motions of the vortex core, eventually changing signs for $\zeta > 0.03$ at $\eta \approx 0.8$ (cf. Figures 5.11b and c).

Assuming axial symmetry (i.e., disregarding the discrete effects of the 12 vanes), the data shown in Figure 5.11a are used to create a 3-D volume that includes the swirling

boundary layer and the bottom edge of the vertical vortex column. Particle pathlines are calculated using this data by numerically releasing particles near the edge of the measurement domain within the boundary layer, and are displayed in an isometric view of the cylindrical domain $0 < \eta < 4$ and $0 < \zeta < 0.06$ (Figure 5.13). In the boundary layer, far from the vortex centerline, the radial and tangential velocities are comparable in magnitude and the entrained air spirals inward. The strength and direction of the swirling flow are determined by a balance between the angle set by the azimuthal flow vanes and the strength of the vortex-induced radial pressure gradient. As the flow approaches the centerline, the radial velocity near the surface increases and concentrates the flow at the base of the column, where it ultimately turns upward at the surface stagnation point (cf. Figure 4.1a) and is accelerated by buoyancy. Once the flow is turned upwards, the particle pathlines that extend into the vortex column initially contract inwards before expanding radially and forming a helical pattern throughout the remainder of the vortex core.

Vorticity Production Mechanism

Buoyancy-induced, columnar vortices contain significant amounts of kinetic energy compared to nonrotating thermal plumes formed under the same conditions, due to the advection, tilting, and stretching of the boundary layer vorticity. The axial turning of the surface flow near the centerline of the vortex is affected by the radial pressure gradient which, in turn, is affected by the angular momentum of the flow. Because the angular momentum is ultimately affected by the axial vorticity, it is instructive to examine the source of the vorticity within the vortex core. Contour plots of the three components of the time-averaged vorticity vector, $\vec{\omega} = (\omega_r, \omega_\theta, \omega_z)$ =

$[-\partial v/\partial z, \partial u/\partial z - \partial w/\partial r, r^{-1}\partial(rv)/\partial r]$, within the domain shown in Figure 5.11a, normalized by the angular velocity of the vortex core at $z/h = 0.17$ ($\Omega = 15\ s^{-1}$) and calculated by assuming that azimuthal variation in the time-averaged data is negligible, are shown as $\hat{\omega}_r$, $\hat{\omega}_\theta$, and $\hat{\omega}_z$ in Figures 5.14a through c, respectively. The radial component of vorticity (Figure 5.14a) is positive throughout the boundary layer (the sense of the radial vorticity depends on the direction of rotation induced by the azimuthal flow vanes). These data show that radial vorticity is primarily concentrated within the surface layer, indicating that the axial variation of tangential velocity is comparatively small elsewhere (cf. Figure 5.5c). The radial vorticity has a local maximum at $\eta \approx 0.50$ and $0 < \zeta < 0.01$, beneath the vortex contraction (located at $\zeta = 0.02$ [$z/h = 0.027$]) where the tangential velocity is largest. The azimuthal vorticity (Figure 5.14b) exhibits the two layers of opposite sense associated with a wall-jet flow structure (cf. Figure 5.12) where the negative vorticity within the lower viscous layer is of the same sign as the tangential velocity. Radial variations in the axial velocity within the contraction region of the forming vortex core contribute to the concentration of positive azimuthal vorticity layer along the periphery of the vortex core. The onset of the core of the columnar vortex can be inferred from axial vorticity concentrations (Figure 5.14c). These data show that the largest concentration of axial vorticity is confined to the domain $\eta < 1$. Within the columnar vortex, the peak axial vorticity occurs at the height of the vortex contraction along the vortex centerline ($\eta = 0$, $\zeta = 0.02$) corresponding to the elevation where the angular velocity attains a maximum. For the current CW (from above) columnar vortex, the axial vorticity is negative.

The measured vorticity components are used to compute vortex lines (parallel to the vorticity vector at each point). Several vortex lines, originating within the near wall region of the radial boundary layer, are shown in Figure 5.15 along with vertical slices of axial vorticity at θ = 0, $\pi/2$, π, and $3\pi/2$. The vortex core is distinguished by axial vorticity centered at $\eta = 0$, and can be considered as a concentration of vortex filaments stretched vertically. Within the viscous section of the radial boundary layer, the vortex lines form horizontal clockwise spirals, similar to the pathlines shown in Figure 5.13. The directional agreement between the vortex and streamlines does not occur for a vortex undergoing counter-clockwise (cyclonic) rotation, as the inward radial entrainment generates negative azimuthal vorticity within the viscous boundary layer regardless of the direction of the vortex rotation. In contrast, in a nonrotating thermal plume, the vortex lines within the boundary layer of the radially-entrained flow form azimuthally-closed circles (or rings) centered around $\eta = 0$. These rings of azimuthal vorticity are compressed as they advect radially inward, before they are transported vertically by the axial flow. The swirling flow induced by the azimuthal flow vanes prevents the formation of closed, circular vortex rings around the axis of symmetry and allows for the spiraling vortex lines to be tilted axially. These vortex lines spiral inward at a nominally invariant pitch until reaching the domain directly beneath the core of the columnar vortex, where they are tilted. Once inside the vortex core, the helical (axial and azimuthal) vortex lines are stretched by axial gradients of vertical velocity. Note that, owing to the sign of the two layers of azimuthal vorticity, vortex lines that originate from within the positive azimuthal vorticity layer (above the local peak in the radial velocity component, cf. Figures 5.11c and 5.12) lead to vortex lines that spiral in an opposite

direction than those shown in Figure 5.15, and are ultimately tilted vertically outside the core ($\eta > 1$) of the vortex.

The tilting of horizontal vortex lines into the vertical direction is a result of the large gradients in velocity accompanying the vortex contraction. The axial vorticity transport equation shows that radial vorticity can be tilted in the vertical direction by radial gradients in the axial velocity: $\omega_r(\partial w/\partial r)$. This term is computed from the SPIV data and displayed using a color raster plot in Figure 5.16a. This figure also shows overlaid contour lines of the axial component of the vorticity vector (with an increment of $\Delta\,\omega_z/\Omega$ = -1, starting at ω_z/Ω = -3). These data show that the magnitude of the tilting term is significant within the domain directly below the vortex core ($\eta < 1$, $\zeta < 0.02$), where the horizontal vortex lines in Figure 5.15 are tilted into the axial direction. The data in Figure 5.16a confirm that it is the interaction between the radial vorticity and radial gradient of the axial velocity that leads to conversion of horizontal vorticity within the surface boundary layer into axial vorticity within the core of the columnar vortex. It is also evident that additional tilting occurs above the location of the vortex contraction. At this location, a concentration of negative radial vorticity, centered about η = 0.2 and ζ = 0.025 (cf. Figure 5.14a), is generated due to the rapid radial expansion of the vortex column, and produces large axial gradients in tangential velocity ($\omega_r = -\partial v/\partial z$). This additional tilting is visible in Figure 5.15, where the vortex lines, once tilted axially, are directed radially outward above the vortex contraction before becoming nominally two-dimensional (axial and azimuthal) and forming a helical pattern in the remainder of the vortex column ($\zeta > 0.03$; $z/h > 0.044$). The axial circulation is computed from the radial distribution of tangential velocity as $\Gamma_z = 2\pi \int -\partial(rv)/\partial r\, dr$ =

$-2\pi\Omega R^2 \int \partial(\eta\hat{v})/\partial\eta \, d\eta$, (assuming axisymmetry) and is shown in Figure 5.16b. The contours clearly depict the tilting of the near-surface, horizontal vorticity within the viscous boundary layer into the vortex core. In fact, a given contour indicates the transition from low to high aspect ratio (axial to radial) cylindrical domains that bound the horizontal vorticity concentrations within the surface boundary layer and the axial vorticity concentrations within the core of the vortex. This is indicative of the change from the cross-stream scale of the boundary layer to the scale of the core of the vortex ($z/r = 0.23$ for $\Gamma_z/2\pi\Omega R^2 = 1$).

Since only the radial vorticity component contributes to the formation of axial vorticity within the core of the columnar vortex (the azimuthal vorticity does not change direction while it is advected into the vortex core), the radial circulation, Γ_r, through the cross-section of a vortex tube within the surface boundary layer should equal the axial circulation, Γ_z, along the same variable-radius streamtube within the vortex core. For an axisymmetric flow,

$$\Gamma_r = \iint \omega_r r d\theta dz = -\oint_{2\pi}^{0} v r d\theta = 2\pi r v = 2\pi\Omega R^2 \eta\hat{v}$$

and (5.1)

$$\Gamma_z = \iint \omega_z r d\theta dr = \oint_{0}^{2\pi} v r d\theta = 2\pi r v = 2\pi\Omega R^2 \eta\hat{v}.$$

The integrals of the radial and axial vorticity components are computed over the circumferential and top surfaces of a cylindrical control volume, respectively, of variable radius $0 < r < 18$ cm ($0 < \eta < 4$) and a fixed height $0 < z < 5$ cm ($0 < \zeta < 0.06$). As shown in Figure 5.17, the radial distributions of the normalized radial and axial circulations are nearly identical, demonstrating that the flux of radial vorticity into the

columnar vortex is the sole source of the axial vorticity within the vortex core. Therefore, the contours of constant Γ_z in Figure 5.16b bound axisymmetric cylindrical bundles of vortex lines that bound the vertical core and the momentum boundary layer. Hence, the strength of the columnar vortex is completely determined by the production and tilting of the radial vorticity due to the azimuthal flow within the swirling boundary layer.

Radial distributions of normalized axial ($\hat{\omega}_z$) and azimuthal ($\hat{\omega}_\theta$) vorticity components within the developed vortex column are computed at $\zeta = 0.12$ in the baseline vortex $\varphi = 30°$ and $Gr = 9.7 \cdot 10^7$) and shown in Figure 5.18. Within the inner core of the vortex, the axial vorticity rapidly decreases from its maximum along the centerline to $0.2\hat{\omega}_{z,max}$ at $\eta = 1$. Outside the vortex core, the magnitude of the axial vorticity continues to decrease before vanishing completely at $\eta = 2$, corresponding to the location where the radial distribution of tangential velocity resembles a potential vortex. Within the vortex column, the azimuthal vorticity, $\frac{\partial u}{\partial z} - \frac{\partial w}{\partial r}$, is dominated by the radial gradient of axial velocity. It is negative within the inner core, with a local minimum at $\eta = 0.55$ before changing sense at $\eta \approx 0.85$ at the maximum axial velocity (cf. Figure 5.1a). The magnitudes of the peak negative and positive azimuthal vorticity concentrations within and outside the core are comparable, and $\hat{\omega}_\theta$ decays and vanishes for $\eta > 3$. This distribution of $\hat{\omega}_\theta$ is consistent with the negative and positive vorticity layers within the radial boundary layer, where the negative ω_θ produced within the viscous layer is advected into the vortex core while the positive ω_θ advects to the domain $\eta > 1$. These data show that the flow region outside the vortex core is not strictly irrotational. As

demonstrated in Figure 5.17, within the vortex core the axial circulation does not increase linearly with η and reaches only $0.67\Gamma_{z,\max}$ at $\eta = 1$. Beyond the radial peak in the tangential velocity, the axial circulation becomes invariant with η, as ω_z vanishes at $\eta = 2$. The asymptotic level of the axial circulation is referred to as the total circulation, or vortex strength, and the baseline single-cell vortex has a core Reynolds number [$Re = \Gamma_z/(2\pi\nu)$, cf. Chapter 2] on the order of 2500.

Color raster plots of time-averaged distributions of the axial vorticity are shown at five equally-spaced elevations $\Delta\zeta \approx 0.05$ apart, starting at $\zeta = 0.07$ (Figure 5.19a). These images show that within this domain the axial vorticity remains nominally invariant with elevation, with a small decrease in magnitude as a result of the spreading of the vortex core. Figure 5.19b shows that the corresponding core Reynolds number (i.e., axial circulation) remains roughly invariant (slightly decreasing) in the vertical direction. This is in agreement with the vorticity production mechanism discussed above, since no additional axial vorticity is generated once the near-surface radial vorticity is turned upwards.

The mechanism for vorticity production in columnar buoyant vortices discussed in this chapter is in good agreement with the mechanism previously proposed by Rotunna (1980). A significant attribute of this mechanism is that it does not rely on the presence of ambient axial vorticity or ambient horizontal wind shear as suggested earlier by Maxworthy (1973). Furthermore, this mechanism enables continued sustainment of the columnar vortex as long as the buoyant instability is present (i.e., the surface is heated) and does not necessitate the production of randomly directed horizontal vorticity via unpredictable vertical wind shear or through induced baroclinic effects. The

production, and ultimately, distribution, of the axial vorticity is the link that enables the conversion of thermal energy from the heated surface into significant kinetic energy within the vortex flow. Furthermore, these findings suggest that the vortex structure and strength, and therefore its kinetic energy, can be intensified by alterations in the production and advection of radial vorticity within the surface boundary layer (cf. Chapter 7).

5.3 Formation Parameters

For given formation parameters that control the entrained flow, namely the thermal resources as measured by the Grashof number and the angle φ imposed by the vanes, the single-cell vortex forms at small vane angles that limit both the angular momentum of the entrained flow and the pressure drop across the vanes. As discussed in connection with Figure 4.2, in the 1-m scale laboratory facility (l = 35 cm x h = 60 cm, cf. Chapter 3), single-cell vortices form for $0 < \varphi \leq 30°$ over the entire range of Gr tested. The objective of this section is to significantly expand the previous analysis of the structural features of the single-cell to a wider range of formation parameters before proceeding to examine in Chapter 6 the changes brought about by the appearance of the downdraft cell.

The dependence on the formation parameters of the distribution of axial vorticity within the core of the single-cell vortex is investigated using SPIV. The measurements are taken in the r-θ plane (z = 10 cm, z/h = 0.17) and are shown using color raster plots of the time-averaged axial vorticity $\omega_z(r, \theta, z = \text{const})$ [normalized by the angular velocity of φ = 30° at $Gr = 9.7 \cdot 10^7$, Ω = 15 s^{-1}] overlaid for reference with radial distributions of the time-averaged tangential velocity for φ = 10°, 20°, and 30° at

$Gr = 9.7 \cdot 10^7$ (Figure 5.20a), and for $Gr = 4.8$, 9.7, and $11.6 \cdot 10^7$ at $\varphi = 30°$ (Figure 5.20b). The rectangular measurement domain measures R_i x $0.5R_i$ and the z axis is located at $0.25R_i$, along the long bisector. Note that as φ is increased from 10° to 30°, the inner radius of the enclosure R_i increases from $0.31h$ to $0.41h$, so the physical dimensions of the measurement domain are enlarged accordingly. These data show that the vortex intensifies significantly with increasing vane angle. At $\varphi = 10°$ (Figure 5.20a) the rotation induced by the entrained flow is small ($\Omega = 2.7$ s^{-1}) and, as a result, the concentration of the axial vorticity within the vortex core ($R = 0.21R_i = 0.063h$ based on the radial location of v_{max}) is not axisymmetric, indicating some meandering of the weak vortex and inadequate sampling rate for time-averaging. As the vane angle increases to $\varphi = 20°$ the vortex core becomes more organized and has a larger cross-section ($R = 0.19R_i = 0.070h$), which increases further when $\varphi = 30°$ ($R = 0.18R_i = 0.082h$). The increase in azimuthal flow with φ results in increased production of radial vorticity concentrations within the boundary layer and leads to a rise in the axial vorticity within the vortex column. It is noted that the raster plots in Figures 5.20a exhibit some weak concentrations of axial vorticity within the (annular) outer flow that may be advected by the entrained flow along the vanes and stretched by the axial flow. The variation of the axial vorticity distribution with Gr is shown in Figures 5.20b for a fixed vane angle ($\varphi = 30°$) and height ($z/h = 0.17$). These data demonstrate a significant increase in the intensity of the axial vorticity with Grashof number, including a nearly five-fold increase in the magnitude of the peak vorticity between $Gr = 4.8 \cdot 10^7$ and $11.6 \cdot 10^7$. It is evident that the increase in the axial acceleration due to increased Gr contributes to amplification of vorticity production by increasing the flux of entrained flow and, therefore, the

rotation above the surface, and also by inducing larger radial gradients of the axial velocity which enhance tilting of the horizontal vorticity in the axial direction (cf. Figure 5.16a). Furthermore, as *Gr* increases, the nominally axisymmetric time-averaged vorticity distribution within the core develops azimuthal undulations, indicating that the core flow becomes increasingly unsteady.

The dependences of the characteristic scales (cf. Chapter 2) on the vane angle and temperature difference are examined for $5° < \varphi < 30°$ (at increments of 5°), and for $4.82 \cdot 10^7 \leq Gr \leq 11.6 \cdot 10^7$ (surface temperatures $50°C < T_p < 150°C$, at increments of 25°C). Throughout this investigation, the variation of the vane angle is expressed as $\tan\varphi$,which describes the ratio of azimuthal to radial velocity (i.e., horizontal swirl number v/u) imparted to the entrained air. The variations of the normalized core radius, $\widehat{R} = R/R_0$, and maximum tangential velocity, $\hat{v} = v/v_0$, axial velocity, $\widehat{w} = w/w_0$, and weight deficiency, $\widehat{g'} = g'/g'_0$ with $\tan\varphi$ for $Gr = 9.7 \cdot 10^7$ ($T_p = 100°C$) are shown in Figures 5.21a-c, and with *Gr* for $\varphi = 30°$ in Figures 5.21d-f. Each of the data sets is fitted to powers of $\tan\varphi$ or *Gr* (with a corresponding offset). The data in Figures 5.21a-c show that for a given *Gr*, $\hat{R}$, $\hat{v}$, $\widehat{w}$, and $\widehat{g'}$ increase monotonically with vane angle, indicating that the increased tangential momentum of the entrained flow leads to intensification of the vortex and that the concomitant increase in pressure drop across the vanes (as the gap between adjacent flow vanes decreases) is overcome by a proportionally stronger vortex core. These data are normalized by the asymptotic characteristic scales R_0, w_0, and g'_0 of a nonrotating thermal plume that forms by natural convection at $\varphi = 0°$ for the given *Gr*. Tangential velocity v is normalized by w_0 because $v = 0$ when $\varphi = 0°$. The increase in the radius of the vortex core with vane angle

$R = \tilde{R}(\tan\varphi)^{5/3} + R_0$ is concomitant with the corresponding change in the radius of the enclosure ($R_i \propto \tan\varphi$) but at a reduced rate of increase [$\tilde{R}$ is a constant]. The corresponding characteristic radius of the nonrotating, thermal plume, R_0, for $\varphi = 0°$ at $Gr = 9.7 \cdot 10^7$ is nominally 3.8 cm. The asymptotic characteristic scales w_0 for $\varphi = 0°$ is 8 cm/s and the rate of increase of the axial velocity is considerably lower than that of the tangential velocity ($\tilde{w}/\tilde{v} = 0.23$). This indicates that despite the strong increase in tangential velocity with φ for a given *Gr*, the axial flow and ostensibly the volume flow rate into the enclosure, are less sensitive to variations in vane angle. The weight deficiency g' at the vortex centerline (r = 0) increases like $g' = \tilde{g}'(\tan\varphi)^2 + g'_0$ and its magnitude in the absence of induced swirl is $g'_0 = 0.64$ m/s^2 ($\hat{T}$ = 0.2). Clearly, since these data are acquired for *Gr* O[10^7] (cf. Figure 4.2) the asymptotic behavior as $Gr \rightarrow 0$ cannot be assessed. The characteristic scales in Figure 5.21d-f (i.e., R_0, w_0, and g'_0, respectively) are therefore normalized by the corresponding values at $Gr = 10^7$ ($T_p \approx 28°$C). For a fixed vane angle ($\varphi = 30°$, $\tan\varphi = 0.58$, Figures 5.21d-f) the vortex core radius decreases with increasing *Gr* ($R = R_0 - \tilde{R}Gr^{7/2}$) indicating that the increase in thermal forcing augments the radial pressure gradient (i.e., tangential velocity [$v = \tilde{v}Gr^3 + v_0$]) which lead to narrowing of the vortex core. Simultaneously, the axial velocity increases substantially with *Gr* ($w = \tilde{w}Gr^3 + w_0$) corresponding to the increase in weight deficiency with surface heating ($g' = \tilde{g}'Gr^{5/2} + g'_0$), indicating that the volume flow rate (and kinetic energy flux) are increased significantly as the temperature difference increases.

Three integral scales used to describe the columnar vortex (Figure 5.22) include the axial circulation calculated from the time-average axial vorticity in the r-θ plane

[$\Gamma_z = \iint \omega_z dA$], the radial integral of kinetic energy flux [$\dot{E} = \iint \frac{\rho}{2}(v^2 + w^2)(\vec{V} \cdot \hat{n})dA$], and the buoyancy flux [$B = 2\pi\rho \int wg'rdr$]. Variations of the axial circulation [normalized as core Reynolds number $\Gamma_z/(2\pi\nu)$], with vane angle for fixed *Gr*, and with *Gr* for $\varphi = 10°$, 20°, and 30° are shown in Figures 5.22a and b ($z/h = 0.17$). These data demonstrate the amplification of vorticity production (cf. Figure 5.20) with a monotonic rise in core Reynolds number when either formation parameter increases. For constant *Gr* (Figure 5.22a) the core Reynolds number varies like $(\tan\varphi)^{3/4}$ ($\Gamma_z = 0$ at $\varphi = 0°$) compared to $(\tan\varphi)^{2/3}$ reported by Mullen and Maxworthy (1977) for a similar experimental facility. For a given φ (Figure 5.22b), the core *Re* varies nearly linearly with *Gr* (the proportionality constant *a* varies between $5.9\cdot10^{-6} \le a \le 14.5\cdot10^{-6}$ for $10° \le \varphi \le 30°$), and for the single-cell vortex at $\varphi = 30°$ this results in a 60% increase in *Re* ($\Gamma_{z,150°C} = 1.57\Gamma_{z,50°C}$). As the production of axial vorticity occurs only within the spiraling boundary layer, the dependence of *Re* on the formation parameters in Figure 5.22a and b is invariant with elevation as long as the single-cell structure is maintained (cf. Figure 5.19b). Similarly, the variations of the integral of the kinetic energy flux $\dot{E}$ (through a circular cross-section of radius $r/R_i = 0.6$) with φ and *Gr* are shown in Figures 5.22c and d, respectively ($\dot{E}$ is normalized by the gravitational potential energy flux $g\rho\nu R_i^2$, $\hat{\dot{E}} = \dot{E}/g\rho\nu R_i^2$). These data show that the mechanical energy increases sharply with both the vane angle [$\hat{\dot{E}} \sim (\tan\varphi)^{2/3}$] and Grashof number ($\hat{\dot{E}} \sim Gr^2$). Specifically, the power in the flow increases significantly with the temperature difference ($\dot{E}_{150°C} = 3.65\dot{E}_{50°C}$ for $\varphi = 30°$). Finally, the third integral measure considered is the radial integral of the buoyancy flux $B = 2\pi\rho \int_0^\infty wg'rdr$, which is a measure of the

buoyancy-induced vertical "thrust force" (analogous to momentum flux) available to accelerate the flow vertically, and which is often used in the analysis of thermal plumes (Turner 1973). The variation of the normalized integral of the buoyancy flux $\hat{B} = B/(2\pi\rho\upsilon g R_i)$ with the normalized surface temperature $\hat{T}_p$ [$(T_p\text{-}T_\infty)/(150°\text{C}\text{-}T_\infty)$, where 150° is the maximum T_p investigated] is shown in Figure 5.22e. For a given φ, $\hat{B}$ varies nearly linearly with $\hat{T}_p$, and its rate of change $\hat{T}_p$ increases with φ. Note that these traces share a common abscissa intercept at $\hat{T}_p \approx 3.6\cdot10^{-2}$ ($T_p \approx 27.6°\text{C}$; $Gr \approx 0.94\cdot10^6$) just below the lower end of the present range of the Grashof number. This common intercept may be interpreted as the minimum thermal forcing needed to induce the formation of vortices of varying sizes and strengths, which will depend on the formation parameters set by the facility.

Figures 5.23a and b show the radial variation of the *local* swirl and Froude numbers $S(\eta)= v(\eta)/w(\eta)$ and $Fr(\eta)=(\alpha \cdot w(\eta)^2/2R \cdot g'(\eta))^{1/2}$, respectively, (which scale the axial momentum equation (2.10); cf. Figure 5.10) for a range of Grashof numbers [$Gr = 4.8\cdot10^7$ (50°C), $7.8\cdot10^7$ (75°C), $9.7\cdot10^7$ (100°C), $10.9\cdot10^7$ (125°C), and $11.6\cdot10^7$ (150°C)] at three different vane angles [φ = 10°, 20°, and 30°] for which a single-cell vortex is maintained. Both $S(\eta)$ and $Fr(\eta)$ increase with vane angle, but the most salient feature is the collapse of the data for each φ, which indicates that *for a given vane angle*, the local swirl and Froude numbers $S(\eta)$ and $Fr(\eta)$ are invariant with Gr over the range investigated. As the gravitational potential energy within the flow increases due to additional surface heating, there is a proportional increase in the axial kinetic energy, such that the adjusted Froude number remains invariant. Furthermore, due to the invariance of the local swirl number with Gr, the increase in the axial kinetic energy (w^2)

with *Gr* corresponds to a proportional increase in tangential kinetic energy (v^2), and therefore, increases the induced radial pressure gradient (for cyclostrophic balance $\rho v^2/r = \partial p/\partial r$).

When each of the radial distributions of the time- and azimuthally-averaged tangential and axial velocity components and the weight deficiency are normalized by their individual characteristic maxima [$v(\eta = 1)$, $w(\eta = 1)$, and $g'(\eta = 0)$], these distributions collapse on each other to form a single self-similar distribution regardless of the vane angle (or *Gr*), as shown in Figure 5.24. The remarkable collapse of these data indicates self-similarity within the single-cell vortex over a broad range of formation parameters. Since the shape of the radial distribution of axial velocity is determined by the balance between the buoyancy and axial pressure forces (cf. Figure 5.3), the collapse of these data suggests that the balance between these forces in the single-cell vortex is invariant with respect to both of the primary formation parameters, φ and *Gr*.

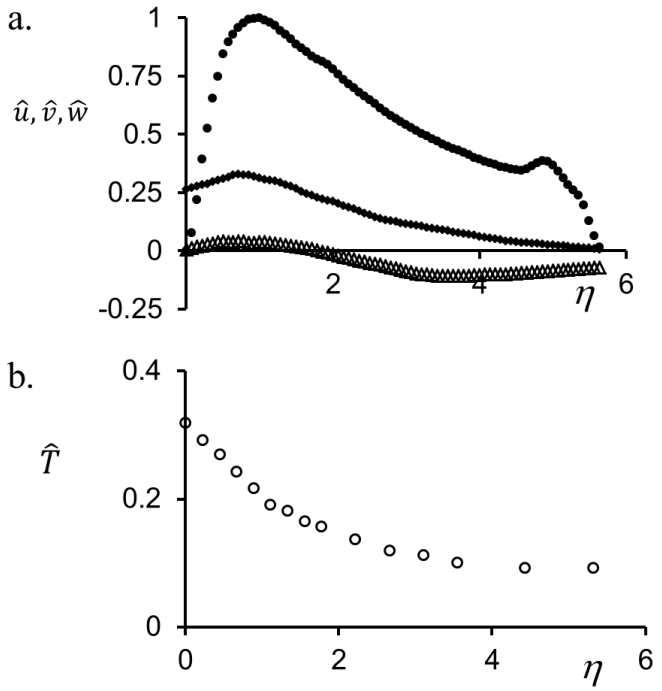

FIGURE 5.1. Time-average radial distributions of the nominal single-cell vortex at $z = 10$ cm ($\zeta = 0.12$): (*a*) Azimuthally-averaged and normalized tangential (●), axial (♦) and radial (Δ) velocity components, and (*b*) normalized temperature (○) within the vortex column ($\varphi = 30°$, $Gr = 9.7 \cdot 10^7$).

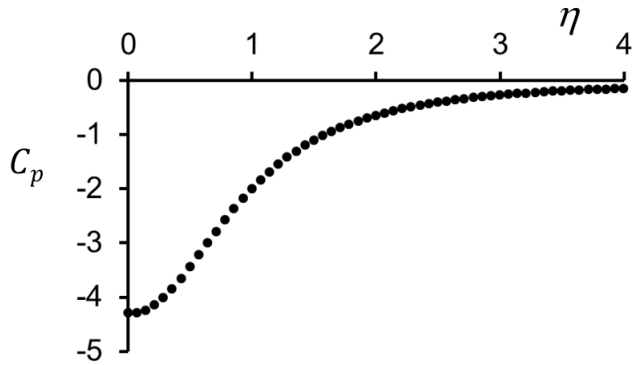

FIGURE 5.2. Radial distribution of the pressure coefficient relative to the ambient pressure ($\varphi = 30°$, $Gr = 9.7 \cdot 10^7$).

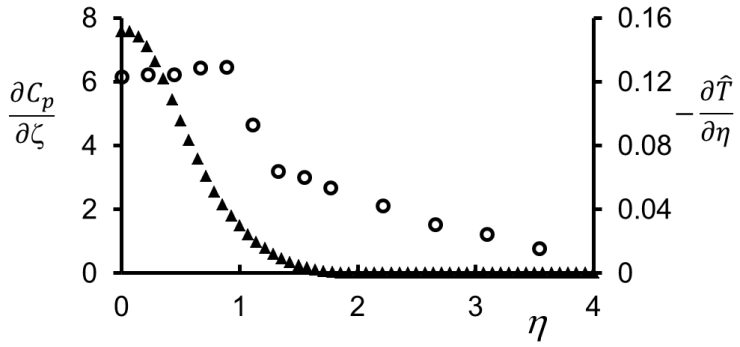

FIGURE 5.3. Radial variation of the radial temperature gradient (○) and axial pressure gradient (▲) ($\varphi = 30°$, $Gr = 9.7 \cdot 10^7$).

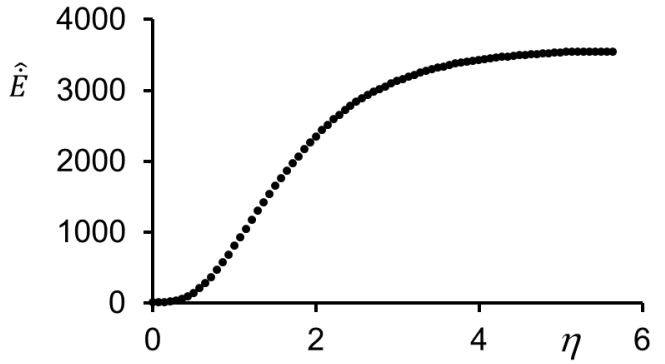

FIGURE 5.4. Radial distribution of the integrated kinetic energy flux through ζ = 0.12 at varying circular control surface radii (φ = 30°, Gr = 9.7·10^7).

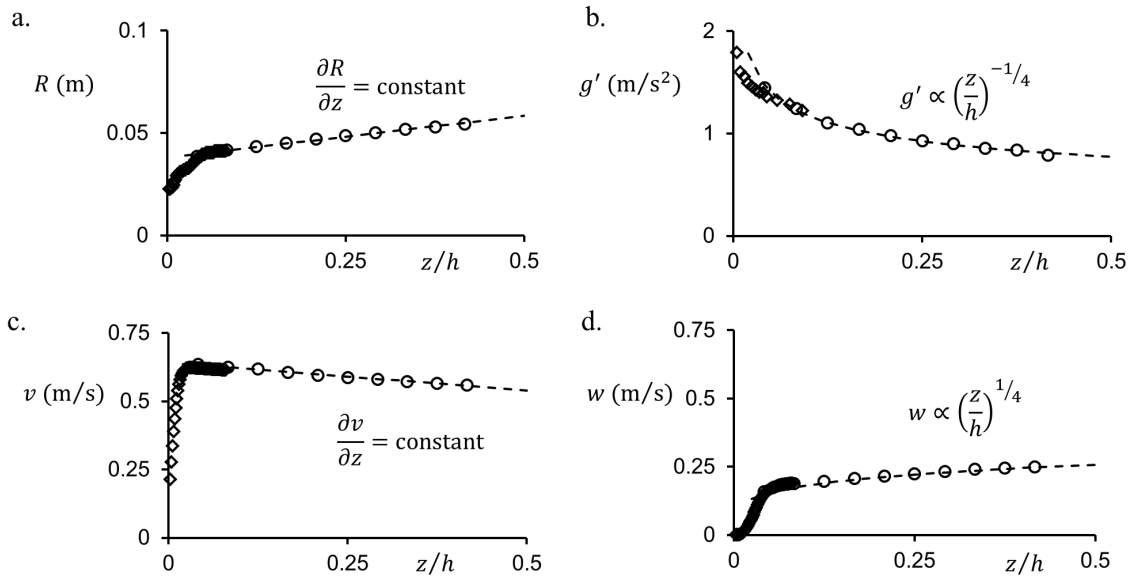

FIGURE 5.5. Axial variations of the characteristic values of the nominal single-cell vortex ($\varphi = 30°$, $Gr = 9.7 \cdot 10^7$): (*a*) vortex core radius, (*b*) centerline weight deficiency, (*c*) tangential and (*d*) axial velocity at $r = R$ ($\eta = 1$). The functional fit of each data set is shown using a dashed line (- -).

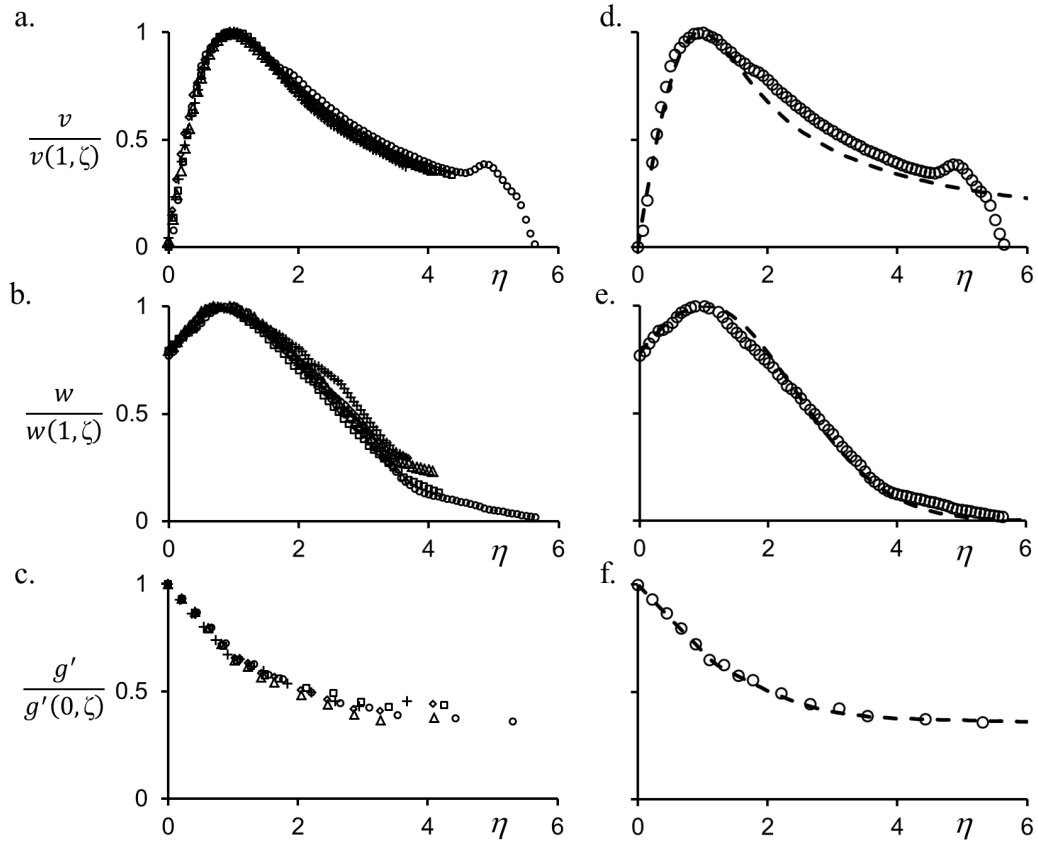

FIGURE 5.6. Radial distributions of the time- and azimuthally-averaged (*a*) tangential and (*b*) axial velocity components, and (*c*) weight deficiency at the elevations: $\zeta = 0.07$ (□), 0.12 (○) 0.17 (Δ) 0.22 (◊), and 0.26 (+). Fitted variation to each measured distribution is shown on the right (*d*, *e*, and *f*) using dashed lines (- -) along with the corresponding measured distribution at $\zeta = 0.12$ (○).

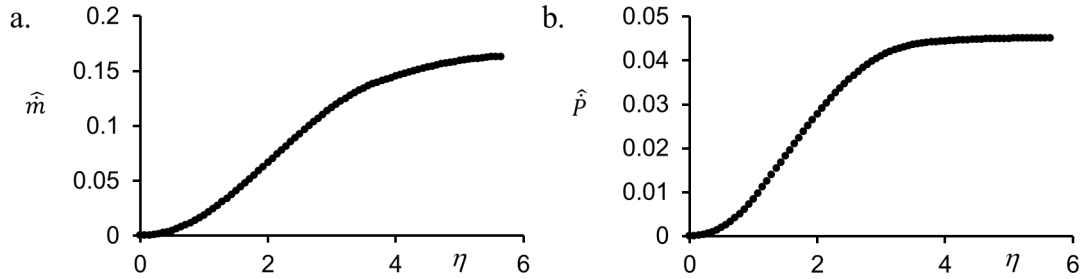

FIGURE 5.7. Radial variation of radial integrals of (*a*) mass and (*b*) axial momentum flux through $\zeta = 0.12$ ($\varphi = 30°$, $Gr = 9.7 \cdot 10^7$).

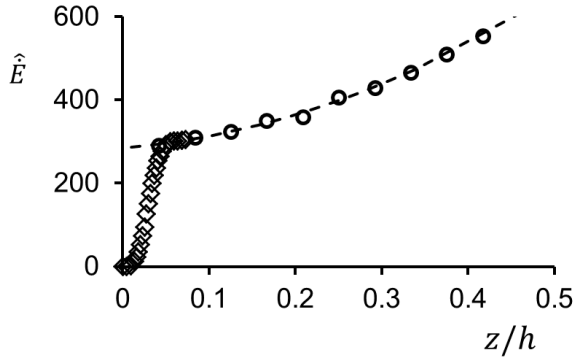

FIGURE 5.8. Variation of the kinetic energy flux with elevation ($\varphi = 30°$, $Gr = 9.7 \cdot 10^7$).

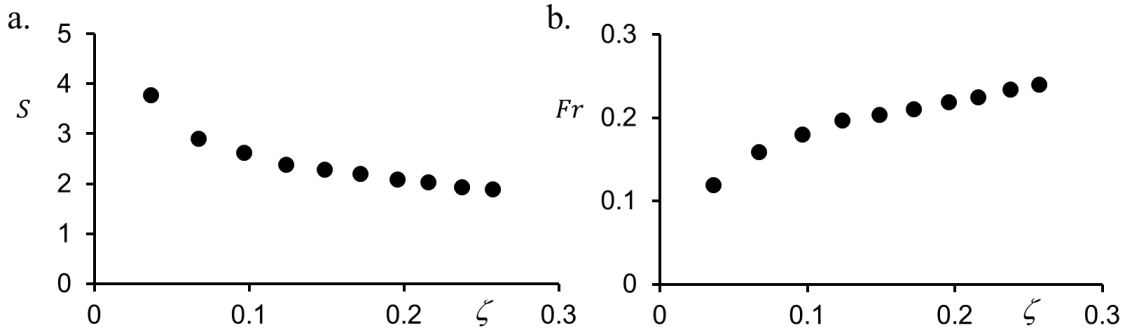

FIGURE 5.9. Axial variation of (*a*) swirl (*S*) and (*b*) Froude (*Fr*) numbers ($\varphi = 30°$, $Gr = 9.7 \cdot 10^7$).

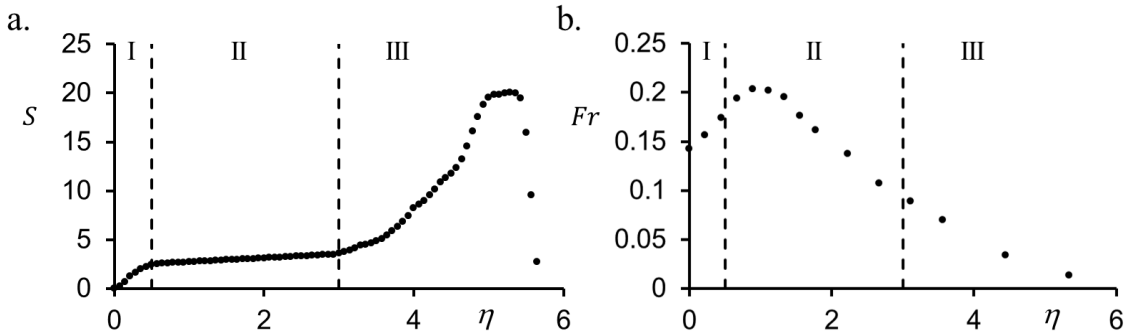

FIGURE 5.10. Radial variation of (*a*) swirl (*S*) and (*b*) Froude (*Fr*) numbers (ζ =0.12, φ = 30°, $Gr = 9.7 \cdot 10^7$).

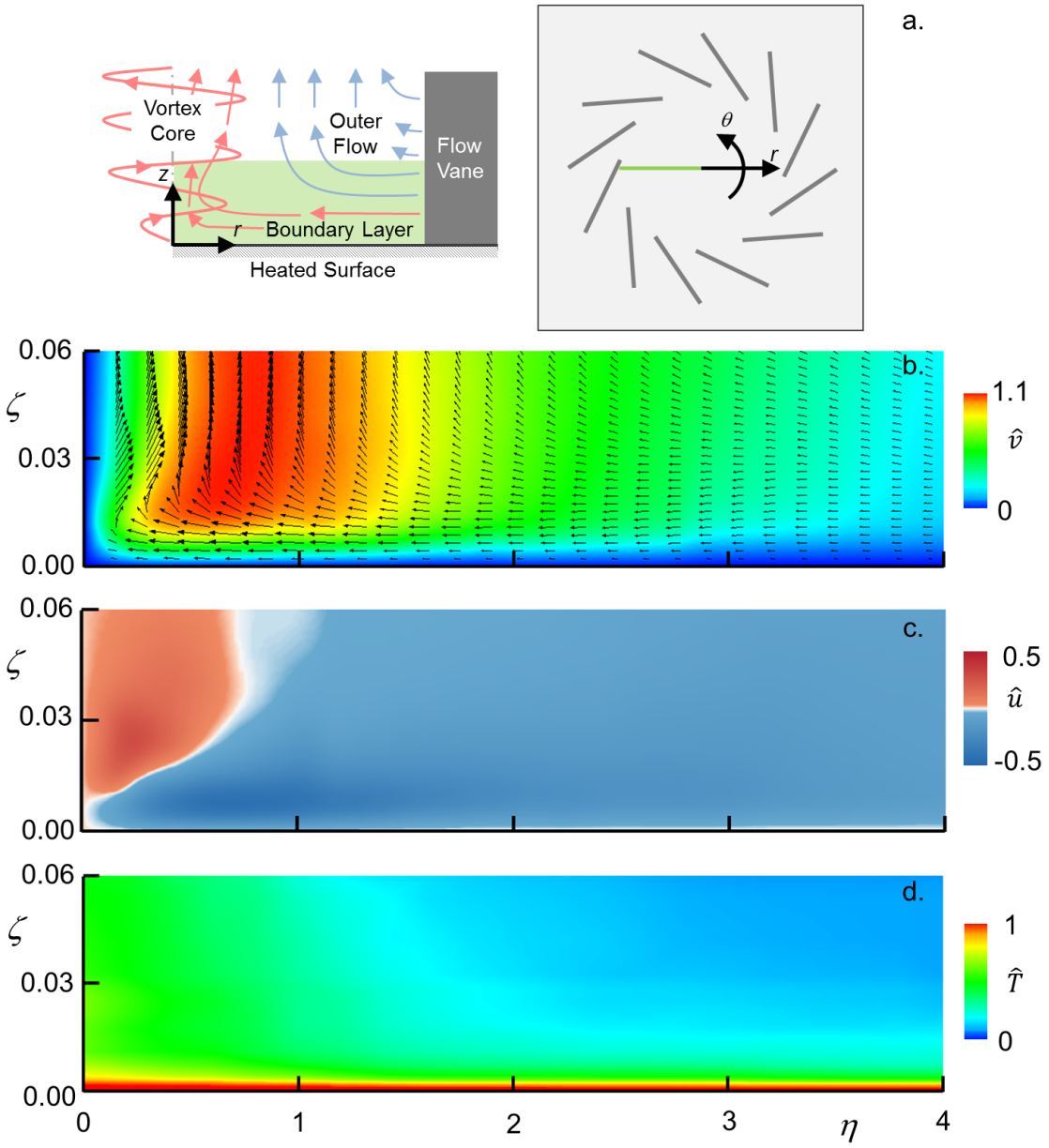

FIGURE 5.11. (*a*) Side and top views of η–ζ measurement plane highlighted in green to denote the location of the laser sheet, and color raster plots of (*b*) normalized tangential velocity distributions superposed with vertical distributions of the in-plane velocity vectors, (*c*) normalized radial velocity distributions, and (*d*) normalized temperature distribution in the η–ζ plane of a single-cell columnar vortex ($\varphi = 30°$, $Gr = 9.7 \cdot 10^7$).

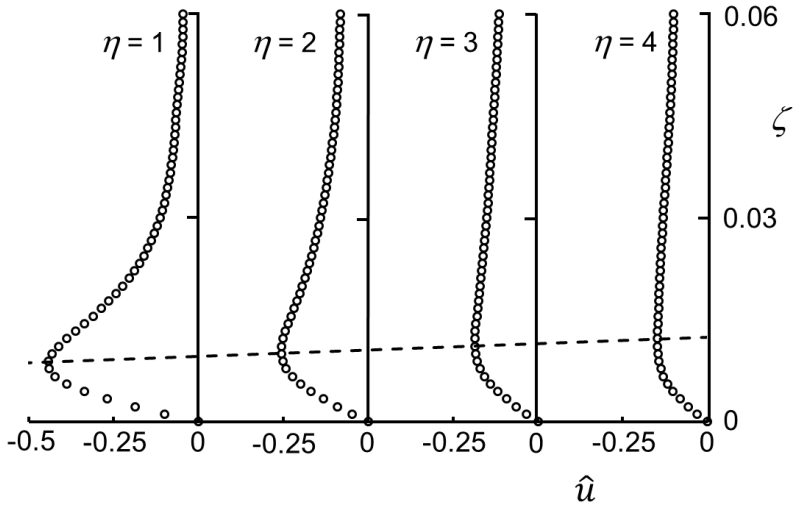

FIGURE 5.12. Axial distributions of radial velocity near the ground-plane at $\eta = 1$, 2, 3, and 4 (○). The dashed line (--) marks the location of the maximum radial velocity at each radial station.

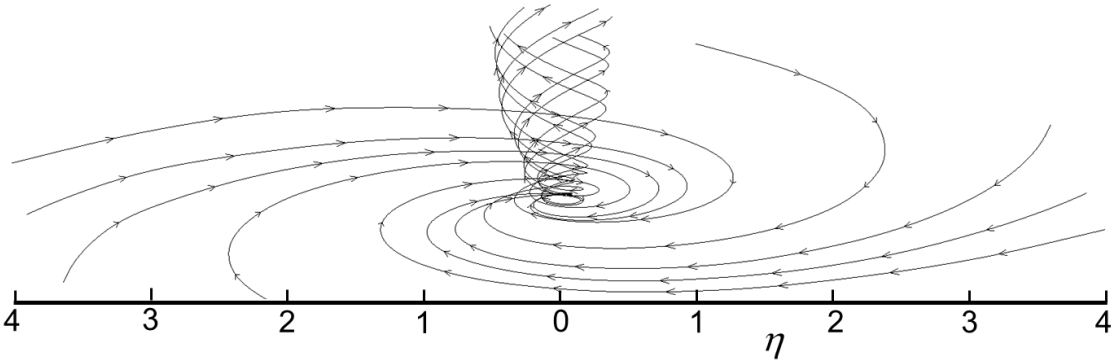

FIGURE 5.13. Isometric view of 3-D pathlines in the axisymmetric flow field showing the near-surface flow evolving into the single-cell columnar vortex located at the center of the cylindrical domain created by the array of vanes.

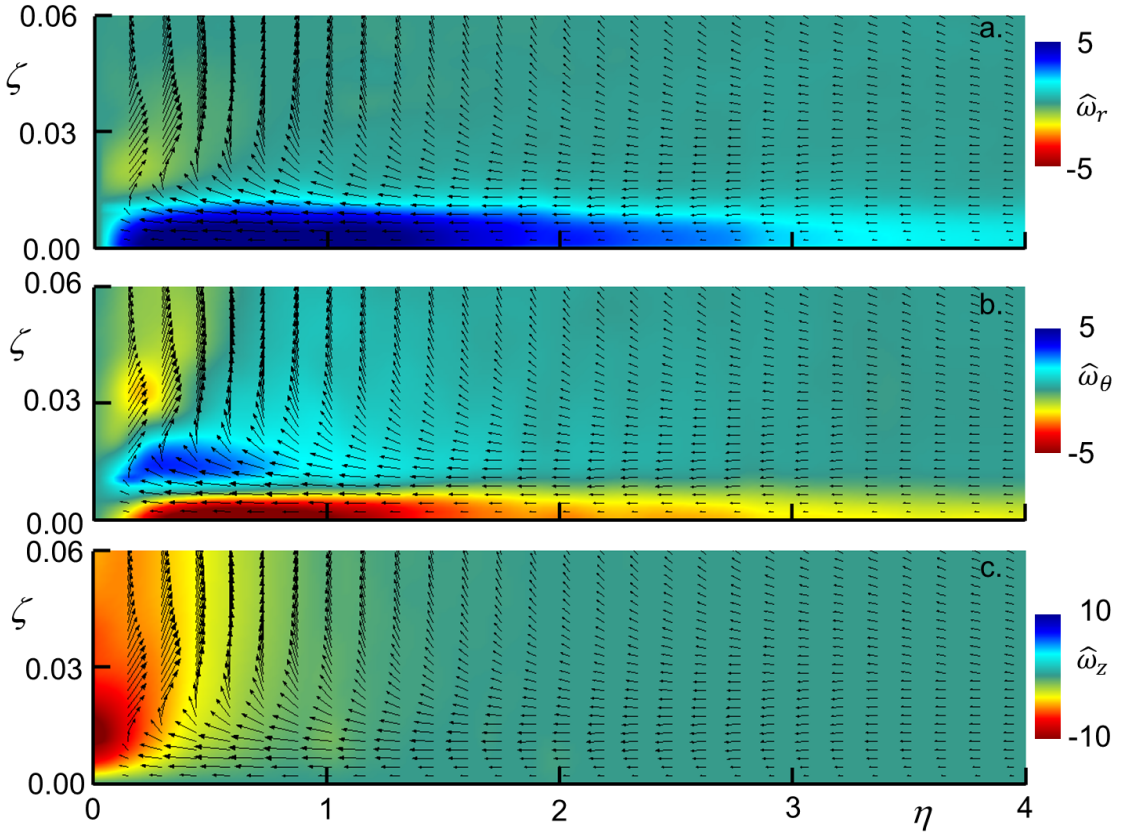

FIGURE 5.14. Color raster plots of vorticity in the η–ζ plane for a single-cell columnar vortex: (*a*) radial, (*b*) azimuthal, and (*c*) axial ($\varphi = 30°$, $Gr = 9.7 \cdot 10^7$).

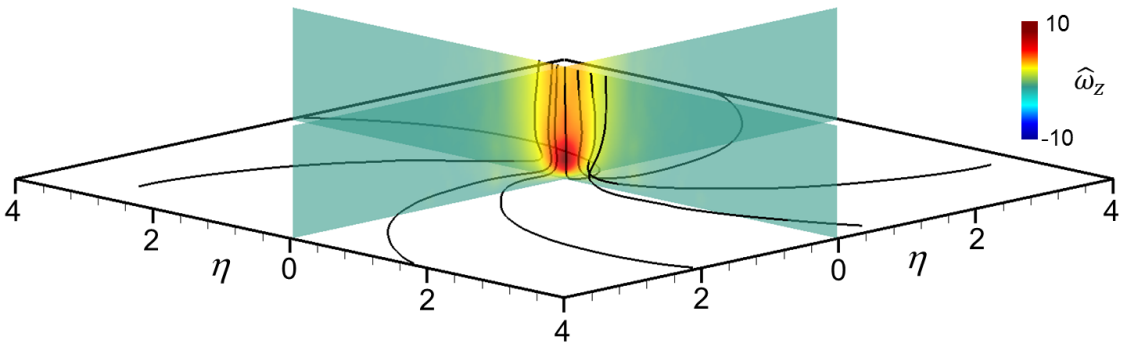

FIGURE 5.15. Calculated vortex lines originating within the radial viscous boundary layer and tilted into the axial direction, with contours of axial vorticity denoting the location of the single-cell vortex core.

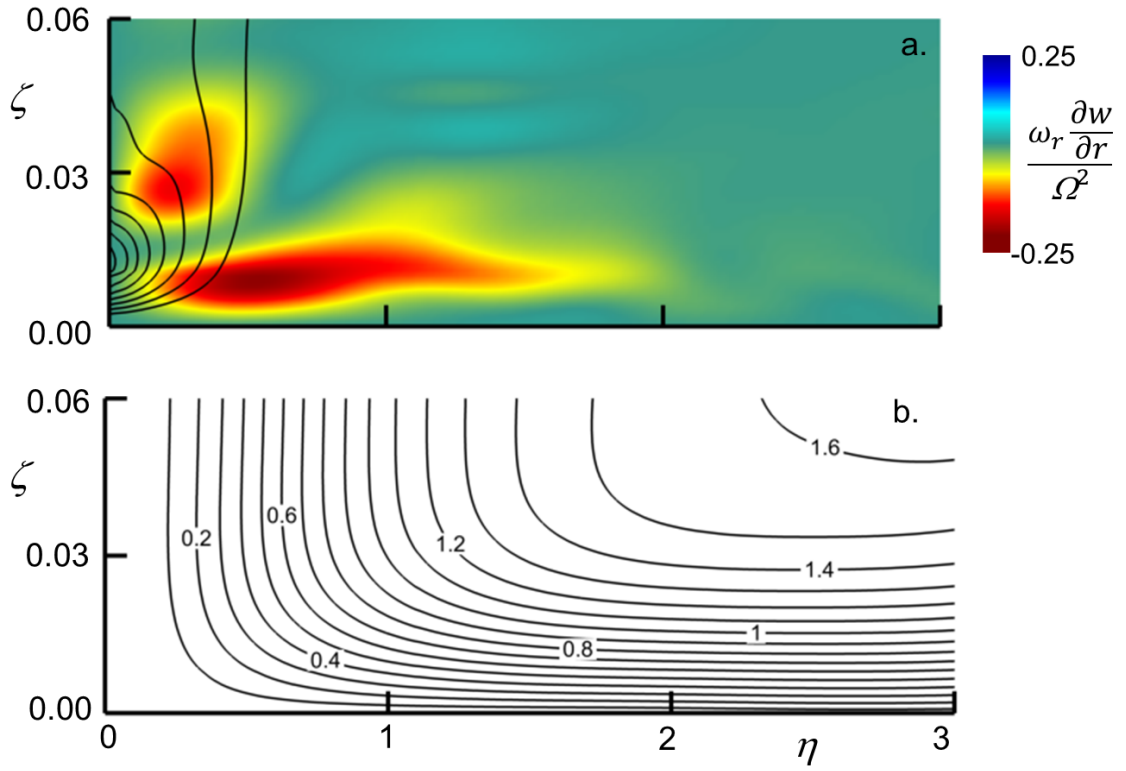

FIGURE 5.16. (*a*) Color raster plot of the radial vorticity tilting term in the axial vorticity transport equation, overlaid with contours of the axial vorticity and (*b*) contours of normalized axial circulation.

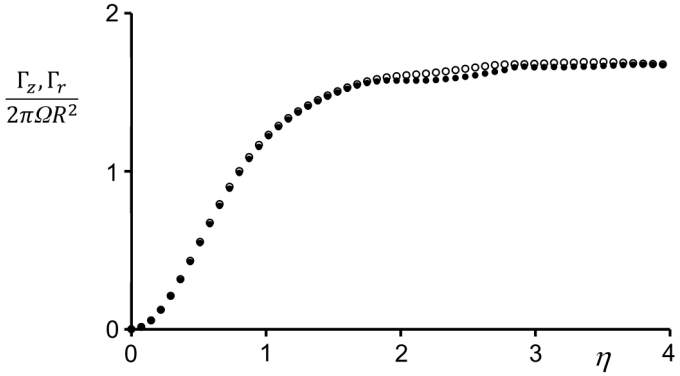

FIGURE 5.17. Comparison of radial circulation (●) and axial circulation (○) at varying cylindrical control surface radii ($\varphi = 30°$, $Gr = 9.7 \cdot 10^7$).

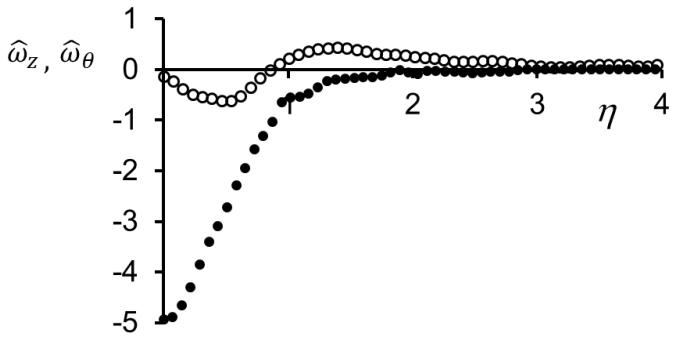

FIGURE 5.18. Radial distributions of axial (●) and azimuthal (○) vorticity (ζ=0.12, φ = 30°, Gr = 9.7·10^7).

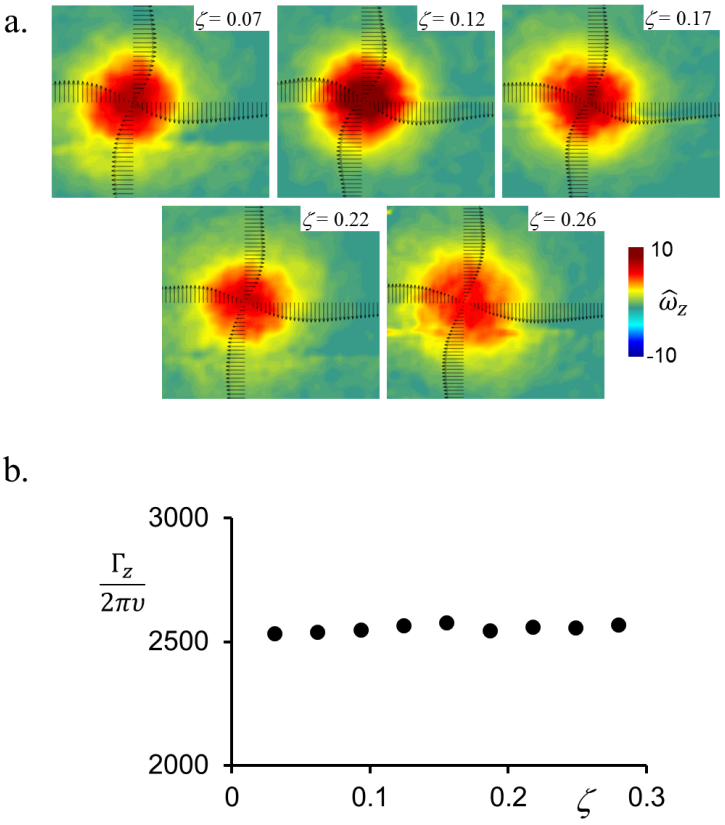

FIGURE 5.19. (*a*) Time-averaged color raster plot of axial vorticity overlaid with radial distributions of tangential velocity vectors showing the vertical evolution of the axial vorticity distribution, and (*b*) the axial variation of core Reynolds number ($\varphi = 30°$, $Gr = 9.7 \cdot 10^7$).

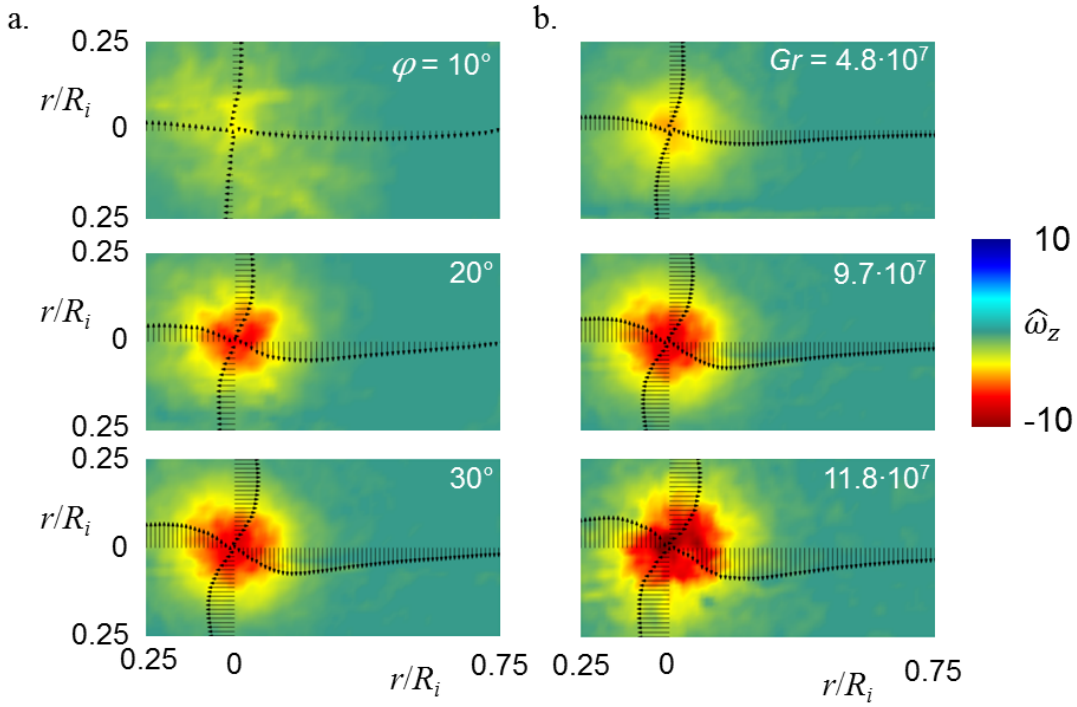

FIGURE 5.20. Time-averaged color raster plot of axial vorticity overlaid with radial distributions of tangential velocity vectors at $z/h = 0.17$ for (*a*) $\varphi = 10°$, 20°, and 30° at $Gr = 9.7 \cdot 10^7$, and (*b*) $Gr = 4.8$, 9.7, and $11.8 \cdot 10^7$ at $\varphi = 30°$.

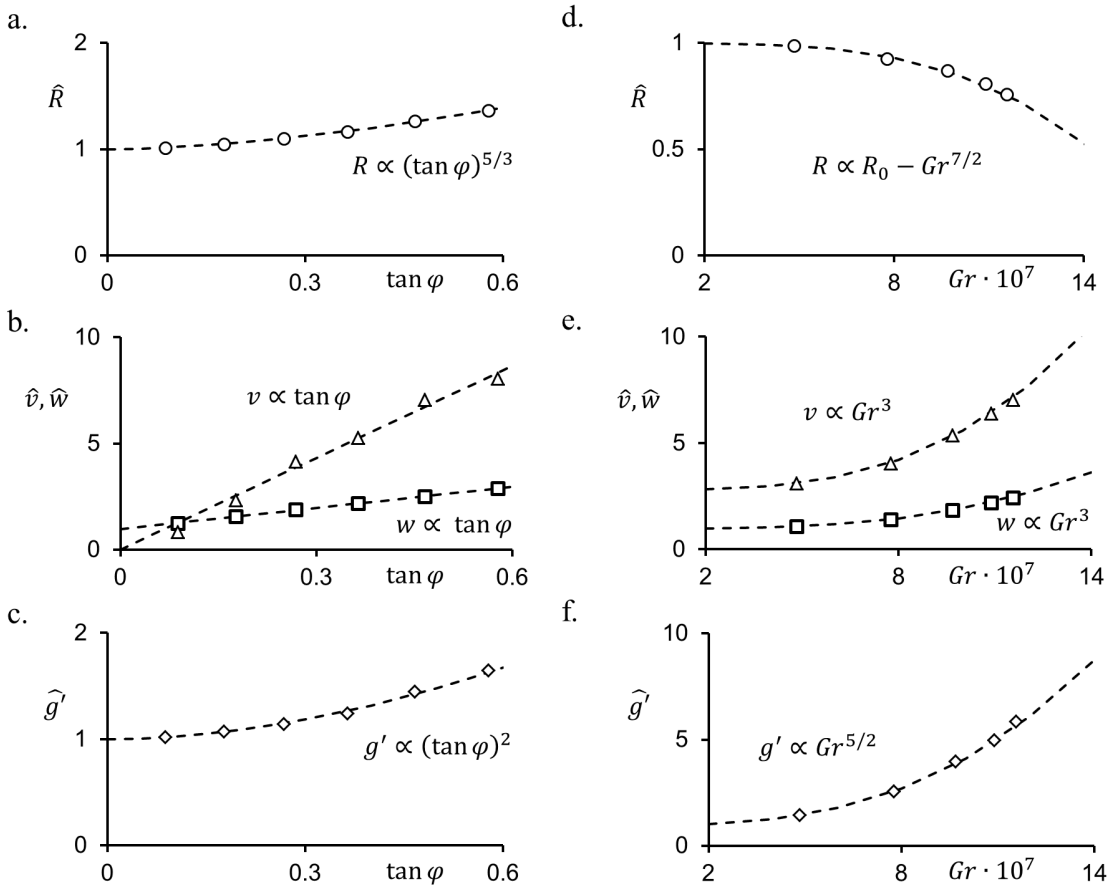

FIGURE 5.21. Variation of (*a*) vortex core radius, (*b*) tangential (Δ) and axial (□) velocity at $r = R$ ($\eta = 1$), and (*c*) centerline weight deficiency with $\tan\varphi$ at $Gr = 9.7 \cdot 10^7$ and (*a*) vortex core radius, (*b*) tangential (Δ) and axial (□) velocity at $r = R$ ($\eta = 1$), and (*c*) centerline weight deficiency with Grashof number, *Gr*, at $\varphi = 30°$ for single-cell vortex structures at $z/h = 0.17$. The functional fit of each data set is shown using a dashed line (--).

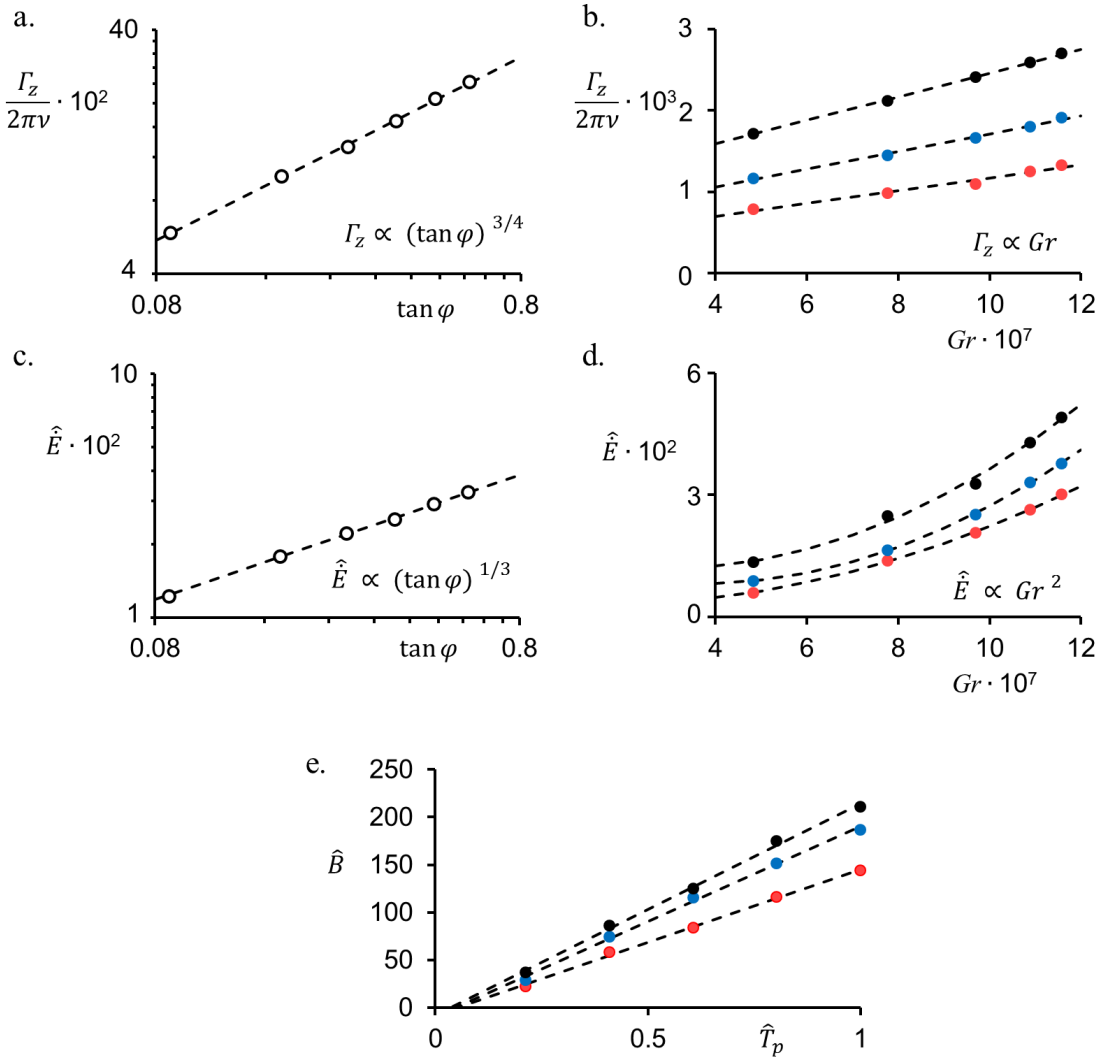

FIGURE 5.22. Variation of (*a*,*b*) core Reynolds number, (*c*,*d*) kinetic energy flux, and (*e*) buoyancy flux with (*a*,*c*) tanφ at $Gr = 9.7 \cdot 10^7$, (*c*,*d*) Grashof number, and (*e*) surface temperature, respectively, at $\varphi = 10°$ (red), 20° (blue), and 30° (black) for single-cell vortices ($z/h = 0.17$).

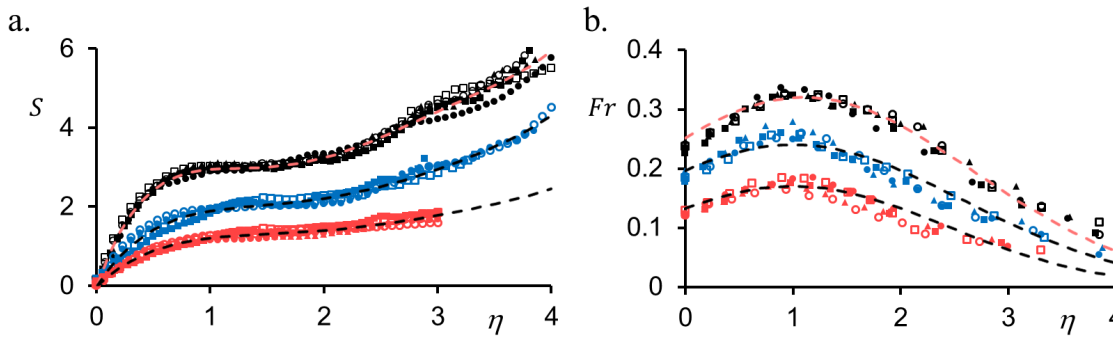

FIGURE 5.23. Radial distributions of local (*a*) swirl and (*b*) Froude number at Gr = 4.8 (■), 7.8 (▲), 9.7 (●), 10.9 (□), and $11.6 \cdot 10^7$ (○) for φ = 10° (red), 20° (blue), and 30° (black).

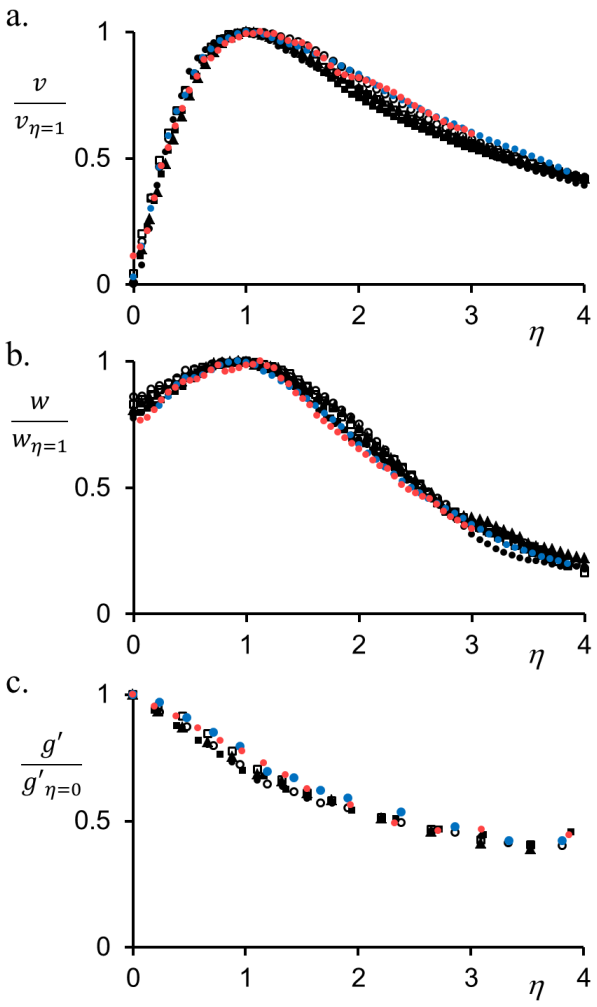

FIGURE 5.24. Radial distributions of the time- and azimuthally-averaged (*a*) tangential velocity, (*b*) axial velocity, and (*c*) weight deficiency of single-cell vortices at $z/h = 0.17$ for $\varphi = 30°$ at $Gr = 4.8$ (■), 7.8 (▲), 9.7 (●), 10.9 (□), and $11.6 \cdot 10^7$ (○) and $Gr = 9.7 \cdot 10^7$ at $\varphi = 10°$ (●), 20°(●), and 30°(●).

CHAPTER VI

Two-Cell Columnar Vortices

A two-cell buoyantly-driven columnar vortex can form as a result of an imbalance between the rotation-induced radial pressure gradient and the available entrained flow (Harlow and Stein 1974). As discussed in Chapter 4, the resulting axially positive pressure gradient can overcome the buoyancy effects within the vortex core and lead to the formation of a recirculating cell of spiraling downdraft flow along the vortex axis, surrounded by an external cell of updraft, buoyancy-driven flow. In the present experiments, the entrained flow and core rotation, and consequently the radial pressure gradient into the vortex core, are regulated by azimuthally adjustable vanes. Therefore, these vanes control the formation and depth of the recirculating downdraft cell and the axial elevation of the characteristic, detached (or "free") stagnation point that forms between the updraft and downdraft flows along the vortex axis (as discussed in connection with Figure 4.2). This chapter focuses on the flow characteristic of two-cell vortices formed in the 1 m scale facility (cf. Figure 3.1), in which the inner recirculating downdraft cell extends into the volume of the azimuthal vane enclosure. Specific attention is given to the near-surface structure of the attached two-cell vortex in which the reverse axial flow reaches the heated ground-plane, and the detached stagnation point migrates to the surface (cf. Figure 4.1b).

The time-averaged, near-surface flow field of a representative attached two-cell vortex ($Gr = 9.7 \cdot 10^7$, $\varphi = 50°$) is measured within a meridional r-z plane, which contains

the vortex centerline $r = 0$, intersects the heated ground-plane ($z = 0$), and passes through the pivot axis of an azimuthal vane (cf. Figure 5.11a). Distributions of normalized velocity vectors (radial and axial velocity components) overlaid on a color raster plot of the normalized axial velocity, $\hat{w}$, in this *r-z* plane, are shown in Figure 6.1a (these data are not averaged azimuthally and the flow field is assumed to be axisymmetric despite the twelve-fold symmetry that is imposed by the vane enclosure). For comparison with the single-cell vortex (cf. Chapter 5), these data are normalized using the core radius R and angular velocity Ω of a single-cell vortex at $Gr = 9.7 \cdot 10^7$, $\varphi = 30°$, for which $R = 0.045$ m and $\Omega = 15\ s^{-1}$ at $z/h = 0.17$. The SPIV measurement domain comprises four individual segments and extends over $0 < r/R_i < 0.6$ and $0 < z/h < 0.1$, capturing the swirling boundary layer, and the lowest extent of the vortex core and outer flow.

The velocity vectors in the *r-z* plane clearly show the presence of axial downdraft along the vortex centerline, terminating at an attached central stagnation point on the ground-plane. The downdraft turns axially upward within the outer segment of the recirculating cell, and the boundary between negative (downward) and positive (upward) axial velocity within the inner cell is marked by the contour $w(r, z) = 0$ (white in Figure 6.1a). The flow surface separating the recirculating downdraft cell and the updraft cell consisting of entrained flow heated along the ground-plane is depicted by the projected stream surface (in the *r-z* plane) originating from the off-axis critical point on the surface at $r/R_i = 0.16$. As noted in Chapter 4, the intersection with the ground-plane of the interface between the recirculating downdraft and updraft cells (cf. Figure 4.1b) forms a circular stagnation line or bifurcation circle (Perry and Chong, 1987). The upward-turning downdraft flow forms a helical jet-like flow bounded on its inner radial

edge (on the left in Figure 6.1a) by the downward flow along the vortex axis and on the outside radial edge (on the right in Figure 6.1a) by the upward-turning buoyancy-driven updraft cell. The interaction between the upward turning flows forms a local contraction near $z/h = 1.2 \cdot 10^{-2}$ before the turned flows expand radially and the updraft cell ultimately reaches a radius of $R/h \approx 0.2$ at $z/h \approx 5 \cdot 10^{-2}$.

Assuming axisymmetric, time-averaged flow within the vane enclosure, the three velocity components are used to construct two sets of particle pathlines, shown in an isometric view within the domain $0 < r/R_i < 0.6$, $0 < z/h < 0.1$ (Figure 6.1b). The first set of particles is seeded near the edge of the measurement domain within the boundary layer ($r/R_i = 0.6$ and $z/h = 0.8 \cdot 10^{-2}$). The horizontal pitch, v/u, of these pathlines (colored blue) is approximately constant ($v/u \approx 4$) within the annular domain $0.3 < r/R_i < 0.6$. For a given Gr these paths are effectively set by the angle of the azimuthal flow vanes that impose the core rotation and, therefore, the strength of the radial pressure gradient. While the magnitude of the tangential velocity component of the swirling momentum boundary layer clearly increases with vane angle, it is important to note that the appearance of the downdraft alleviates the radial pressure gradient, which has the effect of decreasing the radial entrainment along the ground-plane, and which leads to an even larger increase in v/u. The resulting increase in horizontal pitch enables longer residence time along the ground-plane, which in turn increases the heat transfer from the surface and leads to an increase in enthalpy (cf. Figures 4.2d and e) albeit at the cost of increased viscous losses. The second set of particles is seeded within the vortex core ($0.015R_i$) at $z/h = 0.1$ (colored red) and show the recirculating downdraft cell. When these pathlines

reach the base of the vortex column, they are turned outwards and merge with the rising buoyancy-driven flow of the updraft cell to form the helical jet-like flow.

Some features of the flow fields of single-cell ($\varphi = 30°$) and attached two-cell ($\varphi = 50°$) vortices with the same Gr ($9.7 \cdot 10^7$) are compared in Figures 6.2a and b, respectively, using time-averaged in-plane velocity vectors and projections of three-dimensional stream surfaces in the r-z plane. In the single-cell vortex (Figure 6.2a), the vortex core is characterized by the helical, buoyancy-driven updraft flow formed by vertical turning of the radially-entrained spiraling boundary layer along the heated surface. The flow into the updraft cell (shaded red and marked by red streamlines in Figure 6.2a) is bounded from below by the ground-plane and from above by the streamline marked "d", which ultimately turns upward and delineates the radial edge of the vortex core ($r/R_i = 0.14$, $z/h = 0.1$ at the top of the image, and passing through $z/h = 2 \cdot 10^{-2}$ at $r/R_i = 0.6$). Following a local contraction of the entrained flow about the axis of symmetry in close proximity to the surface (cf. Chapter 5), the radial spreading of the core decreases significantly and the streamline "d" separating the inner core flow (shaded red) and the outer flow (white) above the surface boundary layer (including blue-color streamlines for reference) becomes nearly collinear with the contour $u(r, z) = 0$ ("e", marked in green in Figure 6.2a). The entrained flow in the outer domain neither reaches the vortex core nor is directly heated by the ground-plane, but is driven radially and axially through the vanes by the radial pressure gradient imposed by the vortex core rotation, and axially by the buoyancy-driven updraft flow.

In the attached two-cell vortex core, the recirculating downdraft cell (shaded in grey in Figure 6.2b), surrounded by the annular updraft cell (shaded in red), reaches the

ground-plane and gives rise to the attached central stagnation point at $z = 0$. The downdraft cell contains air advected along the axis of rotation from aloft, has zero net axial mass flux, and its momentum and thermal energy are affected by the annular updraft cell flow. Similar to the single-cell vortex, the updraft cell contains boundary layer fluid convectively heated by the ground-plane as it passes through the azimuthal flow vanes, and confined to the annular domain $0.28 \leq r/R_i \leq 0.41$ surrounding the central downdraft cell. Its inner and outer bounds are marked by the streamlines "c" and "d", respectively. While the streamline "c" emanates from the separation line ($r/R_i = 0.16$), the streamline "d" is selected because it is asymptotically collinear with the contour $u(r, z) = 0$ ("e", marked in green) at the upper end of the domain past the contraction of the entrained boundary layer flow. It is remarkable that for the same *Gr* the cross stream extent of the surface layer, characterized by a wall-jet-like velocity distribution, is significantly different in the single-cell and the two-cell flow fields. While in the single-cell vortex the streamline "d" (Figure 6.2a) is approximately aligned with the maximum jet velocity (for $r/R_i > 0.2$), in the two-cell vortex, streamline "d" is located well *above* the maximum jet velocity, and the magnitudes of the velocity vectors above that streamline are noticeably smaller. The effects of these differences on the global entrainment to the vortex are discussed further in connection with Figure 6.4b to follow.

The radial entrainment into the two-cell vortex is effected by the changes in the pressure along the centerline and the radial pressure gradient within the vortex core and outer flow $\hat{C}_p = \partial C_p/\partial(r/R_i)$ [$C_p = (p - p_\infty)/0.5\rho\Omega^2R^2$]. The radial pressure gradient is computed using the radial Navier-Stokes equation (in cylindrical coordinates) and the measurements of the time-averaged three-dimensional flow field (cf. Figure 5.2). These

measurements are taken sufficiently high above the radial flow contraction domain ($z/h > 0.038$) that the flow is nominally self-similar (cf. Chapter 5), and the spatial SPIV grid resolution in the measurement plane at $z/h = 0.17$ is 3.2 mm. The radial pressure gradient for a single-cell vortex ($\varphi = 30^o$, Figure 6.3a), increases monotonically with r to a local maximum at $r/R_i = 0.11$ which is within and near the radial edge of the updraft cell ($r/R_i = 0.14$, Figure 6.2a), and decreases monotonically towards the edge of the measurement domain. The present measurements show that the magnitude of the local maximum of $\hat{C}_p$ for single-cell vortices increases monotonically with vane angle as the increase in angular momentum (cf. Figure 5.21a and b) augments the low pressure along the vortex centerline and leads to an increase in radial entrainment into the enclosure. However, the onset of the recirculating downdraft cell is accompanied by an increase in the pressure in the core, and, as a result, a significant decrease in the magnitude of the peak radial pressure gradient [e.g., $\hat{C}_{p\,50°} = 0.37\hat{C}_{p\,30°}$].

The nonhydrostatic axial pressure gradient, $\hat{p}_z = \partial(p)/\partial z = \rho[g - w(\partial w/\partial z)]$, along the vortex centerline ($u = 0$ at $r/R_i = 0$) is calculated (assuming axial symmetry) using the meridional SPIV measurements in the r-z plane for $\varphi = 30°$ and $50°$ ($Gr = 9.7{\cdot}10^7$) with resolution of $\Delta z/h = 1.5{\cdot}10^{-3}$. Above the development region of the core ($z/h > 0.038$), $\hat{p}_z$ is calculated using the axial variations of the weight deficiency ($\rho_\infty g' = \Delta\rho g$) and centerline axial velocity from the similarity of the vortex column. Assuming that the pressure at the central stagnation point ($r/R_i = z/h = 0$) is p_∞, the axial pressure gradient is integrated to estimate the axial variation of the pressure coefficient C_p along the centerlines of the single-cell ($\varphi = 30°$) and attached two-cell ($\varphi = 50°$) vortices (Figure 6.3b). Note that these axial distributions of C_p are each

normalized by Ω and R of the single cell vortex at $\varphi = 30°$ ($z/h = 0.17$), and that C_p computed from the similarity formulation is denoted by dashed lines. As expected, these data show that the pressure is highest at the central stagnation point on the surface, where the momentum boundary layer converges radially, and then diminishes with elevation to a local minimum at $z/h \approx 1.6 \cdot 10^{-2}$ and $2.4 \cdot 10^{-2}$ for the single and two-cell vortices, respectively (there is a small secondary minimum in the single-cell vortex near $z/h = 0.05$). The local pressure minimum of the two-cell vortex is considerably higher than in the single-cell vortex [$C_{p\,50°} = 0.42 C_{p\,30°}$], consistent with the lower radial pressure gradient (cf. Figure 6.3a) as the vortex core expands radially (cf. Figure 4.3b) in the presence of the reverse axial flow. The rapid decrease in pressure over this near-surface vertical domain is associated with axial updraft acceleration and downdraft deceleration along the centerlines of the single-cell and attached two-cell vortices, respectively. The pressure minimum of each vortex coincides with the elevation of its maximum tangential velocity, marking the turning of the buoyant boundary layer flow into the updraft cell (Figures 6.2a and b). Above these minima, the axial pressure increases monotonically, accompanied by a decrease in tangential velocity as the vortex core expands radially.

The effects of the vane array on the magnitude and direction of the entrained flow are quantified by considering v/u into the radial edge of the measurement domain and the axial volume flow rate Q out of this domain (Figures 6.4a and b, respectively). For each vane angle (with $Gr = 9.7 \cdot 10^7$), the velocity ratio is calculated at $z/h = 0.17$ and $r/R_i = 0.6$ while the corresponding volume flow rate ($Q = 2\pi \int_0^{0.6R_i} wrdr$) is computed at $z/h = 0.17$ for $r/R_i \leq 0.6$ and normalized by Q at $\varphi = 30°$ ($\widehat{Q} = Q/Q_{30°}$). These data show that v/u increases monotonically with $\tan\varphi$, with an abrupt increase in the rate of change

coinciding with onset of the detached downdraft cell ($\varphi \cong 35^{o}$, $\tan\varphi \cong 0.7$), thus indicating a significant increase in angular momentum relative to the radial momentum imparted to the entrained flow through the vanes. However, $\widehat{Q}$ has a local maximum before the onset of the downdraft (φ = 30°, $\tan\varphi$ = 0.58) and then monotonically decreases with increasing vane angle (Figure 6.4b, where the detached and attached two-cell vortices are indicated in red). The precipitous decrease in volume flow rate indicates that an increase in the radial pressure gradient that might be associated with the increase in the tangential velocity is strongly offset by an increase in the centerline pressure due to the presence of the cell open to flow from aloft. The abrupt increase (decrease) of v/u (Q) corresponding to the onset of downdraft reflects the alleviation of the radial pressure gradient force and, therefore, a reduction in the entrainment into the vane array. When comparing the volume flow rate through the single- and two cell vortices, it is noteworthy that the fraction of the volume flow rates through the updraft cells (i.e., originating from the ground-plane entrainment) of the single-cell (φ = 30°, Figure 6.2a) and attached two-cell (φ = 50°, Figure 6.2b) vortices are 18.9% and 49.9%, respectively, out of the entire volume flow rate through the vortex within this domain ($0 < r/R_i < 0.6$, $z/h = 0.17$). However, it is noted that the overall volume flow rate through the single-cell vortex at this height is 34% higher than that of the attached two-cell vortex (cf. Figure 6.4b). These changes in volume flow rate are indicative of the changes in global entrainment brought about by formation of the downdraft cell and alteration of the pressure field.

Another indication of the effects of downdraft is given by the integrated kinetic energy flux through the circular cross-section $r/R_i < 0.6$ at z/h = 0.17 (cf. Figures 5.22c and d) normalized by the integrated gravitational potential energy flux

$\hat{\dot{E}} = \dot{E}/(g\rho\nu R_i^2)$ (single-cell and two-cell (detached or attached) vortices are marked by black and red symbols, respectively in Figure 6.4c). These data show that for a single cell vortex ($\tan\varphi \leq 0.58$, $\varphi \leq 30°$) $\hat{\dot{E}} \sim (\tan\varphi)^{1/3}$ and increases by nearly three-fold between $\varphi = 5°$ and 30° (i.e., $\dot{E}_{30°} = 2.7\dot{E}_{5°}$). The appearance of the downdraft cell at the elevation of the measurement plane results in a monotonic decrease in $\hat{\dot{E}}$ with increasing φ ($0.7 \leq \tan\varphi \leq 1.43$), and as is evident in Figure 6.4c, the functional dependence of $\hat{\dot{E}}$ for the single-cell vortex over predicts the measured integrated kinetic energy flux. These data indicate that the increase in angular momentum of the flow field is more than offset by the decrease in radial entrainment and axial momentum, and further by the increase in R_i with $\tan\varphi$. However, as is evident from Figure 6.2b, the appearance of the downdraft cell also alters the scaling of the domain through which positive axial velocity flows. Despite the increase in enclosure radius R_i with φ, the annular domain of positive axial mass flux diminishes once downdraft extends along the centerline of the vortex column. In an *annular* updraft region defined as $R_u = R_i - R_d$, where R_i is the internal radius of the vane enclosure and R_d is the radius of the downdraft cell, the integral of the energy flux for the two-cell data also varies like $(\tan\varphi)^{1/3}$ (marked by light red symbols). Therefore, despite the increase of enclosure radius R_i with φ, the annular domain of net positive axial flow decreases as the downdraft cell migrates along the centerline of the vortex column.

The regulation of radial entrainment by the vanes does not alter the mechanisms for production and sustainment of axial vorticity within the vortex core. Since in a single-cell vortex, the radial circulation into the sides of a cylindrical control volume bounded circumferentially by the vane array and below by the ground-plane is identical

to the axial circulation of the top surface (cf. Figure 5.17), all axial vorticity within the columnar vortex originates from radial vorticity generation within the boundary layer. Therefore, the same should hold for a two-cell vortex, assuming that the downdraft only transports irrotational flow from aloft. Measurements of the three components of the time-averaged flow in the meridional (r-z) plane of an attached two-cell vortex ($0 < r/R_i < 0.6$ and $0 < z/h < 0.1$) at $\varphi = 50°$ and $Gr = 9.7 \cdot 10^7$ yield axisymmetric distributions of the three vorticity components $(\omega_r, \omega_\theta, \omega_z)$. The normalized vorticity distributions $(\widehat{\omega}_r, \widehat{\omega}_\theta, \widehat{\omega}_z)$ are shown in Figures 6.5a-c (for comparison single-cell concentrations are included Figure 5.14) using color raster plots overlaid with velocity vectors which also include the critical points and the projected stream surfaces marking the interfaces between the updraft and recirculating downdraft cells and between the updraft cell and the outer flow (vorticity concentrations are normalized by the angular velocity of a single-cell vortex $\Omega = 15$ s^{-1} at $\varphi = 30°$, $z/h = 0.17$). The radial vorticity component $\widehat{\omega}_r$ (Figure 6.5a) within the boundary layer results from axial shear by the clockwise swirling flow above. Since the flow rotation about the vortex axis does not change direction within the downdraft cell (cf. Figure 4.3b), neither does $\widehat{\omega}_r$ (positive on both sides of the separation line) until it ultimately vanishes near $r = 0$ due to being tilted and stretched axially by the buoyantly accelerating flow. Outside of the viscous boundary layer, there is a small concentration of negative radial vorticity near the interface between the two cells due to the rapid radial expansion of the vortex core after the vortex contraction. The raster plot of azimuthal vorticity concentrations (Figure 6.5b) show that for $r/R_i > 0.4$ the azimuthal vorticity is primarily confined to the boundary layer over the ground-plane and intensifies with decreasing radial distance until the radial

velocity diminishes (and ultimately vanishes) at the separation line. The vertical turning of the downdraft and updraft flows that leads to the formation of a vertically spiraling jet (cf. Figure 6.1a) induces both positive and negative concentrations of ω_θ above the wall layer with a local extrema at $(r/R_i,\ z/h) = (0.22,\ 0.02)$ and $(0.17,\ 0.05)$, respectively. Distributions of the axial vorticity ω_z (Figure 6.5c) show that it is primarily concentrated within a cylindrical domain that extends radially with elevation and is ultimately bounded from the outside by the interface between the updraft cell and the outer flow (e.g., at $r/R_i = 0.41,\ z/h = 0.10$). The axial vorticity ω_z peaks within an annular domain surrounding the recirculating downdraft cell (cf. Figure 4.4c), and its largest magnitude is at the elevation of the maximum tangential velocity ($r/R_i = 0.27,\ z/h = 1.8 \cdot 10^{-2}$), at the vortex contraction just above the critical point marking the intersection of the two-cell interface with the ground-plane.

It is instructive to consider the evolution of the vorticity field within the core of the vortex. Vortex lines originating within the lower half of the viscous boundary layer spiral (CW) radially inwards and are tilted into the axial direction to form helical (θ, z) spirals about the z-axis (cf. Figure 5.15). The axial progression of the downdraft cell from aloft forces these vortex lines to spread radially, and decreases their vertical pitch as axial vorticity is tilted radially and azimuthally by axial gradients in their respective velocity components due to the radial spreading of the vortex core. Azimuthal shear applied on the downdraft cell by the surrounding updraft cell enables the diffusion of axial vorticity radially into the recirculating cell. Azimuthal vorticity concentrations on either side of the jet-like axial flow (cf. Figure 6.5b) affect radial gradients of axial velocity. The negative azimuthal vorticity inside the downdraft cell is continuously

augmented by azimuthal tilting of axial vorticity and results in progressively larger magnitude concentrations of negative azimuthal vorticity with elevation. Therefore, the radial spreading of the columnar vortex, which induces a positive (nonhydrostatic) axial pressure gradient, is also responsible for additional tilting of axial vorticity into the azimuthal vorticity within the countercurrent helical shear layer between the up- and downward flows within the recirculating downdraft cell.

The variation with $\tan\varphi$ ($5° \leq \varphi \leq 55°$, 5° increments, $z/h = 0.17$ and $Gr = 9.7 \cdot 10^7$) of two integral scales associated with the vorticity field discussed above are considered: the core Reynolds number based on the axial circulation $Re = \Gamma_z/(2\pi\nu)$ and the vortical hydrodynamic impulse per unit length and unit density (using the Boussinesq approximation) $\vec{I} = \iint \vec{x} \times \vec{\omega} dS$ (Figures 6.6a and b, respectively). The data in Figure 6.6a demonstrate that axial circulation increases like $(\tan\varphi)^{3/4}$ regardless of the cellular structure of the vortex core (cf. Figure 5.22a). The decrease in the magnitude of the axial vorticity which accompanies the downward axial migration of the recirculating cell is compensated for by a widening of its radial distribution (cf. Figure 4.4). This redistribution is quantified using the vortical hydrodynamic impulse $\vec{I} = \iint \vec{x} \times \vec{\omega} dS$ which measures the first moment of vorticity and can be thought of as analogous to the momentum required to engender an identical vortex of a given strength (Lamb 1945; Saffman 1992). The azimuthal and axial components of the vortical impulse per unit length (normalized by $2\pi\nu R_i$), defined by $I_\theta = -2\pi \int_0^R \omega_z r^2 dr$ and $I_z = 2\pi \int_0^R \omega_\theta r^2 dr$, in the r-θ plane are shown in Figure 6.6b. For a single-cell vortex (i.e., $\tan\varphi \leq 0.58$), the two components of the impulse increase monotonically with the induced angle and are nearly identical, indicating that the contributions from the azimuthal and axial vorticity

concentrations are nearly the same. The increase in azimuthal impulse for the single-cell vortex results from the simultaneous increases in axial circulation (cf. Figure 5.22a) and core radius (cf. Figure 5.21a) with φ ($\hat{I}_{\theta,30^\circ} = 2.1\hat{I}_{\theta,5^\circ}$). The increase of the axial impulse I_z ($\hat{I}_{z,30^\circ} = 1.7\hat{I}_{z,5^\circ}$) is associated with the increase in volume flow rate through the updraft cell with φ (cf. Figure 6.4b) and the resulting intensification of the positive azimuthal vorticity within the shear layer between the radial edge of the buoyancy-driven core and outer flow. In the presence of the downdraft cell, as the distribution of axial vorticity spreads laterally and concentrations migrate to the distal edge of the core (at a fixed elevation $z/h = 0.17$), the rate of change of $\hat{I}_\theta$ increases and is indicative of the increase in angular momentum of the two-cell vortex. However, the intensification of negative azimuthal vorticity within the recirculating downdraft cell and reduction in the magnitude of the positive azimuthal vorticity between the core and outer flow as a result of the reduction in Q for two-cell vortices (cf. Figure 6.4b) leads to a monotonic decay in $\hat{I}_z$ for $\tan\varphi > 0.7$. In fact, at the largest vane angle tested ($\varphi = 55°$), $\hat{I}_z$ is negative, and negative axial momentum would be needed to form an identical attached two-cell vortex.

As discussed in Chapter 5, within the similarity domain of the single-cell vortex the local swirl $S(\eta)$ and Froude numbers $Fr(\eta)$ are invariant with Gr for a given vane angle, and both $S(\eta)$ and $Fr(\eta)$ increase with φ. The dependence of $S(\eta)$ and $Fr(\eta)$ on the formation parameters of attached two-cell ($\varphi = 50°$) and single-cell ($\varphi = 30°$) vortices are compared over a range of Grashof numbers [$Gr = 4.8 \cdot 10^7$ (50°C), $7.8 \cdot 10^7$ (75°C), $9.7 \cdot 10^7$ (100°C), $10.9 \cdot 10^7$ (125°C), and $11.6 \cdot 10^7$ (150°C)] in Figures 6.7a and b ($z/h = 0.17$). Similar to Figure 5.23, for a given vane angle these data are invariant with Gr, demonstrating that the strength of the attached downdraft cell is proportional to the

magnitude of the thermal forcing (note that due to the expansion of the vortex core with downdraft [cf. Figure 4.3b], the radial extent of the measurement domain in the similarity coordinate η is significantly smaller). However, the radial distributions and magnitudes of S and Fr are clearly altered by the presence of downdraft. The swirl number of the two-cell vortex (Figure 6.7a) exhibits an apparent singularity at $\eta = 0.33$ between the downward and upward axial flows in the recirculating downdraft cell where $w \rightarrow 0$. For $\eta > 0.33$, S of the attached two-cell vortex is larger than that of the single-cell (S = 6.2 and 2.9 at η = 1, respectively) due to the diminished axial velocity throughout the enclosure with the onset of reversed axial flow (cf. Figure 4.3a). For $\varphi = 50°$, the local swirl number reaches a minimum (S = 4.7) near the location of streamline "c" in Figure 6.2a and monotonically increases through the updraft cell ($0.84 \leq \eta \leq 1.24$, $0.28 \leq r/R_i \leq 0.41$) and outer flow. Analogously, the adjusted Froude number (Figure 6.7b), which is smaller in the two-cell vortex owing to the decrease in axial momentum and increase in thermal energy (cf. Figure 4.3b and c), vanishes at the interface between the downward and upward axial flows. For $\eta > 0.33$, Fr has a local maximum at $\eta = 0.84$ (r/R_i = 0.28) near the location of streamline "c" in Figure 6.2a along the midpoint of the helical jet formed by the merging of the updraft cell and upward motions of the recirculating downdraft cell. For $\eta > 0.84$ ($r/R_i > 0.28$), Fr diminishes as a result of the decreasing axial velocity and advection of thermal energy from the heated air layers into the updraft cell.

When radial distributions of the time- and azimuthally-averaged tangential and axial velocity components and the weight deficiency of the two-cell attached vortex ($\varphi = 50°$) are each normalized by their respective maxima [$v(\eta = 1)$, $w(\eta = 0.8)$, and

$g'(\eta = 0.4)$], each distribution collapses to form a single, self-similar distribution with elevation and the primary formation parameters as shown in Figures 6.8a through c [for z/h = 0.08, 0.17, 0.25, 0.33, and 0.42 at $Gr = 9.7 \cdot 10^7$, and for $Gr = 4.8 \cdot 10^7$, $7.8 \cdot 10^7$, $9.7 \cdot 10^7$, $10.9 \cdot 10^7$, and $11.6 \cdot 10^7$ at z/h = 0.17]. It is remarkable that self-similarity is attained the global length scale imposed by the azimuthal array and the drastic structural changes caused by the recirculting downdraft cell along the vortex axis. Of particular note is that although the temperature difference controls the elevation of the free stagnation point for the detached two-cell vortex (cf. Figure 4.2b), once a stable attached recirculating domain is established, the evolution of the vortex becomes self-similar with respect to Gr. The collapse of these data indicates that the balance between the buoyancy force and (downward) pressure force can be invariant despite the presence of reversed axial flow within the core. The corresponding radial distributions in similarity coordinates for the attached two-cell and single-cell vortices are compared in Figures 6.8d through f. Clearly, similarity is not maintained over the different vortex structures. While the radial peaks of the tangential velocity component obviously coincide at η = 1, the peak of the axial velocity in the two-cell vortex no longer occurs near $\eta \approx 1$, but rather at $\eta = 0.8$ near the location of streamline "c" in Figure 6.2b. As discussed in connection with Figure 4.3c, the location of peak temperature moves radially outward due to advection of cool air from aloft along the centerline. Therefore, weight deficiency has a maximum at $\eta = 0.4$ in the attached two-cell vortex, compared to $\eta = 0$ in the single-cell vortex. It is reasonable to assume that in the case of the detatched two-cell vortex, the self-similar distributions of a two- or single-cell vortex would also

describe the flow field above and below the free stagnation point, respectively, with similarity being disrupted near the free stagnation point.

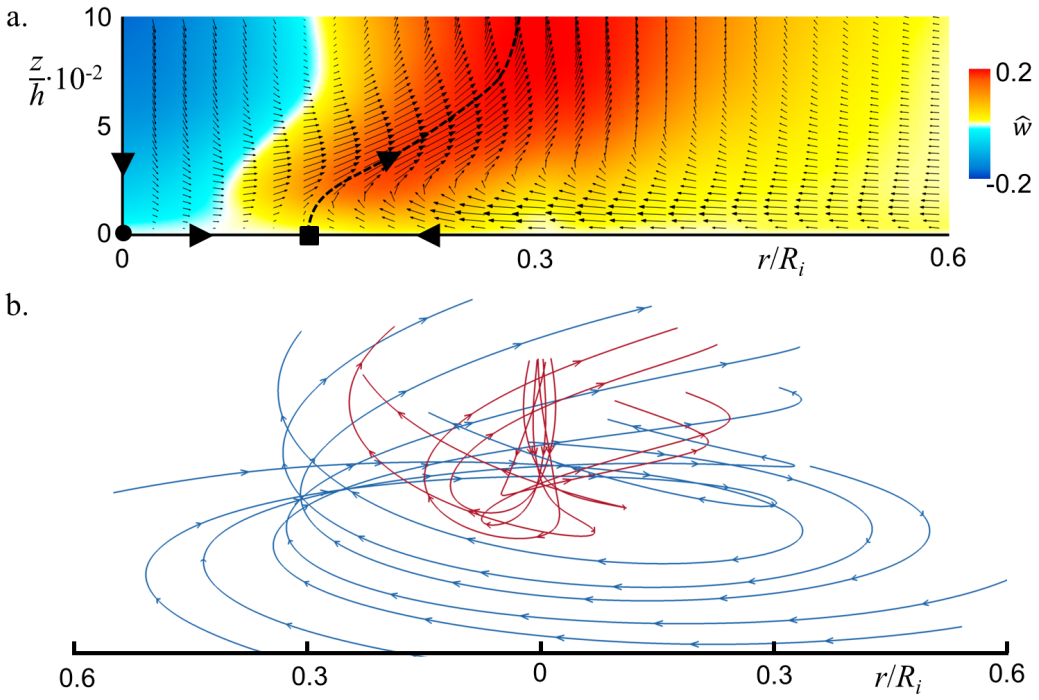

FIGURE 6.1. (*a*) Color raster plot of normalized axial velocity in the *r*-*z* plane overlaid with vertical distributions of the in-plane velocity vectors. The central stagnation point and separation line are marked by (●) and (■), and the projected stream surface that separates between the up- and downdraft cells is marked by a dashed line. (*b*) 3-D pathlines in the axisymmetric flow field showing the near-surface flow (blue) surrounding the recirculating downdraft (red) of a two-cell columnar vortex ($Gr = 9.7\cdot 10^7$, $\varphi = 50°$).

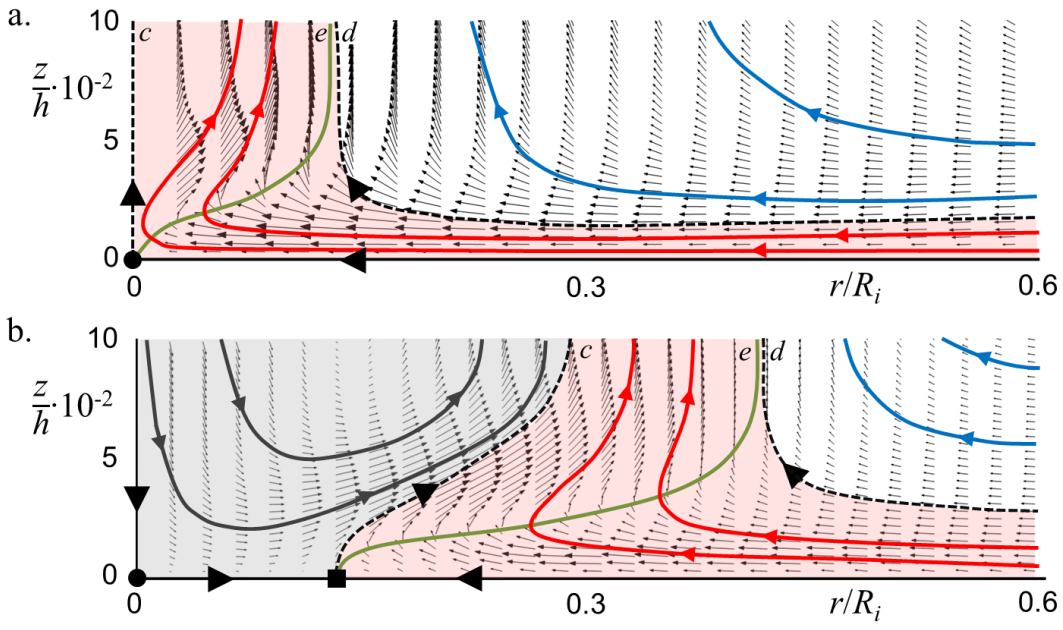

FIGURE 6.2. Vertical distributions of the in-plane velocity vectors in the *r*-*z* plane overlaid with projections of the intercepting stream surfaces for a (*a*) single- [$\varphi = 30°$] and (*b*) two-cell [$\varphi = 50°$] vortex structure ($Gr = 9.7\cdot 10^7$). The updraft cell is highlighted in red and the recirculating downdraft cell in gray. Projected streamlines in the recirculating downdraft cell, updraft cell, and outer flow are denoted in black, red, and blue, respectively. The characteristic streamlines (*c*,*d*) that define these interfaces are shown with dashed lines. Solid green line denotes the line of zero radial velocity (*e*).

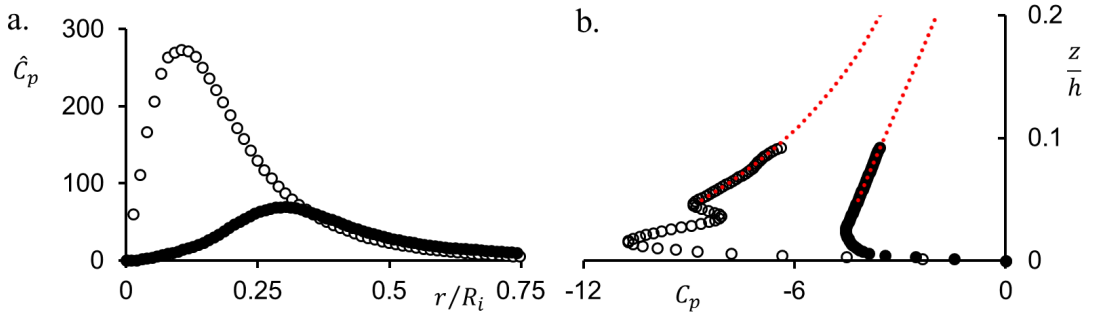

Figure 6.3. (*a*) Radial distribution of the radial pressure gradient of a single- (○) and attached (●) two-cell vortex at $z/h = 0.17$. (*b*) Axial variation of centerline pressure in a single- (○) and two- (●) cell vortex ($Gr = 9.7 \cdot 10^7$).

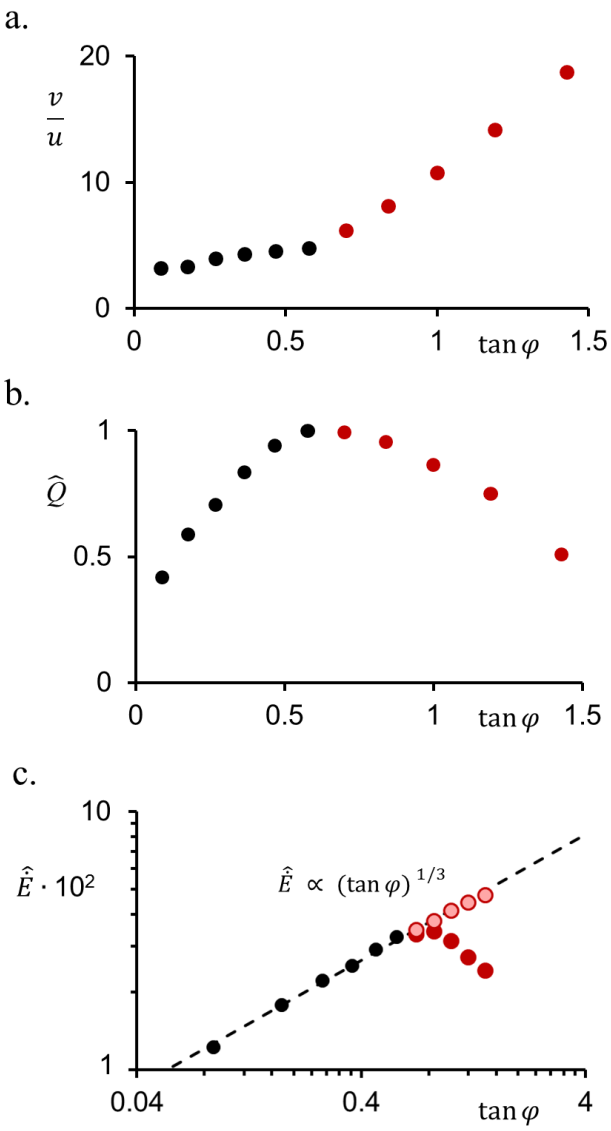

Figure 6.4. Variation of (a) v/u, (b) axial volume flow rate, and (c) integrated kinetic energy flux with $\tan\varphi$ (z/h = 0.17, $Gr = 9.7 \cdot 10^7$). Two-cell vortices are denoted in red.

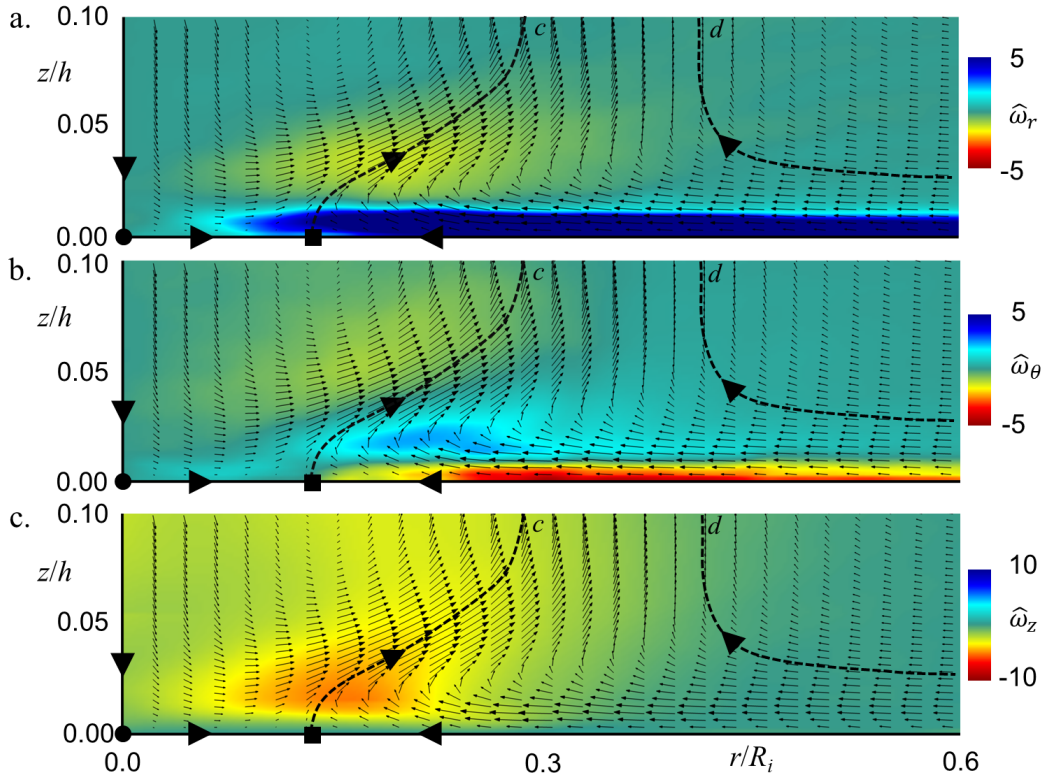

FIGURE 6.5. Color raster plots of normalized vorticity concentrations for an attached two-cell ($\varphi = 50°$) columnar vortex in the *r*-*z* plane: (*a*) radial, (*b*) azimuthal, and (*c*) axial concentrations overlaid with in-plane velocity vectors. The stagnation point, separation line, and flow interface are denoted by ●, ■ and --, respectively. ($Gr = 9.7 \cdot 10^7$).

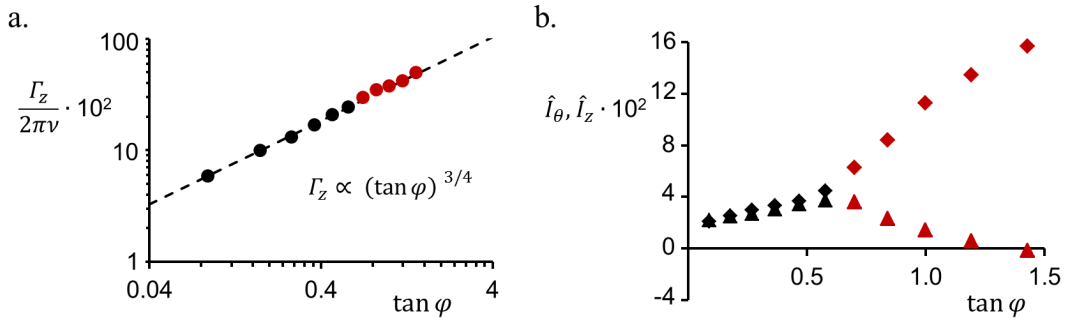

FIGURE 6.6. Variation of (*a*) core Reynolds number (●) and (*b*) azimuthal (♦) and axial (▲) impulse per unit length with tanφ (z/h = 0.17, Gr = 9.7·10^7). Two-cell vortex structures are denoted with red symbols.

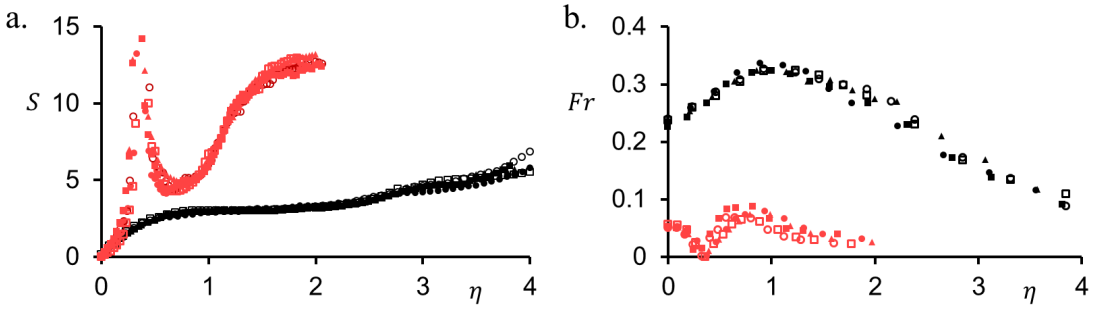

FIGURE 6.7. Radial distributions of local (*a*) swirl and (*b*) Froude numbers at Gr = 4.8 (■), 7.8 (▲), 9.7 (●), 10.9 (□), and $11.6 \cdot 10^7$ (○) for a single- [φ = 30°, black] and attached two-cell [50°, red] vortex.

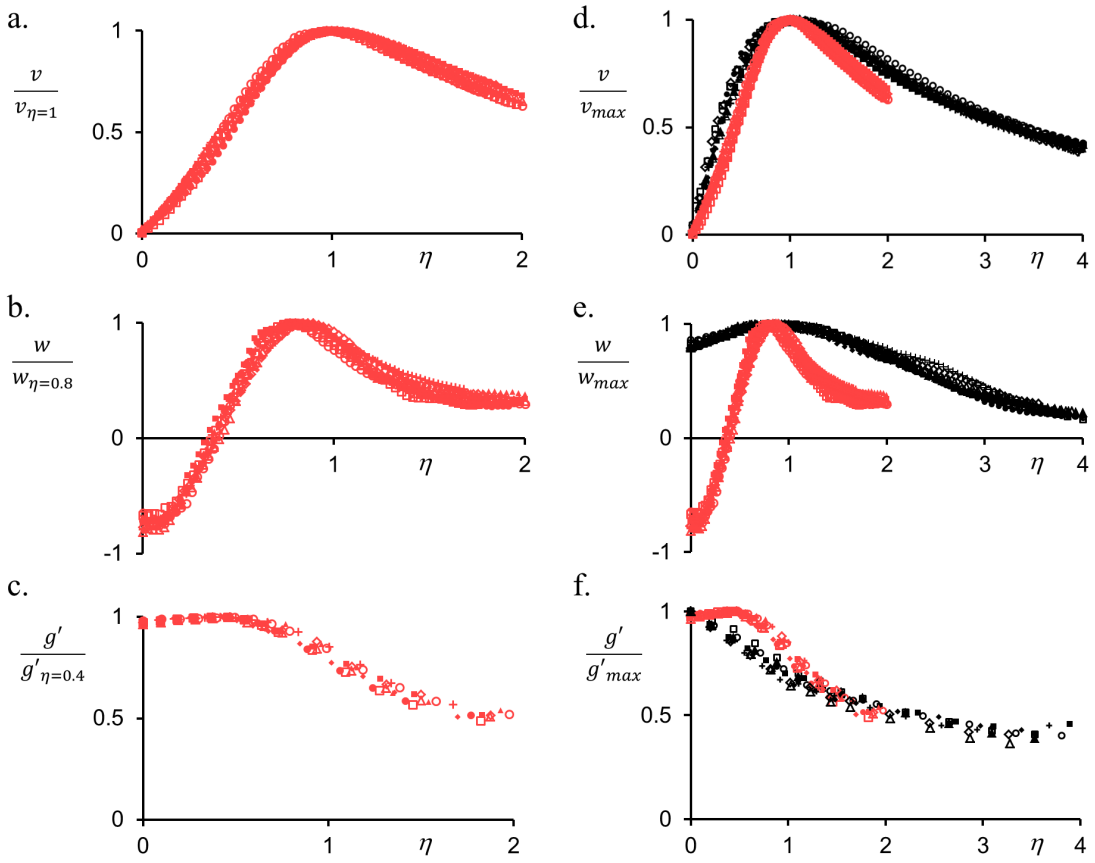

FIGURE 6.8. Radial distributions of the time- and azimuthally-averaged (*a,d*) tangential velocity, (*b,e*) axial velocity, and (*c,f*) weight deficiency of single- (black) and attached two-cell (red) vortices at $z/h = 0.17$ for $\varphi = 50°$ at $Gr = 4.8$ (■), 7.8 (▲), 9.7 (●), 10.9 (□), and $11.6 \cdot 10^7$ (○) and $Gr = 9.7 \cdot 10^7$ at $\varphi = 50°$ for $z/h = 0.08$ (♦), 0.17 (●), 0.25(Δ), 0.33 (◊), and 0.42 (+).

Chapter VII

MODIFICATION OF COLUMNAR VORTICES BY GROUND-PLANE VORTICITY MANIPULATION

Chapters 5 and 6 discussed the effects of the primary generation parameters (namely, the Grashof number and the magnitude and direction of the entrained flow) on the formation and evolution of single- and two-cell buoyant columnar vortices. In these investigations, the boundary layer on the heated ground-plane and, in particular, the development of the vorticity flux into the vortex core, is affected by the boundaries of the flow enclosure. The present chapter discusses the effects of altering the vorticity distribution and transport within the ground-plane boundary layer on the structure of the columnar vortex. While the generation and advection of vorticity concentrations in and above the spiraling boundary layer of the base flow within the flow enclosure can be manipulated in a number of ways, the present investigations explore the effects of an array of vertical (lower-tier) flat-plate vanes that alter the direction of the boundary layer flow towards the central vortex. These vanes, which are azimuthally distributed about the outer perimeter of the enclosure and extend a short distance above the boundary layer are mounted below and can be independently adjusted relative to the upper-tier vanes, as shown schematically in Figure 3.3b. The lower-tier vanes redirect the entrained flow along the surface, affect a local horizontal swirl number v/u, and effectively shorten the spiraling trajectory of the entrained flow into the vortex core, thereby alleviating the streamwise pressure drop through the vanes. The measurements presented in this chapter

are acquired using the 3.7 m scale laboratory facility (cf. Figure 3.2). The effects of the lower-tier vanes on the structure of the columnar vortex are examined in §7.1, and the structure and advection of vorticity concentrations affected by these vanes are discussed in §7.2. Finally, control over the magnitude and distribution of these vorticity concentrations through changes to the lower-tier geometry is demonstrated in §7.3.

7.1 Alteration of the Columnar Vortex

The effects of the lower-tier vanes are investigated in the presence of an attached two-cell vortex (cf. Chapter 4) that is formed at a vane angle of $\varphi = 50°$ (at this setting the radius of the cylindrical vortex enclosure is $R_i = 0.6$ m) and $Gr = 43 \cdot 10^8$ ($L_p = 3.7$ m; cf. Figure 3.2a). The twelve flat-plate lower-tier vanes in the present investigations are normal to the ground-plane and extend $0.133h$ above the heated surface (cf. Figure 3.3b). Each vane ($l_h = 0.79h$) extends $0.76h$ into the vortex enclosure from the same pivot point as the corresponding upper-tier vane above it. When the lower-tier vanes are set at $\varphi_h = 15°$ with respect to the inward radial direction, they form an internal cylindrical enclosure with radius $R_h = 0.25R_i$. The corresponding settings of the upper-tier vanes are $\varphi = 50°$ and $R_i = 60$ cm ($l = 0.56h$).

Time- and azimuthally-averaged radial distributions of the tangential and axial velocity components are measured using SPIV in the horizontal plane at $z/h = 0.83$ ($z/h_h = 6.25$) above the heated ground-plane and are shown in Figures 7.1a and b along with the corresponding distributions for the baseline vortex. Each velocity component is normalized by the angular velocity Ω (3.25 s^{-1}) and core radius R (24.5 cm) of the corresponding columnar vortex in the baseline enclosure. The distribution of the normalized tangential velocity $\hat{v}_h$ in the presence of the lower-tier vanes is significantly

different from the Lamb-Oseen-like distribution in the baseline configuration (subscripts h and b refer to hybrid and baseline vanes). The hybrid vortex has solid-body rotation about its centerline, with a local maximum at r/R_i = 0.09, followed by a monotonic decrease to a local minimum at r/R_i = 0.24. There is a secondary annular domain of solid-body rotation ($0.3 < r/R_i < 0.47$) with a local maximum at $r/R_i = 0.55$. Following the second maximum, $\hat{v}_h$ decreases again and $\hat{v}_h \approx \hat{v}_b$ throughout the remainder of the measurement domain ($r/R_i > 0.55$). The radial distribution of the axial velocity in the hybrid vortex $\hat{w}_h$ (Figure 7.1b) is also significantly altered compared to the baseline vortex. Perhaps the most salient feature is the absence of the recirculating downdraft cell and the significant increase in the magnitude of $\hat{w}_h$ compared to $\hat{w}_b$ within $r/R_i < 0.4$, where $\hat{w}_{h\text{-max}} = 2.65\hat{w}_{b\text{-max}}$. However, within the range $0.25 < r/R_i < 0.75$ the radial rate of decrease of $\hat{w}_h$ is higher than that of $\hat{w}_b$, and for $r/R_i > 0.5$, $\hat{w}_h < \hat{w}_b$ (at $r/R_i = 0.75$, $\hat{w}_h = 0.14\hat{w}_{h\text{-max}}$). The radial distribution of $\hat{w}_h$ indicates that changes in the entrained flow through the lower-tier vanes lead to the detachment of the downdraft cell of the baseline vortex and to an upward migration of the free stagnation point along the axis of rotation (cf. Chapter 4). This is the result of a significant increase in entrainment through the vane array (integral of the volume flow rate based on the radial distributions of the axial velocity, $Q_h = 1.6Q_b$) that eliminates entrainment of makeup air from aloft. The detachment is accompanied by a strong buoyancy-driven updraft that overcomes the rotation-induced, low pressure along the centerline and the resulting adverse axial pressure gradient. In fact, there is a minor slowdown of the flow at $r = 0$, manifested by a slight local minimum of $\hat{w}_h$ on the centerline and a shallow local maximum at $r/R_i = 0.12$. Unlike the single-cell columnar vortex (Chapter 5), the radial location of $\hat{w}_{h\text{-}}$

$_{max}$ does not correspond to the first maximum of the tangential velocity (r/R_i = 0.09). Instead, there is an annular domain 0.09 < r/R_i < 0.24 of higher axial velocity within the outer flow, in which $\hat{v}_h$ has a local minimum. However, the redistribution of momentum comes at the cost of an axial momentum deficit compared to the baseline within the outer radial extent of the enclosure (r/R_i > 0.55).

Radial distributions of the normalized temperature $\hat{T} = (T\text{-}T_\infty)/(T_p\text{-}T_\infty)$ within the flow are measured at z/h = 0.83 using a radial rake of thermocouple sensors spaced 1 cm apart (≈ 0.017R_i) for the baseline and hybrid geometries are shown in Figure 7.1c. The temperature distribution in the baseline (attached two-cell) vortex has an off-center local maximum $\hat{T}_{b\text{-max}}$ = 0.26 at r/R_i = 0.17 as a result of the advection of cool air from aloft by the reversed axial flow (cf. Figure 4.3c). Past this peak, the air temperature decreases radially in the domain 0.17 < r/R_i < 0.65 before reaching a nearly-constant level $\hat{T}$ = 0.11 at r/R_i = 0.65. By comparison, the temperature distribution of the hybrid vortex is similar to that of a single-cell vortex (cf. Figure 4.3c) for which the maximum $\hat{T}_h$ = 0.28 occurs on the centerline, with $\hat{T}$ decreasing radially to nearly the same temperature ($\hat{T}$ = 0.11) as for the baseline vortex (r/R_i > 0.48). The radial distribution of normalized temperature in the annular domain 0.65 < r/R_i < 1 is identical for both configurations. These data show that the secondary peak of the tangential velocity and the elevated axial velocity do not significantly alter the radial temperature distribution within the outer flow. In fact, even though the baseline vortex encounters downdraft of cooler air along its axis, it has a larger radially-integrated enthalpy ($\mathcal{H} = 2\pi\int \rho c_p \Delta T r dr$; cf. Figures 4.2d and e) than the hybrid vortex, $\mathcal{H}_b$ = 1.2$\mathcal{H}_h$. The radial integral of the kinetic energy flux through a radially expanding circular control surface centered about the axis of rotation at the same

elevation is computed from the SPIV data, and the normalized radial distributions [($\hat{\dot{E}} = \dot{E}/(\rho g \upsilon R_i^2)$] for the baseline and hybrid vortices are shown in Figure 7.1d. These data show that for the same *Gr* ($43 \cdot 10^8$), the hybrid vane configuration induces a 2.5-fold increase ($\dot{E}_h = 2.51\dot{E}_b$) in the available mechanical power within the measurement domain.

The radial entrainment into the vane enclosure is affected by the changes in the radial pressure gradient $\hat{C}_p = \partial C_p/\partial(r/R_i)$ [$C_p = (p - p_\infty)/(0.5\rho\Omega^2R^2)$] within the flow enclosure. The SPIV measurements of the time-averaged three-dimensional flow within the enclosure (8 mm grid) are used to estimate $\hat{C}_p$ from the radial Navier-Stokes equation (cf. Figure 5.2) at $z/h = 0.83$. The radial pressure gradient of the baseline vortex (cf. Figure 6.3a), increases monotonically with r to a local maximum at $r/R_i = 0.32$, just radially inward of the radial peak of tangential velocity (cf. Figure 7.1a) and thereafter decreases monotonically towards the edge of the measurement domain (Figure 7.2). The magnitude of the pressure gradient within the central column of the hybrid vortex is significantly higher and has a local maximum at $r/R_i = 0.04$, $\hat{C}_{p\,h\text{-max}} = 6.2\hat{C}_{p\,b\text{-max}}$. These data suggest that the redirection of the spiraling flow within the surface boundary layer can lead to significant enhancement of the ensuing vortex flow, and thereby augment the induced radial pressure gradient at higher elevations which is manifested by the substantial increase in radial entrainment into the enclosure.

The hybrid vane configuration also leads to a redistribution of the axial vorticity ω_z. Figures 7.3a and b show color raster plots of the time-averaged axial vorticity overlaid with tangential velocity vectors in the plane $z/h = 0.83$ for the baseline and hybrid vortices, respectively. In the baseline two-cell vortex, the axial vorticity within

the circular domain ($r/R_i < 0.2$) coinciding with the recirculating downdraft cell of the vortex core (i.e., $\hat{w} < 0$) is nearly invariant (approximately $0.5\omega_{z\text{-max}}$). This inner domain is surrounded by an annular domain about the axis of rotation ($0.1 < r/R_i < 0.3$) where $\omega_z > 0.7\omega_{z\text{-max}}$. Outside the vortex core ($r/R_i > 0.4$), the axial vorticity vanishes and the time-averaged flow field is nearly irrotational.

The corresponding concentrations of axial vorticity within the hybrid vortex (Figure 7.3b) are significantly different. The axial vorticity is concentrated within a central, high-intensity core ($r/R_i < 0.12$) that is surrounded by an annular domain in which ω_z nearly vanishes ($0.12 < r/R_i < 0.23$). The secondary radial increase and peak of the tangential velocity (cf. Figure 7.1a) is accompanied by a secondary annular ($0.3 < r/R_i < 0.47$) concentration of lower magnitude ω_z [$\hat{\omega}_z(r/R_i = 0) \approx 10\hat{\omega}_z(r/R_i = 0.4)$]. Outside this second annular concentration, the axial vorticity vanishes. The formation of these two distinct vorticity concentrations marks a significant extension of the formation of axial vorticity within single- and two-cell vortices in which the flow along the ground-plane is unaltered (Chapters 5 and 6). These data indicate that the lower-tier vanes lead to intensification of the radial vorticity within the segmented surface boundary layer and augment its axial tilting outside of the primary core of the columnar vortex. The axial vorticity in Figures 7.3a and b is used to compute radial distributions of the core Reynolds number $Re = \Gamma_z/(2\pi\nu)$ in Figure 7.3c. The circulation of the baseline vortex increases monotonically with r, and is nominally invariant ($Re = 14600$) at $r/R_i = 0.5$. The radial rate of increase of Re of the hybrid vortex diminishes significantly within $0.12 < r/R_i < 0.23$ outside of the vortex core, and then increases again at nearly its initial rate within the annular vorticity domain, before reaching the same

asymptotic level of the baseline vortex (Re = 14600) at r/R_i = 0.62. This shows that despite the changes in the geometry of the vanes, the net axial circulation is invariant. Furthermore, this finding indicates that for a given Gr the core Reynolds number in the presence of the hybrid vanes is determined by the geometry of the upper-tier vanes.

7.2. Structure and Advection of Secondary Vortices

The changes in columnar vorticity concentrations brought about by the presence of the lower-tier vanes through disruption of the swirling momentum boundary layer are highlighted in smoke visualization of the flow through and above these vanes. Figure 7.4a shows a snapshot of a longitudinal vortex formed by interaction between the radially entrained flow through the lower-tier vanes and the tangentially (CW as viewed from above) rotating outer flow above them (denoted by the blue CW arrow). This vortex forms within the converging channel between adjacent lower-tier vanes (shown schematically in a top view in Figure 7.4b, which also includes a notional depiction of the entrained air flow through the upper and lower-tier vanes). The longitudinal vortex between the lower-tier vanes is induced by a shear layer between these two air streams, lifts vertically from the surface as the lower-tier vanes contract, and is ultimately advected up into the bulk rotating flow just upstream of the radial edges of the vanes. Once the longitudinal vortices formed within each of the lower-tier vane channels are subjected to the rotating flow above, they become helically wound about the primary vortex column. The continuous creation and advection of these secondary vortices results in the redistribution of the axial vorticity and the formation of the time-averaged annular domain $0.3 < r/R_i < 0.47$ in Figure 7.3b.

Measurements of the near-surface flow within the converging channel formed by adjacent lower-tier vanes are acquired using SPIV in several planes, each normal to the ground-plane and a channel wall. In the present configuration, the measurement planes are normal to the inner surface of the left vane in Figure 7.5e, which is at an angle $\varphi_h = 15°$. In the present data, the field of view in each measurement plane extends to the height of the vane ($z/h_h = 1$), and data are acquired at six stations along the channel, $0.14l_h$ (10 cm) apart, starting $0.21l_h$ (15 cm) upstream of the downstream vertical edge of the left vane at $r/R_i \approx 1.18$. As shown in Figure 7.5*e*, the flow within the channel is described using a secondary coordinate frame rotated about the z axis ($\breve{x}$, $\breve{y}$, z), where the $\breve{x}$ and $\breve{y}$ axes are normal and parallel to the surface of the left vane, with the corresponding velocity components given by $v_{\breve{x}}$, $v_{\breve{y}}$, and w. Figures 7.5a-d show color raster plots of the normalized in-plane velocity magnitude $\left|\hat{V}_{\breve{x}-z}\right| = V_{\breve{x}-z}/V_{max}$ (V_{max} is the maximum in-plane velocity in each plane), overlaid with velocity vectors at four streamwise positions $\breve{y}/l_h = 0.21$, 0.35, 0.49, and 0.63. Note that each measurement plane is offset by $\Delta\breve{x}/h_h \approx 0.08$ relative the left and right vanes to avoid laser reflections, and that the intervene gap and field of view diminish in the streamwise direction with increasing $\breve{y}$. Upstream of the first measurement plane $0 < \breve{y}/l_h < 0.21$, vertical air layers with different velocities are tangentially and radially entrained between adjacent upper- and lower-tier vanes, and interact to form a shear layer at the interface between them, as depicted notionally in Figure 7.4b. The flow to the left and above the channel in Figure 7.5*e* (i.e., CW in a top view of the enclosure and denoted by the blue arrows) results in the streamwise helical flow within the channel.

The measurement plane farthest upstream (at $\breve{y}/l_h = 0.21$) is at the same location which an upper-tier vane crosses the edge of the left lower-tier vanes. Figure 7.5a shows the CCW flow within the vane channel and the onset of helical rotation in this plane. Of particular note is the downward flow along the surface near $\breve{x}/h_h = 0$ as outer flow air is advected downward to induce recirculation within the channel. Negligible in-plane motion exists at the center of the measurement domain, and rotation is confined to the edges of the channel, signifying the onset of the longitudinal vortex. At the next measurement station, $\breve{y}/l_h = 0.35$, the in-plane rotational motion is more coherent, and is accentuated by the presence of a low-velocity domain centered at $\breve{x}/h_h = 0.5$, $z/h_h = 0.75$. As the adjacent vanes contract and the longitudinal vortex is advected in the streamwise direction, the vortex tightens and begins to lift from the surface (this lifting is ostensibly forced by the image vortices of the bottom and vertical vane on the right). At $\breve{y}/l_h = 0.49$, the upper segment of the longitudinal vortex is above the measurement domain ($z/h_h > 1$) and its effect on the flow within the channel is confined to the spanwise region $0 < \breve{x}/h_h < 0.5$. The downwash on the left (outside the field of view) is diminished, and the largest in-plane velocity is the upwash near at $\breve{x}/h_h \approx 0.75$. By $\breve{y}/l_h = 0.63$ (Figure 7.5d), the longitudinal vortex has been completely advected out of the channel, and the remaining in-plane motion is vertical advection of buoyant near-surface air.

The streamwise evolution of the longitudinal vortex along the channel between the lower-tier vanes is further investigated by considering the changes in volume flow rate [$\iint v_{\breve{y}} d\breve{x} dz$], integrated kinetic energy flux [$\iint v_{\breve{y}}(v_{\breve{x}}{}^2 + v_{\breve{y}}{}^2 + w^2) d\breve{x} dz$], and integrated streamwise vorticity flux [$\iint v_{\breve{y}} \omega_{\breve{y}} d\breve{x} dz$] (subject to the Boussinesq approximation) at several streamwise locations (Figure 7.6). Each integral quantity is

normalized by its respective magnitude ($\hat{Q}, \hat{\dot{E}}$, and $\hat{\omega}_{\breve{y}}$) at $\breve{y}/l_h$ = 0.21. As shown in Figure 7.6, the three integral quantities increase at $\breve{y}/l_h$ = 0.35 ($\hat{Q}$ = 1.03, $\hat{\dot{E}}$ = 1.13, $\hat{\omega}_{\breve{y}}$ = 1.24), as additional air is forced into the channel by the interaction between the two air streams entrained through the upper and lower vanes. Additional data demonstrate that the streamwise velocity in the channel accelerates convectively, and that the horizontal vortex formed within the channel intensifies, as measured by the streamwise vorticity flux. Downstream of this location ($\breve{y}/l_h$ = 0.49) the top segment of the vortex already extends above the lower-tier vanes and advected some of the channel flow into the rotating cross flow above. Therefore, while the three integral fluxes increase compared to the initial station ($\hat{Q}$ = 1.01, $\hat{\dot{E}}$ = 1.07, $\hat{\omega}_{\breve{y}}$ = 1.16), they are lower than at $\breve{y}/l_h$ = 0.35. At $\breve{y}/l_h$ = 0.63 the vortex has been advected above the lower-tier vanes, and as a result there is a steep drop in each the integral fluxes between $\breve{y}/l_h$ = 0.49 and 0.63 ($Q_{0.63} = 0.79Q_{0.49}$, $\dot{E}_{0.63} = 0.67\dot{E}_{0.49}$, $\dot{\omega}_{\breve{y},0.63} = 0.45\dot{\omega}_{\breve{y},0.49}$). The largest decrease occurs in streamwise vorticity flux, leaving only the streamwise vorticity advected into the central vortex, and accounting for only 22% of the global axial circulation (cf. Figure 7.3c).

The advection and tilting of the longitudinal vortices from the near-surface into the outer flow are monitored by measuring the flow within the domain above the top horizontal edge of the lower-tier vanes in the domain $1.08 \leq z/h_h \leq 2.08$ (with $\Delta z/h_h \approx 0.08$). The flow in the baseline configuration is measured in the same domain for comparison. Radial distributions of time- and azimuthally-averaged tangential and axial velocity components for each vane configuration are shown in Figure 7.7. The data for the hybrid and baseline configurations are marked in gray and blue, respectively, and the

color intensity (or brightness) corresponds to the increases in the height of the measurement plane. Each velocity component is normalized by the angular velocity, Ω (5.21 s^{-1}), and core radius, R (20.4 cm), of the baseline vortex at z/h_h = 1.08. As discussed in Chapter 6, the vertical evolution of the axial and azimuthal velocity components of the attached two-cell anchored columnar vortex is self-similar (cf. Figure 6.8). Therefore, the baseline data in Figure 7.7 for all elevations collapses and exhibits the expected characteristic linear increase in core radius [$R(z/h_h = 1.08) = 0.96R(z/h_h = 2.08)$] and decrease in peak tangential velocity [$\hat{v}(R, z/h_h = 1.08) = 1.04\hat{v}(R, z/h_h = 2.08)$]. It is remarkable that the radial distributions of the tangential velocity component of the hybrid vortex collapse reasonably well within $r/R_i < 0.33$. Its core radius (as marked by the inner radial peak of the tangential velocity, cf. Figure 7.1a) displays a monotonic increase with height [$R(z/h_h = 1.08) = 0.89R(z/h_h = 2.08)$] and peak tangential velocity undergoes a large decrease [$\hat{v}(R, z/h_h = 1.08) = 1.16\hat{v}(R, z/h_h = 2.08)$]. Within the annular domain $0.1 \leq r/R_i \leq 0.33$ between the two primary concentrations of axial vorticity (cf. Figure 7.3b), the normalized tangential velocity of the hybrid vortex is nominally invariant in elevation but a significant dispersion occurs for $r/R_i > 0.33$. These data show the azimuthally-averaged effect of the advection and tilting of the secondary (longitudinal) vortices as the magnitude of the second tangential velocity peak increases nearly three-fold [$\hat{v}(r/R_i = 0.66, z/h_h = 1.08) = 2.7\hat{v}(r/R_i = 0.66, z/h_h = 2.08)$]. The radial distribution of the normalized axial velocity in the baseline vortex demonstrates an increase in the magnitude of the reversed axial flow along the centerline [$\hat{w}(0, z/h_h = 1.08) = 1.24\hat{w}(0, z/h_h = 2.08)$] and a corresponding increase within the

annular domain $0.18 < r/R_i < 1$ as the flow is accelerated by buoyancy (Figure 7.7b). As the hybrid vortex evolves with elevation, the changes in the radial distribution of axial velocity vary radially. Within the vortex core ($r/R_i < 0.09$) the decrease in centerline velocity [$\hat{w}(0, z/h_h = 1.08) = 0.7\hat{w}(0, z/h_h = 2.08)$] with elevation is accompanied by an increase in the radial gradient of $\hat{w}$ within $0 < r/R_i < 0.09$. Concomitantly, throughout the annular domain $0.09 < r/R_i < 0.5$ $\hat{w}$ increases [$\hat{w}(0.3, z/h_h = 1.08) = 2.46\hat{w}(0.3, z/h_h = 2.08)$]. Finally, for $0.5 < r/R_i < 0.66$, $\hat{w}$ decreases substantially towards the outer edge of this domain, increasing the magnitude of the radial gradient $\partial\hat{w}/\partial[r/R_i]$ from 0.65 to 2.17 between $z/h_h = 1.08$ and 2.08, respectively. The increase in the magnitude of this gradient is related to the azimuthal tilting of the longitudinal vortex by the rotation of the outer flow. This manifests as a steepening of the radial gradient of axial velocity and the advection of axial momentum into the annular domain $0.09 < r/R_i < 0.5$. Owing to the scales imposed by the secondary vortices, the vertical evolution of the hybrid vortex is not self-similar.

The axial variations of the kinetic energy flux $\hat{\dot{E}} = \dot{E}/(\rho g \upsilon R_i^2)$ through a horizontal circular section (radius $r/R_i = 0.66$) of the baseline and hybrid vortices are computed at several elevations within $1.08 < z/h_h < 6.25$ (Figure 7.8). These data show that the axial rate of change with elevation of the kinetic energy flux $\partial\dot{E}/\partial z$ of the baseline vortex increases like z (cf. Figure 5.8) and has a nearly three-fold increase (2.71) between $z/h_h = 1.08$ and 6.25. Similarly, the kinetic energy flux of the hybrid vortex also increases axially [$\dot{E}(z/h_h = 1.08) = 3.46\dot{E}(z/h_h = 6.25)$] but at a much higher rate with elevation. By comparison, the rate of change in the baseline vortex is nominally invariant

within $1.08 < z < 2.08$, as the change in the axial velocity over the same span is small (cf. Figure 7.7b).

Combining the measurement planes of the time-averaged SPIV data for $1.08 \leq z/h_h \leq 2.08$, the vorticity vector, $\vec{\omega} = (\omega_r, \omega_\theta, \omega_z)$ is computed along with the axial gradients of u and v between adjacent horizontal measurement planes ($\Delta z/h_h \approx 0.08$ resolution). These data are used to obtain the integrated axial flux of each vorticity component $\dot{\vec{\omega}} = 12\iint_{-\pi/12}^{\pi/12} w\vec{\omega} r d\theta dr$ through a $\pi/6$ slice of each horizontal plane to account for the 12-fold symmetry of the vane geometry. The integrated flux of each component is normalized by the integrated axial flux of the vorticity magnitude, $\dot{\vec{\omega}}$, at $z/h_h = 1.08$ and its axial variation is shown in Figure 7.9. Initially, the longitudinal vortices between the lower-tier vane channels are tilted vertically and the vortex lines are directed both radially and axially. At $z/h_h = 1.08$, the integrated vorticity flux of these components is approximately the same, $\dot{\omega}_z/\dot{\vec{\omega}}_0 = \dot{\omega}_r/\dot{\vec{\omega}}_0 \approx 0.5$, and there is negligible azimuthal vorticity. Once the longitudinal vortices are advected into the outer flow, azimuthal flow ($|v| > 0$) forces additional tilting due to the shear in the tangential velocity ($\omega_r\, \partial v/\partial r$ and $\omega_z\, \partial v/\partial z$ are the tilting terms in the azimuthal vorticity transport equation), and the advected longitudinal vortical structure acquires all three vorticity components between $z/h_h = 1.08$ and $z/h_h = 1.67$. The increase of the azimuthal and axial vorticity components with elevation accounts for the increased radial gradients of the tangential and axial velocity components for $r/R_i > 0.4$ (cf. Figure 7.7). At approximately $z/h_h = 1.67$, the radial component of the secondary vortex decreases, and the secondary vortices become increasingly dominated by the axial and azimuthal vorticity components. Near the top edge ($z/h_h = 2.08$) of the measurement domain the

axial flux of radial vorticity nearly vanishes and the helical secondary vortices are nearly fully developed.

As shown in Figure 7.3c, despite the redistribution of vorticity the axial circulation of the vortices formed by the baseline and hybrid geometries is nearly identical. It was demonstrated in Chapter 5 that the sole source of axial vorticity in the baseline columnar vortex is the production, and eventual tilting, of radial vorticity within the swirling boundary layer (cf. Figure 5.17). Therefore, the radial circulation (Γ_r) through the side of a cylindrical domain about the axis of symmetry is equivalent to the difference in axial circulation ($\Delta\Gamma_z$) about its top and bottom surfaces. Since the axial vorticity within the enclosure of the baseline vortex is generated within the momentum boundary layer ($z/h_h << 1$), the axial circulation is nearly invariant over a small axial span. Above the boundary layer on the ground-plane, the radial vorticity is negligible ($\omega_r = -\partial v/\partial z \approx 0$) and $\Gamma_r = 0$ so that the circulation equality is satisfied in the baseline configuration. A cylindrical volume of data ($1.08 \leq z/h_h \leq 2.08,\ 0 \leq r/R_i \leq 0.66$) is generated from the SPIV measurements using the 12-fold symmetry of the vane array. Radial distributions of the normalized axial and radial circulations, $Re_z = \Delta\Gamma_z/(2\pi\nu)$ and $Re_r = \Gamma_r/(2\pi\nu)$ respectively, are shown in Figure 7.10a. $\Delta\Gamma_z$ between the top and bottom of the cylindrical control volume increases within the outer flow, $r/R_i > 0.33$, with a peak change of $\Delta\Gamma_z/(2\pi\nu) = 8950$ at $r/R_i = 0.66$ as the secondary vortices are tilted axially and the axial vorticity concentrations with the central vortex column ($r/R_i < 0.33$) remain nearly invariant. Concurrently, there is considerable radial circulation at the vertical edge of the cylindrical volume (θ-z) for $r/R_i > 0.33$ but unlike the baseline vortex $\Gamma_r > \Gamma_z$ as a portion of the radial circulation is converted through tilting to the azimuthal direction.

The variation with elevation of the axial circulation through a circular surface of radius $r/R_i = 0.66$ is shown in Figure 7.10b. For the baseline vortex, the core Reynolds number decreases only slightly with height. However, the hybrid vortex has a three-fold increase in core *Re* within the axial domain $1.08 \leq z/h_h \leq 2.08$, but approaches *Re* of the baseline vortex near $z/h_h = 2.08$. In the higher measurement planes $z/h_h = 4.17$ and 6.25 the axial circulation of the baseline and hybrid vortices are nearly identical (cf. Figure 7.1d).

That the axial circulation of the two types of columnar vortices is invariant despite the substantial increase in the mechanical energy for an identical *Gr* indicates that the redistribution of axial vorticity within the enclosure plays a crucial role in the strengthening of the anchored vortex. This redistribution is quantified by computing the vortical hydrodynamic impulse per unit length through a circular cross-sectional surface about the axis of rotation to describe the first vorticity moment within this plane. The two components of the impulse vector, I_θ and I_z (cf. Figure 6.6b), are calculated at several axial elevations $1.08 \leq z/h_h \leq 6.25$ and shown in Figures 7.10c and d, respectively (normalized by $2\pi\nu R_i$). The variation of the azimuthal impulse with elevation is similar to the axial circulation, and so it is approximately invariant in the baseline vortex, although it decreases slightly with elevation. The azimuthal impulse increases monotonically in the hybrid geometry from $z/h_h = 1.08$ to 2.08 before reaching a maximum near $z = 2h_h$. Unlike the axial circulation, the impulse near the top of the enclosure is not invariant with vane geometry. Consistent with the appearance of the annular concentration of axial vorticity at distal locations from the vortex centerline, $\hat{I}_{\theta,h} = 1.37\hat{I}_{\theta,b}$ at $z/h_h = 4.17$. The distribution of the axial impulse shows a significant difference between the two types of vortices. As discussed in connection with the

formation of the attached two-cell vortex (cf. Chapter 6), azimuthal vorticity concentrations of opposite sign are produced within the shear layer that forms within the vortex core. Negative azimuthal vorticity is produced within the helical shear layer of the recirculating downdraft cell, while azimuthal vorticity of the opposite sign is produced within the helical shear layer that develops between the outer edge of the vortex core and the outer rotating flow. As the vortex evolves above the heated surface, reversed axial downdraft along the centerline deepens, and accelerations in the outer flow due to buoyancy result in an increase and decrease in the magnitudes of the local azimuthal vorticity components. Therefore, the normalized axial impulse decreases with elevation from $\hat{I}_{z,b}$ = 0.19 (z/h_h = 1.08) to $\hat{I}_{z,b}$ = -0.13 (z/h_h = 6.25) as the azimuthal circulation of the flow field decreases with elevation and eventually becomes negative. However, the axial impulse of the hybrid vortex increases over $1.08 < z/h_h < 2.08$ as the secondary vortices (CW, postive) are tilted azimuthally. Once the secondary vortices are fully developed, the axial impulse of the hybrid vortex has a peak at z/h_h = 2.08. The helical secondary vortex structure advects mass and momentum upwards into the annular domain between the vortex core and outer flow. It is this advection that leads to the significant increase in the integrated kinetic energy flux, as manifested by the large positive axial impulse.

The time-averaged three-dimensional distribution of the vorticity vector is used to compute contours of the vorticity magnitude, $|\vec{\omega}|$, shown (normalized by the maximum value of the vorticity magnitude, $|\vec{\omega}|_{max}$) in perspective side and top views of multiple horizontal cross-sectional-planes in Figures 7.11a and b, along with a model of the lower-tier vanes (shaded gray). For visualization of the secondary vortices, the vorticity

magnitude within the central core is saturated above $0.2|\vec{\omega}|_{max}$ and vorticity levels below $0.08|\vec{\omega}|_{max}$ are removed. These data show two secondary CCW vortices emanating from the top ($z/h_h = 1.08$) of adjacent lower-tier channels at the center of the image in Figure 7.11a. Once tilted, these secondary vortices become helically wound around the central vortex column as they are advected clockwise (from above) in the azimuthal direction with the prevailing local tangential velocity (Figure 7.11b). It is noteworthy that at least within the vertical extent of the measurement domain ($1.08 < z/h_h < 2.08$), the vortices remain coherent (i.e., 12-fold symmetry). As noted above, the time averaged helical winding of these vortices about the central vortex column that ultimately merge azimuthally gives rise to the annular domain of time-averaged axial vorticity in Figure 7.3b.

7.3 Redistribution of Vorticity Concentrations

Manipulation of the streamwise vorticity within the ground-plane boundary layer (e.g., Figure 7.4) by the formation and advection of longitudinal vortices between the lower-tier vanes leads to alteration of the distribution of axial vorticity within the baseline vortex. The sensitivity to the formation parameters of the balance between axial vorticity concentrations within the center vortex core and in the outer surrounding flow is investigated by variations of the angle of the lower-tier (φ_h) for a given upper-tier angle ($\varphi = 50°$). The time- and azimuthally-averaged radial distributions of the tangential and axial velocity components (normalized as in Figure 7.1) at $z/h_h = 6.25$ and $Gr = 43 \cdot 10^8$ are shown in Figures 7.12a and b, respectively for φ_h = 15° (the nominal hybrid geometry), 25°, 35°, and 50° (the nominal baseline geometry). For $r/R_i > 0.4$, the radial distributions of velocity for φ_h = 15°, 25°, and 35° remain relatively invariant**.**

Distributions of the tangential velocity demonstrate that the diameter of the central vortex core increases with φ_h, as is evidenced by the changes in the radial position and magnitude of the first peak of $\hat{v}$ in Figure 7.12a. The decrease in vane spacing, as φ_h is increased, corresponds to stronger contraction of the flow in the channels between them, and therefore to an increase in the angular momentum imparted to the flow into the primary vortex and, therefore, an increase in $\hat{v}_{\max}$. However, for $\varphi_h > 35°$ the core continues to spread radially, and the magnitude of $\hat{v}_{\max}$ begins to decrease, ostensibly as a result of increased losses within the lower-tier vane channels. The tangential velocity becomes nearly constant as φ_h varies for $r/R_i > 0.6$. The increased channel losses (or streamwise pressure gradient) with increasing φ_h result in a decrease in the magnitude of $\hat{w}$ (Figure 7.12b), which is most pronounced along the vortex centerline, with the formation of a two-cell vortex for $\varphi_h > 35^o$. These changes in $\hat{w}$ clearly lead to a reduction in the volume flow rate and in the integrated kinetic energy flux of the columnar vortex. It is noted that before the axial extent of the downdraft cell penetrates to below this elevation, the axial velocity distribution is nearly independent φ_h past the local maximum of $\hat{w}$, indicating that the combined effects of altering the distributions of axial vorticity concentrations do not affect the magnitude and radial gradients of $\hat{w}$ (or $\hat{v}$). However, the radial distribution of $\hat{w}$ in the outer flow clearly changes in the presence of the downdraft cell. The corresponding distributions of normalized axial circulation (Figure 7.12c) show that prior to the appearance of the downdraft cell, the radial distributions of the circulation vary within the annular domain between the inner core and the concentration of secondary axial vorticity (cf. Figure 7.3b) where for a given radial position Γ_z increases with φ_h as the concentrations of the secondary vortices migrate

towards the primary core. However, the distributions of Γ_z inside and outside of this annular domain are nearly identical. Therefore, for a given lower-tier vane geometry, φ_h controls the magnitude of the axial vorticity concentrations within the inner and outer domains of the columnar vortex. While the total circulation is invariant with φ_h, the redistribution of the axial vorticity can be quantified by the variation of the impulse vector (Figure 7.12d). The largest azimuthal impulse is measured at $\varphi_h = 15°$ (nominal hybrid vortex), corresponding to the largest axial vorticity concentrations within the annular domain outside of the primary core. As φ_h increases and the magnitude of the secondary axial vorticity concentrations diminishes, the corresponding azimuthal impulse decreases. The axial impulse has a maximum at $\varphi_h = 15°$ due to the large (positive) azimuthal vorticity concentration within the outer flow. As φ_h increases, the reduction in the centerline axial velocity, and eventual development of a two-cell structure, induces a vertical shear layer that generates large concentrations of negative azimuthal vorticity within the primary vortex core, and leads to a diminution of the axial impulse.

The effects of the characteristic height of the lower-tier vanes above the ground-plane (i.e., the depth of the intervane channels) on the annular domain of the secondary vorticity concentrations is characterized by the ratio $h^* = h_h/h$ (i.e., the ratio of the heights of the lower- and upper-tier vanes). The flow field is measured at a fixed elevation ($z/h_h = 6.25$) for $h^* = 0$, 0.04, 0.09, 0.13, and 0.18 for $\varphi_h = 15°$ and $\varphi = 50°$, and the corresponding concentrations of the axial vorticity are shown in Figures 7.13a(*i*–*v*). These data clearly show the profound effects of the lower-tier channel height on the vorticity distribution within the enclosure. In the baseline vortex [Figure 7.13a(*i*)] the distribution of ω_z is continuous within the domain $r/R_i < 0.5$ with a minimum of the

centerline and a peak at $r/R_i = 0.24$. As h^* increases slightly [to 0.04, Figure 7.13a(*ii*)], the vortex develops a strong concentration of ω_z ($\omega_z > 0.5\ \omega_{z,\max}$ for $r/R_i < 0.14$) and decreases monotonically outside of this domain. An annular concentration of secondary vorticity ($0.28 < r/R_i < 0.55$) becomes evident for $h^* = 0.09$ [Figure 7.13a(*iii*)] and thereafter migrates radially outward as h^* increases, while the center core intensifies significantly. It appears that the radial width of this annular domain does not vary significantly as its center radius increases. The raster plots of vorticity are accompanied by distributions of normalized v, w, $\Gamma_{z,}$ and I_z and I_θ in Figures 7.13b through f, respectively. Distributions of the tangential velocity show that the changes imposed by the lower-tier vanes are very pronounced at low h^*, and for $h^* = 0.04$ the annular secondary domain and primary vortex core merge for $0.15 \le r/R_i \le 0.45$. When $h^* = 0.09$, a large increase in $\hat{v}$ at low r/R_i occurs, as the central core of the vortex becomes more concentrated and pronounced, as is evidenced by the formation of the first and second peaks of $\hat{v}$ at $r/R_i = 0.15$ and 0.44. The magnitudes and radial spacing between the peaks of $\hat{v}$ decrease and increase, respectively, as the annular domain migrates radially outward [Figures 7.13a(*iv*) and 7.13a(*v*)]. The characteristic height of the lower-tier vanes also has a profound effect on the radial distributions of axial velocity. Specifically, as h^* increases, the downdraft cell migrates upward, $\hat{w}$ on the centerline reverses its direction, and the magnitude of its radial distribution increases significantly. It is noteworthy that when $h^* = 0.13$, the local minimum on the centerline nearly vanishes and the peak level of $\hat{w}$ is nearly constant for $r/R_i \le 0.25$ [cf. Figure 7.13a(*iv*)]. Compared to the distribution $\hat{w}$ at $h^* = 0.13$, as h^* is increased further ($h^* = 0.18$) its magnitude decreases somewhat near the centerline (6%) but also increases

at larger radii ($r/R_i > 0.28$), indicating further increases in the volume flow rate and the integrated flux of kinetic energy. The axial vorticity distribution is used to compute radial distributions of the core Reynolds number (Figure 7.13c). Similar to the corresponding distributions in Figure 7.12c, the total circulation of the columnar vortex flow is nearly independent of h^*. The distributions at $h^* = 0.13$ and 0.18 clearly show an annular domain with low (or negligible) concentrations of ω_z within the annular domain between the primary and secondary concentrations. The vortex structure at $h^* = 0.04$ shows a monotonic radial increase in Γ_z, but at a higher rate than for the baseline vortex ($h^* = 0$). As the radial location of the maximum radial gradient in axial velocity ($\partial w/\partial r$) migrates away from the centerline with increasing h^*, the axial impulse (Figure 7.14d) increases (nearly linearly) with h^* (the negative value at $h^* = 0$ is due to the helical shear layer induced by the two-cell vortex). As h^* increases, the increase of the axial velocity along the axis of rotation coupled with the advection of momentum due to the secondary vortices, augments the axial momentum and therefore the axial impulse. For $h^* \geq 0.09$, the azimuthal impulse increases nearly linearly as the annular domain of axial vorticity surrounding the central vortex moves radially outwards with a constant strength. For this range of h^*, the axial and azimuthal impulses are nearly identical (similar to the single-cell vortex; cf. Figure 6.6). When $h^* < 0.09$, the variation of the azimuthal impulse with h^* is reduced, as the two vortical structures begin to merge and the decrease in the radial location of the annular concentration of secondary axial vorticity is slowed.

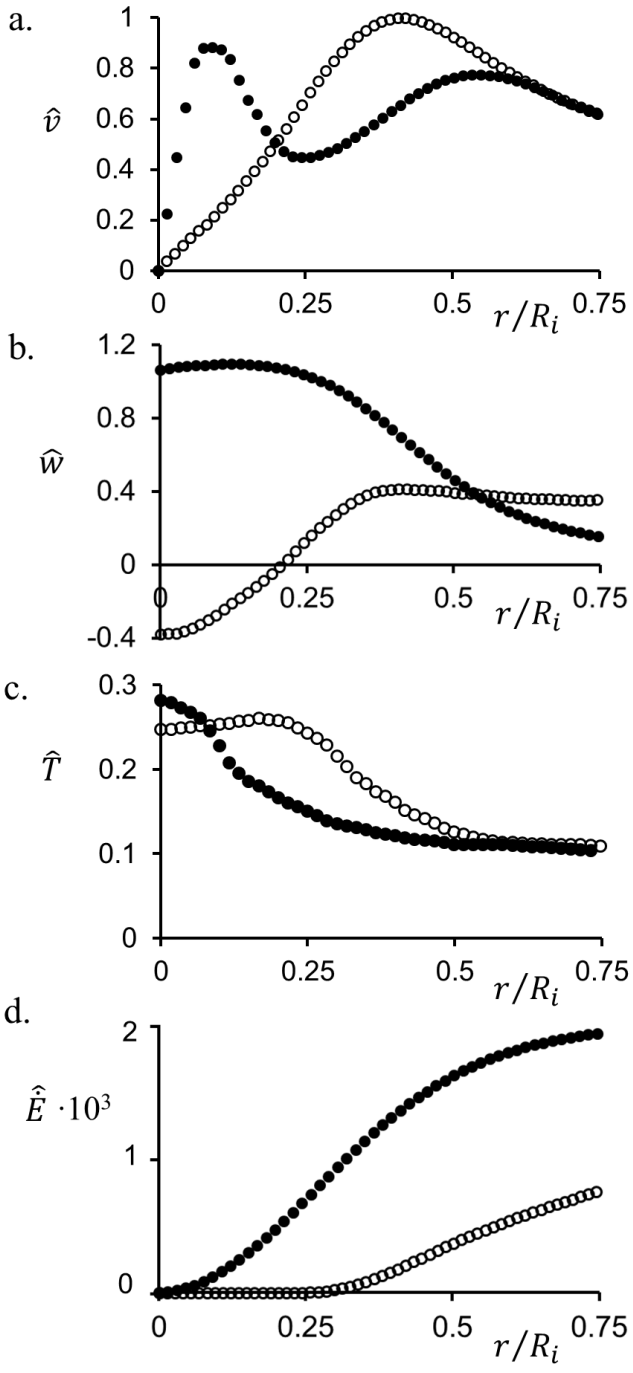

FIGURE 7.1. Time- and azimuthally- averaged radial distributions of normalized (*a*) tangential velocity, (*b*) axial velocity, (*c*) temperature, and (*d*) kinetic energy flux for a baseline, attached two-cell vortex (○) and hybrid vane induced vortex (●) at $z/h = 0.83$ and $Gr = 43 \cdot 10^8$.

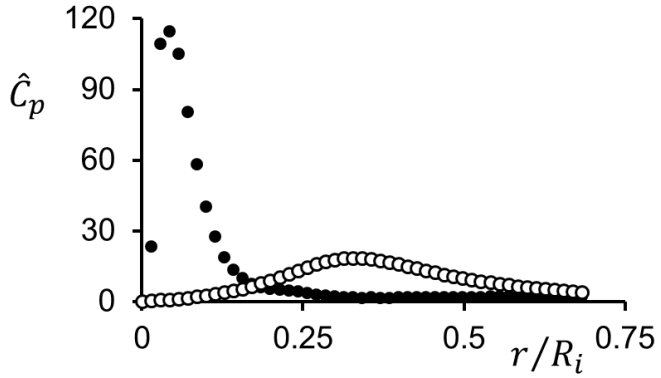

FIGURE 7.2. Radial distribution of the radial pressure gradient of a baseline attached two-cell vortex (○) and hybrid vane (●) induced vortex at $z/h = 0.83$ and $Gr = 43 \cdot 10^8$.

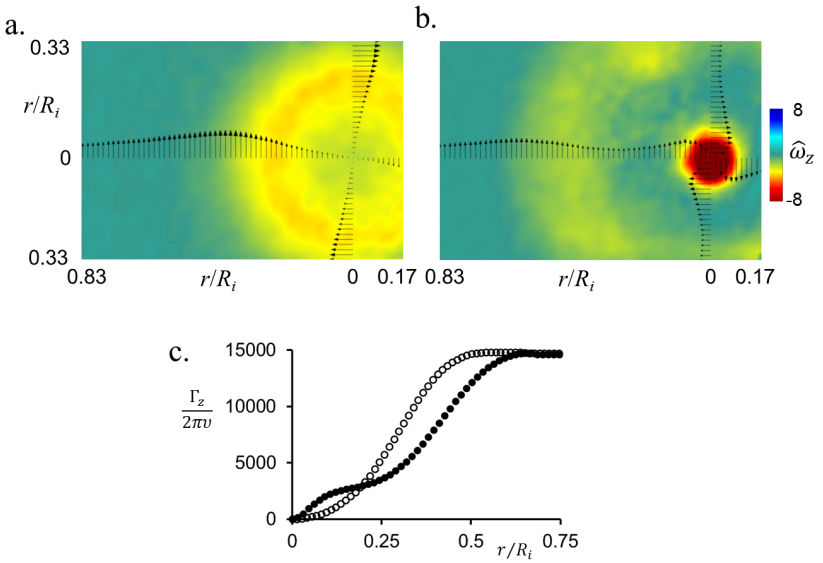

FIGURE 7.3. Time-averaged color raster plot of axial vorticity with radial distributions of tangential velocity for a (*a*) baseline attached two-cell vortex and (*b*) hybrid vane induced vortex and (*c*) the corresponding radial profiles of core Reynolds number: baseline (○) and hybrid (●) at z/h = 0.83 and $Gr = 43 \cdot 10^8$.

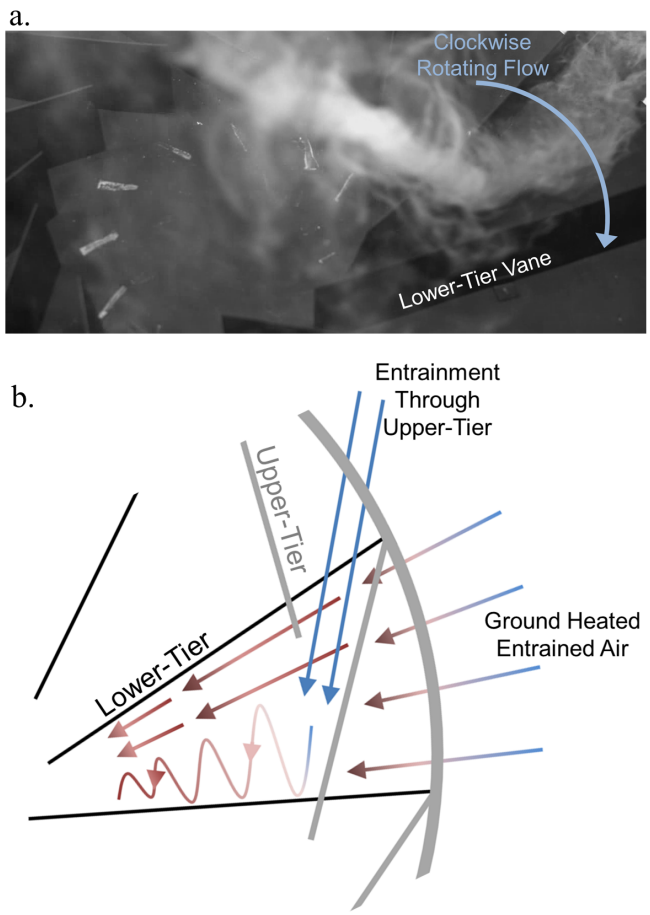

FIGURE 7.4. (*a*) Smoke visualization and (*b*) notional schematic of the horizontal vortex formed between adjacent lower-tier vanes for the hybrid vane configuration.

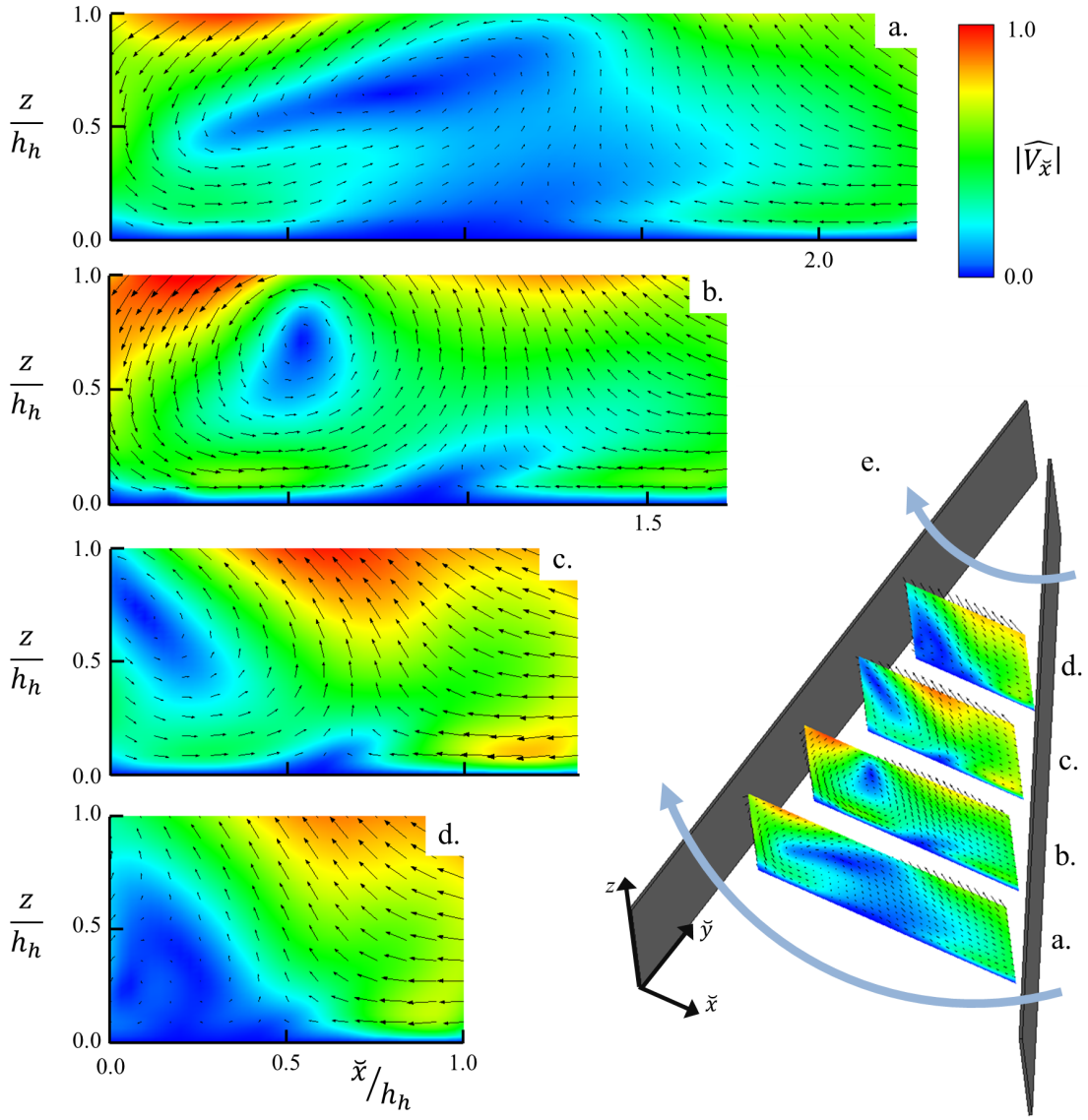

FIGURE 7.5. Color raster plots of normalized in-plane velocities normal to the (*e*) left lower-tier bottom vane in a hybrid configuration at $\breve{y}/l_h$ = (*a*) 0.21, (*b*) 0.35, (*c*) 0.49, and (*d*) 0.63.

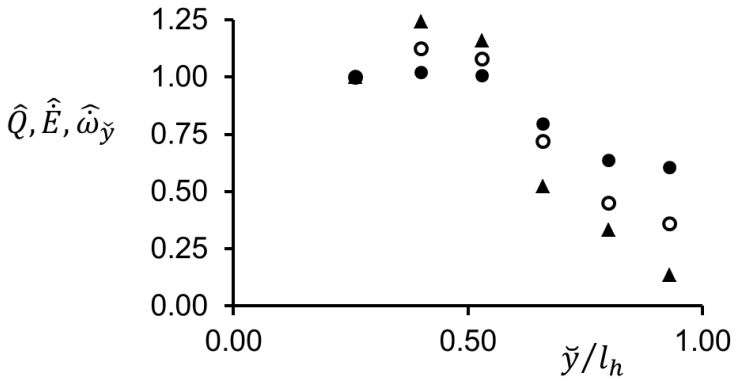

FIGURE 7.6. Variation in volume flow rate (●), integrated kinetic energy flux (○), and streamwise vorticity flux (▲) within the lower-tier vanes.

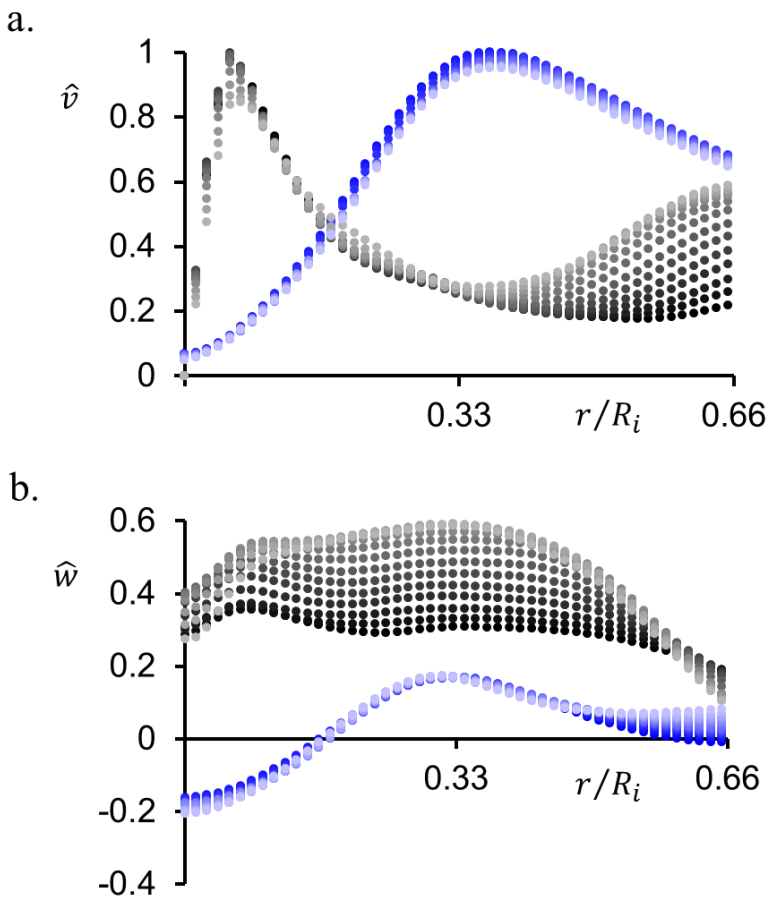

FIGURE 7.7. Time- and azimuthally-averaged radial distributions of (*a*) tangential and (*b*) axial velocity at $\Delta z/h_h = 0.08$ increments for hybrid (●) and baseline (●) configurations where increasing color brightness corresponds to increasing measurement height from $1.08 \leq z/h_h \leq 2.08$ at $Gr = 43 \cdot 10^8$.

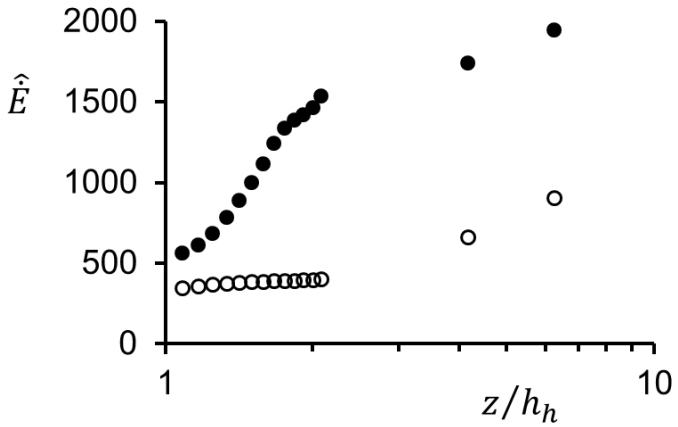

FIGURE 7.8. Axial variation of integrated kinetic energy flux for hybrid (●) and baseline (○) geometries at $Gr = 43 \cdot 10^8$.

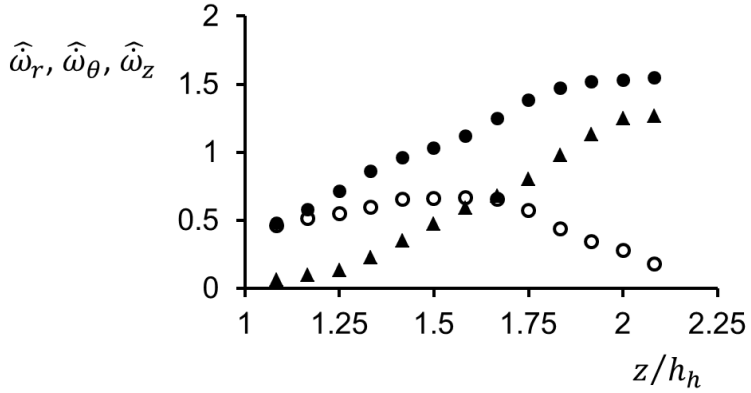

FIGURE 7.9. Variation of the integrated axial flux of axial (●), radial (○), and azimuthal (▲) vorticity with elevation at $Gr = 43 \cdot 10^8$.

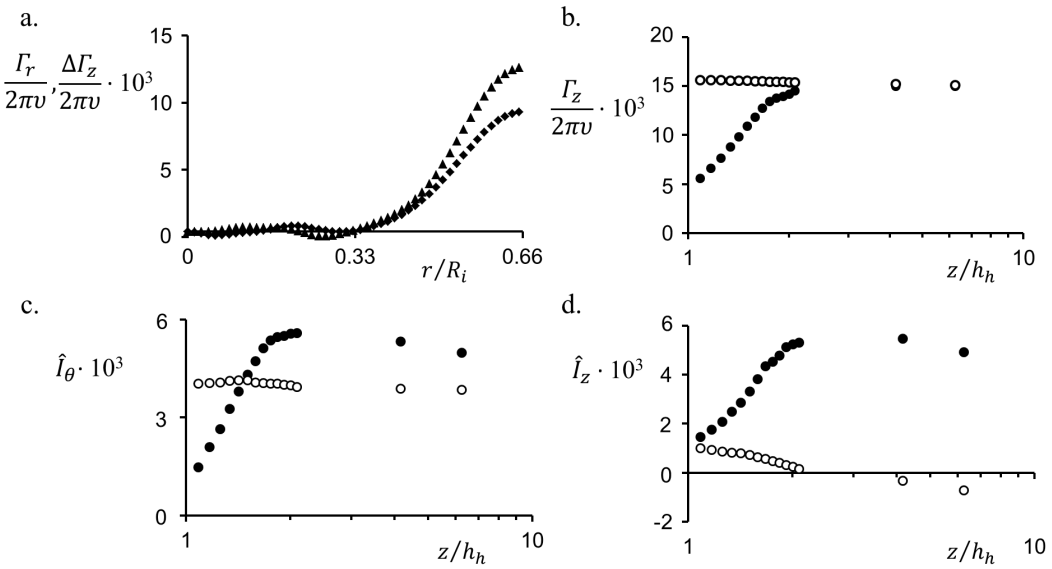

FIGURE 7.10. (*a*) Comparison of the radial (▲) and axial (●) circulations for the hybrid geometry through a radially expanding cylindrical control volume ($1.08 \leq z/h_h \leq 2.08$). Axial variation of (*b*) axial circulation and (*c*) azimuthal and (*d*) axial impulse per unit length for the baseline (○) and hybrid (●) vane geometries at $Gr = 43 \cdot 10^8$.

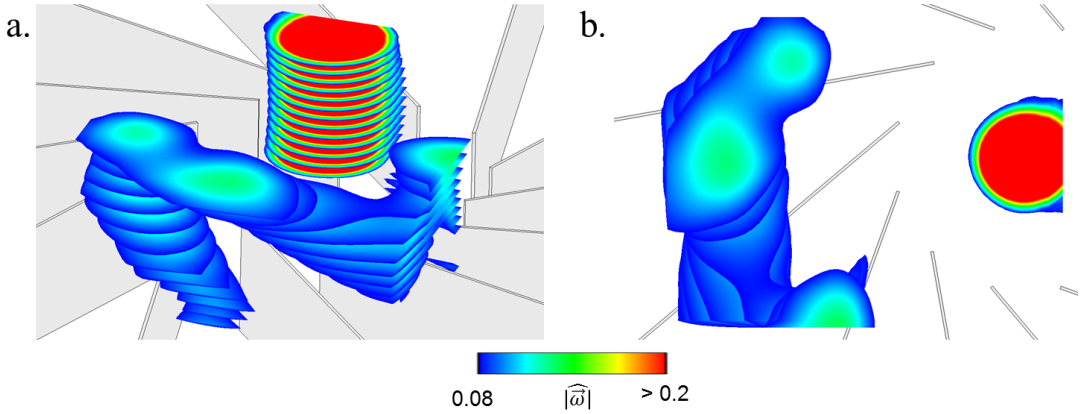

FIGURE 7.11. (*a*) Isometric and (*b*) top view of vertical slices (at $\Delta z/h_h \approx 0.08$ increments) of vorticity magnitude concentrations within the central core and secondary vortices.

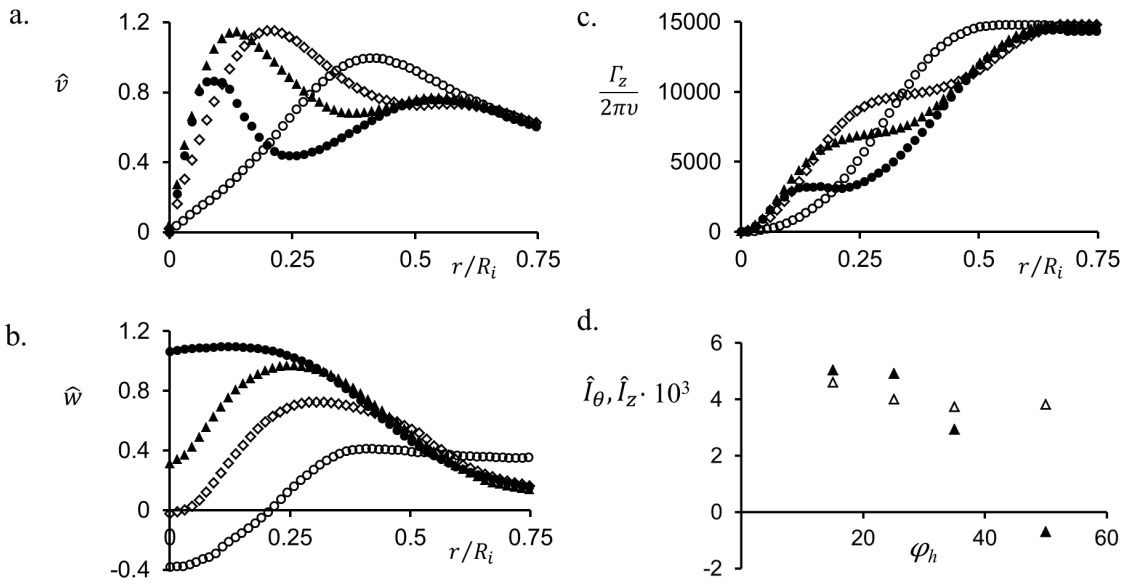

FIGURE 7.12. Radial distributions of normalized (*a*) tangential and (*b*) axial velocity and (*c*) core Reynolds number for φ_h = 15° (●), 25°(▲), 35°(◊), and 50°(○). (*d*) Variations of azimuthal (Δ) and axial (▲) impulse per unit length with φ_h ($Gr = 43 \cdot 10^8$ and $z/h_h = 6.25$).

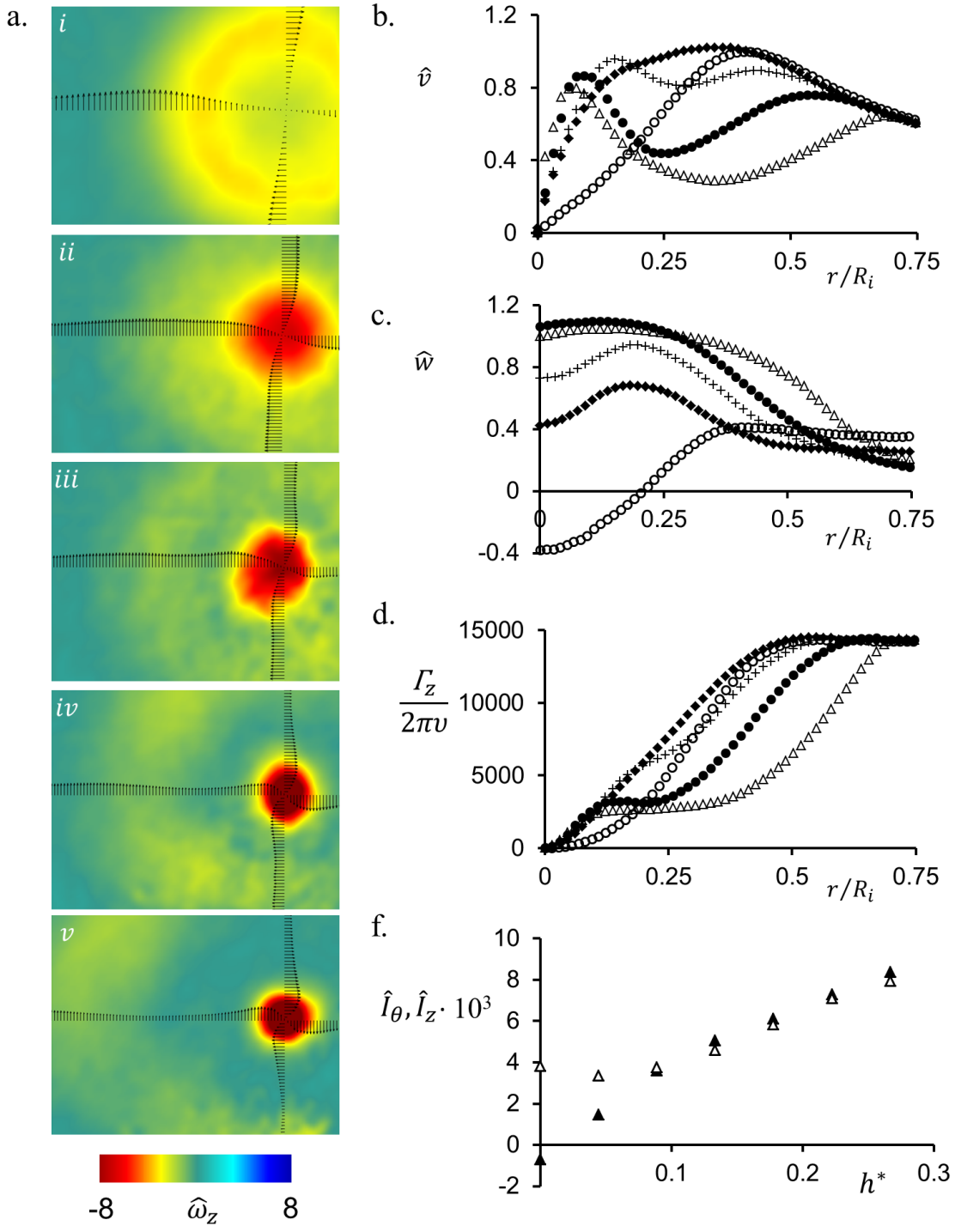

FIGURE 7.13. Radial distributions of normalized (*a*) tangential and (*b*) axial velocity and (*c*) core Reynolds number for $h^* = 0$ (○), 0.04 (♦), 0.09 (+), 0.13 (●), 0.18 (Δ) at $Gr = 39 \cdot 10^8$ and $z/h_h = 6.25$. (*d*) Variations of azimuthal (Δ) and axial (▲) impulse per unit length with h^*. (*e*) Time-averaged color raster plot of axial vorticity overlaid with radial distributions of tangential velocity vectors with variations of h^* ($Gr = 43 \cdot 10^8$ and $z/h_h = 6.25$).

CHAPTER VIII

FIELD TESTS OF OUTDOOR PROTOTYPES

8.1 Overview of the Energy Generation Concept

Power generation using buoyancy-driven, anchored columnar vortices exploits a thermal instability of ground-heated air layers to provide a thermomechanical link between low-grade solar (or industrial waste) heat and electric energy. Electric power is generated by deliberately triggering a columnar vortex within an open-top above-ground cylindrical enclosure and laterally bounded by an azimuthal array of flow vanes. The vortex is centrally coupled along its center of rotation to a specially designed vertical-axis turbine that captures both the tangential and axial momentum of the flow, as shown schematically in Figure 8.1. As discussed in Chapter 1, the anchored columnar vortex is triggered by buoyancy and sustained by entrained makeup air through the tangential vanes as long as a heat source is present. A crucial difference between the vortex that forms in quiescent conditions in laboratory experiments and an anchored vortex in the natural environment is the ambient wind field that can intensify the rotational flow by increasing the tangential momentum imparted to the flow entrained through the vanes. This chapter describes several field tests of two scaled prototypes (having 2 m and 6 m inner diameter) of the vortex enclosure, in which flow is driven only by solar radiation, and then briefly discusses preliminary characterization of the flow field and power generation.

8.2 Experimental Facilities and Diagnostics

The field vortex facilities were designed based on insight provided by the laboratory investigation described in Chapters 3-7. The coupling of the enclosure with an ambient wind field was explored experimentally in wind tunnel investigations by Dr. Pablo Hidalgo at Georgia Tech, and in numerical investigations by Dr. Robert Moser (University of Texas at Austin) and Dr. Arne Pearlstein (University of Illinois at Urbana-Champaign). The field facilities were designed, fabricated, and constructed at Georgia Tech by Mr. John Culp, and then transported to the test site at the former GM Proving Grounds in Mesa, Arizona. The field tests were conducted in May/June and August of 2014 (on asphalt surface) and June and August 2015 (on unimproved land).

The 2 m Field Facility

The 2 m facility (Figure 8.2) was used in May/June 2014, and is based on twelve equally-spaced vertical (2.5 cm diameter) posts connected to 2 m diameter wooden and steel rings at their top and bottom edges, respectively, to form the structural backbone of the facility. The two-tier hybrid flow vanes (cf. Chapters 3 and 7) are constructed from 13 mm thick plywood boards painted black to improve the background contrast for smoke visualization photography. Each upper-tier vane (l = 0.8 m by h = 0.92 m) is set to an angle of $\varphi = 50°$ with respect to the radial direction, and is attached to and can pivot about the vertical post 0.7 m from its inner vertical edge, such that the inner diameter of the enclosure is D_i = 1.7 m. The lower-tier vanes (l_h = 1 m by h_h = 0.15 m, h^* = 0.14) are set at $\varphi_h = 15°$, have an inner enclosure diameter D_h = 0.4 m, and are each attached to the vertical post (below the upper-tier vanes) 0.9 m from their inner vertical edge. A clear plastic shroud (0.6 m tall) is attached around the upper circumference of the enclosure

(overlapping 4 cm of the top edge of the upper-tier vanes) to mitigate interaction between the ambient wind field and the vortex flow (Figure 8.2a).

Figure 8.2b shows the assembled 1.65 m diameter six-bladed, vertical-axis rotor. Each blade is comprised of 6 Styrofoam elements fabricated using hot-wire cutting, mounted side-by-side along a radial 1 cm diameter spar attached to a 10 cm central hub, which is connected through a rotor assembly to a dynamometer. Each element has a 13 cm span with a *c*-shaped, 19 cm chord and can be individually rotated about the spar to allow for discretized, variable-twist configurations. The entire turbine assembly is supported by a surrounding steel tubing structure (Figure 8.2a) that allows for elevation adjustment through the four jack-screw assemblies at each of the support structure corners**.** The turbine and support structure subsystem is assembled on casters to allow easy removal, providing the opportunity to test vortex initiation and sustainment in the absence and presence of the rotor assembly.

The primary diagnostics include smoke visualization and measurements of the mechanical power using a custom-designed hysteresis brake dynamometer (Magtrol HB-50, 50 oz·in, Figure 8.2c). The hysteresis brake produces a controllable and repeatable mechanical load on the rotor shaft. The angular speed and total torque of the rotor were measured by an optical encoder (US Digital E5, 2500 cycles per revolution) and a torque transducer (Transducer Techniques, 0-50 oz·in range), respectively. These measurements provide an estimate of the extracted mechanical power from the flow field. The hysteresis brake is controlled through a current-regulated power supply using an analog output module and the signals of the torque transducer and encoder are recorded at 0.4 Hz using analog input and differential digital input modules, respectively. Due to the

inherent fluctuations of the ambient wind (cf. Figure 8.7), the rotor RPM varies significantly for a constant brake torque, complicating the quantification of the performance of the anchored vortex. A software-based controller was devised and implemented in an attempt to maintain a constant rotor angular velocity (Figure 8.2d) to minimize RPM variability and maximize power by maintaining an optimal rotor speed (nominally 10-12 RPM). The controller proportionally adjusts the mechanical load using the hysteresis brake when the rotor speed is above 6 RPM, and enforces a deadband below this speed. The power data presented for the 2 m scale facility (cf. §8.4) were acquired using this control scheme, but due to inherent time delays in the software and hardware used during the field test, power optimization could not be achieved.

The 6 m Field Facilitiy

The structural backbone of the 6 m facility is an azimuthal array of twelve 5-cm diameter vertical posts each 2.84 m tall, mounted between and supported by two horizontal regular dodecagons. Each side of the ground dodecagon is made of a 1.27 cm thick, 160 cm long steel plate with a low-profile flange at each end. Each side of the upper dodecagon is made of a closed aluminum square channel measuring 10 x 15 x 160 cm, with 0.64 cm thick walls and welded connection flanges at each end. The top dodecagon and the 12 vertical posts support a conical contraction section assembled from 12 plane trapezoidal frames constructed from extruded aluminum channel bars (5.08 x 1.27 cm cross-section) and covered with translucent 0.15 mm thick polyethelyne sheet. The trapezoidal frames, each measuring 1.5 and 0.65 m at their base and top and with side 2.54 m long, are attached to each other along their nonparallel sides to form a 2 m high contraction cone (42% contraction ratio by area) that is open at its

bottom and top ends and mounted on top of the upper horizontal dodecagon of the facility (Figures 8.3 and 8.4) to mitigate interference of cross-flow ambient wind with the anchored vortex flow.

The 2015 field tests used two separate designs of upper- and lower-tier vanes. In the first design (D-1) each upper-tier vane is made of a frame constructed from 2.56 m tall vertical aluminum channel material (5 x 1.2 cm cross-section) and 6 1.98 m long horizontal fiberglass bars (5 x 0.6 cm cross-section) attached to the vertical aluminum channels at equally-spaced elevations (Figure 8.3a). Each 1.98 x 2.56 m vane is covered with translucent 0.15 mm thick polyethelyne sheet that provides an impermeable surface for directing the entrained air flow into the vortex enclosure. Each vane can also be bent along the flexible horizontal fiberglass rods that are used as batons to support the plastic sheet, thereby forming curved vanes with an adjustable radius of curvature. The upper-tier curved vanes are attached to, and can independently pivot about, the vertical posts at 1.88 m from the inner vertical edge (when the upper-tier vanes are planar). Outside the enclosure, an outer segment is hinged to each vane along its height and can be independently adjusted as a flap with a 0.3 m chord. The lower-tier hybrid vanes are constructed from flexible, 10 mm thick fiberglass sheet, measure 2.44 m long and 0.15 m high ($h^* = 0.055$), and are attached to the vertical posts 2.36 m from their inner edge (when the lower-tier vanes are planar). The hybrid vanes can also be bent along their lengths (independently of the top-tier vanes) to form curved vanes. A schematic of the nominal vane geometry is shown in Figure 8.3b.

In the second design (D-2), the upper-tier vanes protrude *outward* from the enclosure using segments of portable chain-link fence (Figure 8.4). Each segment

consists of a metal frame 4.3 m long and 2.5 m high, with standard chain-link material within the frame, and extends away from the structure with one 4.3 m side on the ground. Each frame can pivot about a secondary vertical post inserted in the ground parallel and in close proximity to one of the 12 vertical posts of the enclosure. A vertical post mounted in a portable, ground-based fixture supports the outer end of each fence segment so that the outer end can be independently rotated about the fixed inner post. Each fence segment is covered with standard translucent 0.15 mm thick polyethelyne sheet to provide an impermeable vane boundary for directing the entrained air flow. The lower-tier vanes are constructed from opaque, flexible, 10 mm thick fiberglass sheets, 4.6 m long and 0.15 m high ($h^* = 0.06$), and hinged at their midpoint about the vertical posts of the enclosure so they extend both into and out of the enclosure with an angle independently adjustable with respect to the upper-tier. Outside of the facility, the lower-tier vanes extend straight from their hinge point to the midpoint of the adjacent upper-tier vane in the clockwise direction. Inside the facility, the curvature of each lower-tier vane was adjusted using a rope-pulley system that applies tension between the hinge point and its inner vertical edge. A schematic of the nominal vane geometry is shown in Figure 8.4a. The assembled facility at the test location is shown in Figure 8.4b. The inside of the facility using D-2 vane design (constructed on unimproved landscape) is shown in Figure 8.4c, demonstrating the curved lower-tier vanes ($D_h = 1.6$ m). The curvature of each lower-tier vane is set by its chord length (2 m) for constant arc length (2.26 m) and its root is offset from the inward radial direction by $\varphi_h = 15°$.

Diagnostics during the 6 m scale field tests included a radial array of vane anemometers (Dwyer Instruments, VP1 100 mm vane thermos-anemometer probe). The

anemometer rake (Figure 8.4d) consists of nine sets of corresponding azimuthally and axially oriented anemometers radially spaced at $\Delta r = 28$ cm within $0.28 \leq r \leq 2.52$ m and placed at an elevation of $z = 2.13$ m ($z/h = 0.85$) from the ground-plane. The rotation frequency of each anemometer is sampled at 0.4 Hz using dedicated DAQ modules that provide radial distributions of the tangential and axial velocity within the enclosure.

8.3 Environmental Conditions

The ambient wind speed at the test site is measured at 1 m and 2 m elevations using two three-axis ultrasonic anemometers (RM Young Model 81000) that are sampled at 0.4 Hz (Figure 8.5a). These wind speed measurements are augmented by a dedicated weather station (Davis Instruments wireless Vanage Pro2 Plus) that records one-minute averages of the ambient air temperature and solar radiation. Higher spatial resolution temperature data is also recorded using vertical rakes of thermocouples (T-type) 0.5 and 2 m tall (Figure 8.5b) to characterizate the local thermal boundary layer. The measurements are sampled at 0.4 Hz using a 16-channel DAQ with a thermocouple input module.

Characteristic diurnal variations in solar radiation and air temperature (at 1 m) at the test location in Mesa, AZ (recorded during the 2 m scale field investigation on June 4, 2014) are shown in Figure 8.6a and b. The solar radiation above the ground-plane is recorded by the pyranometer beginning shortly after sun rise (approximately 5:00 am), and the insolation reaches a maximum of 950-1000 W/m^2 at approximately 12:30 pm with cloudless skies. The ground-plane thermal gradient (corresponding to the surface heat flux into the adjacent air layer) reaches a maximum at this time. The air temperature 1 m above ground level begins to rise 45 minutes after sunrise, is 39.2°C at

12:30 pm, and reaches a maximum of 41.3°C at 4:53 pm as the sensible heat flux from the surface continues into the adjacent air long after peak insolation has ended (Figure 8.6b). Corresponding temperature distributions measured at 12:30 pm are shown in Figure 8.6c. The 2 m rake is located approximately 10 m from the vortex facility (cf. Figure 8.5b) while the 0.5 m rake is placed at the inlet of the azimuthal array of flow vanes. These measurements show that thermal boundary layer decays with the vertical (z) coordinate. Despite their different locations with respect to the facility, the similarity between the two temperature profiles indicates that the 2 m scale facility did not significantly alter the local temperature field, and that the axial thermal gradient is approximately constant over the ground-plane.

The local ambient wind was also measured over a 24-hour diurnal cycle (June 4, 2014) using the ultrasonic aneometer at 1 m. It was found that significant vertical velocity fluctuations owing to buoyantly driven flows are induced by strong suface solar heating during daylight hours beginning shortly after sunrise and reaching a maximum ($|w| > 1$ m/s) between 11:00 am and 6:00 pm (Figure 8.7a). These fluctuations occur as surface heated air rises and induces mixing that ultimately reduces the thermal gradient and adds stability to the stratified air layers. Concomitantly, the local ambient wind field can reach horizontal speeds of up to 8 m/s during the day (Figure 8.7b), and the largest wind speeds are recorded during daylight hours when solar insolation and surface thermal gradients are also maximum. These fluctuations are significantly reduced after sunset as the buoyancy-driven flow diminishes. It is important to note that while sporadic or sustained wind gusts obviously can and do occur during the night (e.g., around 4:00 am) they lack the magntiude and fluctuations compared to the ambient

wind field during the afternoon hours. The ambient wind field in which the facilities are imbedded is forced into the enclosure, turned tangentially by the flow vanes to assist in the formation and strengthening of the columnar vortex, and is thus an inherent part of the power generation system. Therefore, characterizing the wind field is necessary for quantifying the power generation capabilities of each field facility.

8.4 Field Test Measurements

Characterization of the prototype field facilities was completed in successive summer expeditions to the Arizona desert. The 2 m scale test focused on the initiation of an anchored, buoyancy-induced columnar vortex and its coupling to a vertical-axis turbine. The goal of the 6 m scale tests is the optimization of the induced flow field by two vane designs, and their effects on the distributions of tangential and axial velocity and integrated kinetic energy flux.

2 m Scale Field Prototype

An anchored vortex column having a nominal diameter of 0.4 m is successfully initiated, maintained, and directly coupled to the spinning rotor during the 2 m scale outdoor field test. The columnar vortex is visualized by injecting theatrical fog near the ground-plane between two lower-tier vanes (Figure 8.8a). Similar to the laboratory vortex, a central column is formed (visualized by fog injection) that scales with the inner diameter of the lower-tier vanes. The vortex is shown to spread considerably as it approaches the plane of the rotor due to the inherent blockage of the turbine. The vortex was formed in the absence and presence of cross-wind or gusts prevalent during the day and demonstrates significant strengthening in the presence of sustained ambient wind currents.

The 2 m facility is operated and monitored continuously for nearly 24 hours using the control scheme described in §8.2. Figure 8.8b shows the time history of the ambient wind speed and the power generated by the facility during that 24 hour period. Daytime power is clearly characterized by strong vortex intensification due to entrainment of heated ambient air as demonstrated by the significant peaks in power (greater than 1 W) during periods with large wind fluctuations. The ramping up and down of extracted power following the trajectory of the sun is clearly visible with peak power production occurring during the afternoon hours when solar surface heating is maximum (cf. Figure 8.6a). No start-up issues are encountered as the rotor under small variable load maintained rotation throughout the night in response to even a very light breeze. It is noteworthy that throughout the night the rotor only stopped for 2 short intervals totaling 25 minutes. The significant increase in the extractable power between day (average power from 12:00 pm to 6:00 pm is 173 mW) and night (12:00 am to 6:00 am is 25 mW) is due to the formation of the buoyancy-driven air motions induced by the anchored, columnar vortex.

6 m Scale Field Prototype Vane Configuration D-1

Field tests of the D-1, 6 m scale enclosure (without a rotor) were conducted to investigate vortex formation and performance characteristics using flexible vanes that provided the ability to adjust their curvature, and a conical contraction to reduce interference by the ambient wind above the level of the vanes (cf. §8.2). A vortex column having a nominal inner diameter of 1.2 m is successfully initiated, maintained, and visualized. The votex extends through the array of upper- and lower-tier vanes, and rotation continued through the conical contraction. The columnar vortex is visualized by injecting theatrical fog through flexible aluminum tubing near the ground-plane

(Figure 8.9). The vortex strength is significantly enchanced by the entrainment of ambient air effected by local wind, which enhances the nominal solid-body rotation at the outer radial edge of the vortex and increases the entrainment of ground-heated air into the core. It is important to note that the vortex was continuously present throughout the day, even in the absence of cross-wind.

During the field testing of the D-1 enclosure, a radial array of vane anemometers was used for *separate*, nonsimultaneous measurements of the tangential and axial velocity components of the vortex low field within the enclosure. Rotating the radial rake by 90° about its axis provided measurements of the axial or tangential component. For a given radial profile, the anemometer output is sampled and recorded at 0.4 Hz during a 15 minute interval. Given the dependence of each velocity component on the ambient wind field, time averages are not representative of the true variation of the velocity. Furthermore, since the two velocity components are not measured *simultaneously*, each time series is sorted (using 0.1 m/s increment bins) based on the magnitude of the ambient wind field (using the time-resolved measurements of the ultrasonic anemometers). The average radial distributions of the two velocity components as a function of wind speed constructed from these data are shown in Figure 8.10a and b (the magnitude on the centerline, $r = 0$, is zero for the tangential velocity and linearly extrapolated for the axial velocity). It is important to note that the curved vane geometry is such that the inner diameter of the vane array, D_i, is only 4 m. The measurements are taken at an elevation of 2 m above ground (just below the bottom of the cone) for concave (relative to the incoming entrained flow) upper-tier vane curvature with a 1 m opening between adjacent vanes. The lower-tier vanes maintained a

convex curvature (shown schematically in Figure 8.3b). These velocity distributions demonstrate that the magnitudes of the azimuthal and tangential velocity components increase with ambient wind speed. The tangential velocity profile nearly resembles solid-body rotation, where the highest azimuthal velocity occurs well outside of the inner tip of the lower-tier vanes, indicating that the vortex spreads radially and nearly fills the enclosure at the upper end of the vanes. From these velocity distributions the integral of the kinetic energy flux over a horizontal plane [$\dot{E} = \iint \frac{\rho}{2}(v^2 + w^2)(\vec{V} \cdot \hat{n})dA$] is calculated as a function of ambient wind speed and for this geometry, peak power of up to 180 W is realized (Figure 8.10c). It is seen that the mechanical power within the enclosure scales approximately with the square of the ambient wind speed.

6 m Scale Field Prototype Vane Configuration D-2

During August 2015, field tests of a redesigned (D-2) 6 m scale enclosure (without a rotor) were conducted to investigate the effect of frontal area and interactions with ambient wind and air currents on the air flow into and within the enclosure and the mechanical characteristics of the columnar vortex. The structural elements of the enclosure and the cone are unchanged from D-1 (cf. §8.2). During testing, radial rakes of vane anemometers were operational and are used to generate simultaneous radial distributions of the axial and tangential velocity components along the inner radius of the enclosure (R_i = 3 m). Data are recorded at a sampling rate of 0.4 Hz for one hour. Figures 8.11a and b show characteristic *time-averaged* profiles of the tangential and axial velocity, respectively, during midafternoon (1:00 pm to 2:00 pm) when the upper-tier angle is φ = 51° (φ_h = 15°, h^* = 0.06). During these measurements, the average air temperature at an elevation of 1 m was 41°C. Each profile is normalized by its respective

value of tangential velocity at $r/R_i = 0.36$. The measurements demonstrate the presence of two local maxima of the tangential velocity ($r/R_i = 0.27$ and 0.74) associated with the presence of the lower-tier vanes. However, the flow is dominated by the maximum at $r/R_i = 0.74$, which is more than three times larger than the magnitude of the inner peak [$\hat{v}(r/R_i = 0.74) = 3.03\hat{v}(r/R_i = 0.27)$]. This increase in azimuthal velocity at the outer edge of the facility is a result of strong entrainment and interaction with the ambient wind field, and is directly attributable to the vanes. Similar to natural dust devil vortices, the entrainment of ambient air accelerates the azimuthal flow and interacts with the lower-tier vanes to increase the strength of the secondary vortex structures. The result is a significant increase in angular momentum far from the vortex centerline. It is noted that the axial velocity is almost radially-invariant, indicating that axial flux could be enhanced with further improvement of the vane design.

The effect of the ambient wind on the radial distribution of the velocity field within the enclosure is demonstrated in Figure 8.12. The instantaneous data (vane and ultrasonic anemometers) are boxcar-averaged over ten sample increments (≈ 25 seconds) to remove small fluctuations and account for latency between the ambient wind and the reaction of the vane anemometers within the facility. The boxcar-averaged anemometer data are then binned by the measured wind speed outside of the facility in 0.1 m/s increments, and each bin is averaged to produce radial profiles of velocity for a different ambient air speed. Figure 8.12 displays five such profiles from 1.2 m/s to 6 m/s at 1.2 m/s increments. The magnitude of the outer radial extent of the tangential velocity distribution increases more strongly with wind speed than at other radial locations, and the local minimum between the two vortex structures disappears. Due to the frontal area

of the outdoor facility, as the velocity of the ambient wind increases so does the volume flow rate through the facility, leading to a proportional increase in the axial velocity. Figure 8.12b shows that the axial velocity remains approximately radially-invariant regardless of the wind currents outside the facility, with a nearly proportional increase in the magnitude of the axial velocity and volume flow rate [Q(6 m/s) = 4.8Q(1.2 m/s)] with increasing wind speed. It is noted that the velocity magnitude of the flow field within the array of vanes is less than the ambient wind entrained into the facility.

The time-dependent mechanical power [the integral of the kinetic energy flux over the horizontal exit plane] is calculated from a 60-minute record of the instantaneous tangential and axial velocity traces (black line in Figures 8.13a) along with the corresponding variation of the ambient wind speed measured by the ultrasonic anemometers (gray line). The 60-minute time-averaged integral of the kinetic energy flux is 107 W (denoted by the dashed line) with an RMS of 79.4 W and peak power of 784 W, while the corresponding time-averaged wind speed is 3.4 m/s. These data show that the fluctuations of mechanical power do not follow closely the changes in wind speed (during this time, the wind direction was reasonably invariant, within ± 15^{o}). In particular, the mechanical power is frequently lower than what is expected for a given wind speed (see for example, the power and wind speed between 20 and 35 minutes). While ambient wind enhances the vortex for the anchored columnar vortex and the naturally-occurring dust devils, it appears that the design of the vanes can be further improved to enhance interactions between the anchored vortex and the wind. The 5-minute samples of mechanical power and ambient wind speed for the same vane geometry are shown in Figures 8.13b and c. For *each* sample period, the nominal

average wind speed is 4 m/s, but there is significant dispersion in the mean power, from approximately 0.3 to 1 kW.

The time series of mechanical power (Figure 8.13a) is boxcar-averaged and binned by ambient wind speed and the functional dependence of power generation with wind speed is shown in Figure 8.14a. For the nominal field facility geometry ($\varphi = 51°$, $\varphi_h = 15°$, $h^* = 0.06$), the mechanical power is proportional to $U_{\text{wind}}^{5/2}$ (where U_{wind} is the velocity of the ambient wind field) with $\bar{\dot{E}} = 86$ at the average wind speed of 3.4 m/s. Note that the data at low wind speeds is rather sparse (less than 5% at wind speed lower than 1 m/s, and less than 25% between 2 and 3 m/s) since wind is prevalent most of the time. These data demonstrate that the ambient, thermally-driven wind is an important contributor to the strength of the anchored columnar vortex.

Two additional upper-tier vane angles ($\varphi = 42°$ and $33°$) were investigated while maintaining the lower-tier vane settings. These data (sampling rate of 0.4 Hz for one hour) are box-car averaged and binned by ambient wind speed and their variation with ambient wind speed is shown in Figure 8.14b. As the angle of the upper-tier azimuthal array decreases (becoming increasingly more radial) the power generation at low ambient wind speeds decreases, and the columnar vortex induced by buoyancy alone (without wind) becomes weaker. Alternatively, the dependence of the kinetic energy flux on the ambient wind speed becomes more significant, varying like $U_{\text{wind}}^{3.5}$ and $U_{\text{wind}}^{4.25}$ for $\varphi = 42°$ and $33°$, respectively. As the upper-tier becomes more radial, the frontal area of the facility increases and harvests additional kinetic energy from the wind field leading to a larger increase in the integrated kinetic energy flux for significant ambient winds. At

larger wind speeds (> 3 m/s), $\varphi = 42°$ and 33° produces nominally equivalent power for identical wind speed.

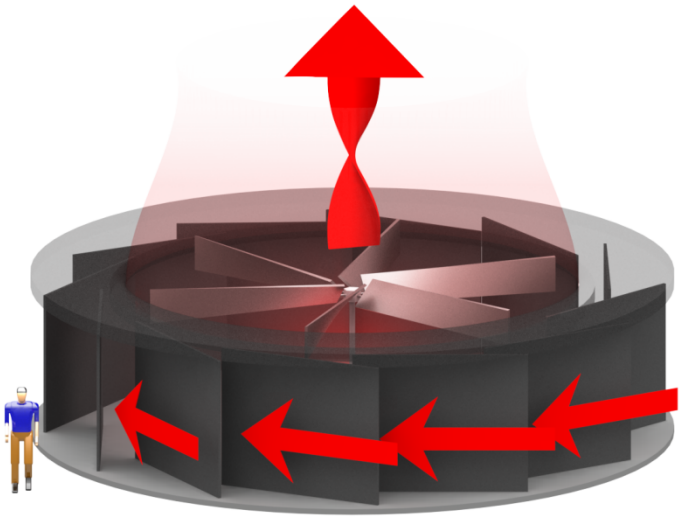

FIGURE 8.1. Schematic representation of the power generation concept using a buoyancy-induced, columnar vortex coupled to a vertical-axis turbine.

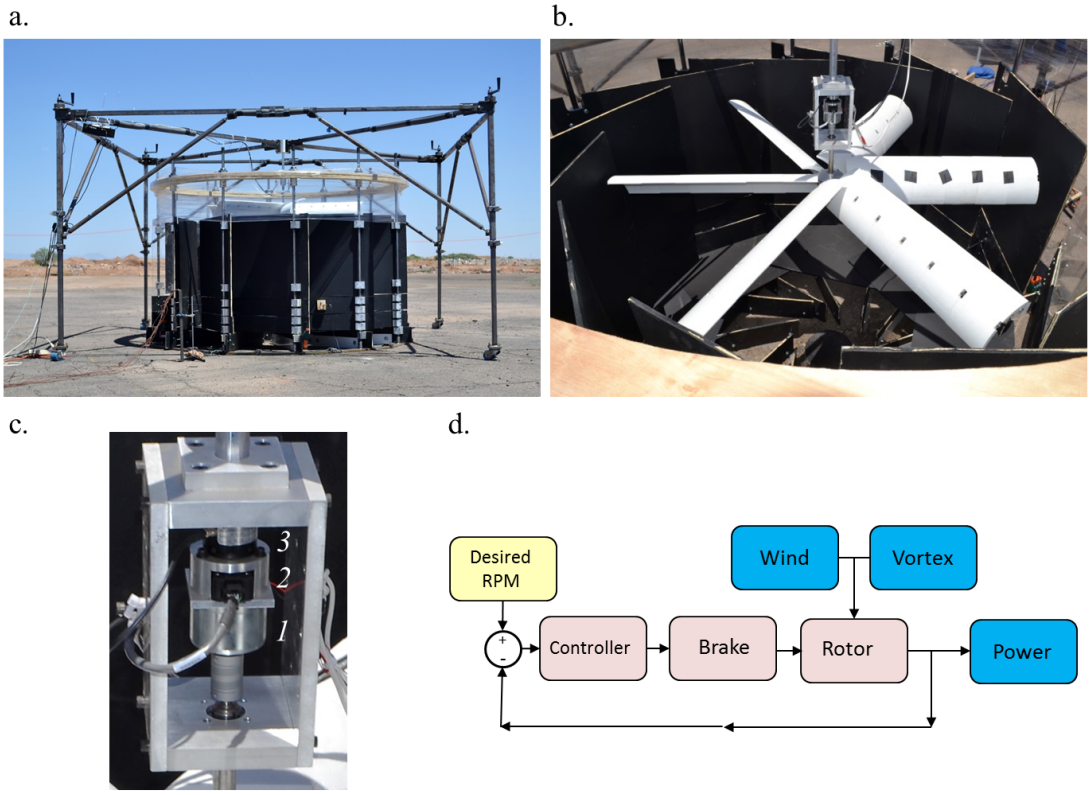

FIGURE 8.2. (*a*) Assembled 2 m scale facility in Mesa, AZ and (*b*) 1.65 m diameter rotor used during testing. (*c*) 2 m scale field facility hysteresis brake (*1*) dynamometer with optical encoder (*2*) and torque transducer (*3*). (*d*) Field-implemented control schematic for attempted optimization of turbine RPM through variation of mechanical load applied to the rotor shaft.

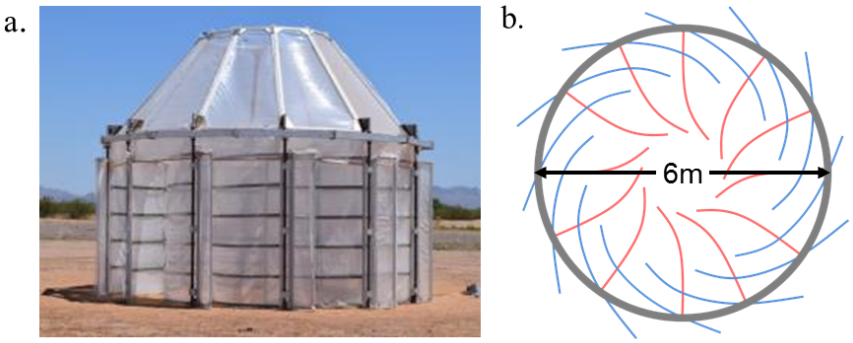

FIGURE 8.3. (*a*) Assembled 6 m scale (D-1) field facility (*b*) schematic of field facility vane geometry (D-1) showing upper- (blue) and lower- (red) tier vanes.

a.

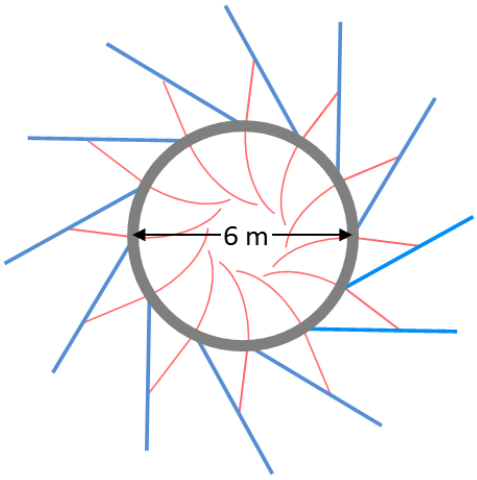

b.

c.

d.

FIGURE 8.4. D-2 field facility showing (*a*) schematic of the upper- (blue) and lower- (red) tier vane geometries, (*b*) field facility at test site, (*c*) inside view of lower-tier geometry , and (*d*) radial array of vane anemometers.

a. b.

FIGURE 8.5. Environmental diagnostic equipment photographed during 2 m scale field testing: (*a*) sonic anemometer, weather station, and (*b*) thermal boundary layer rake.

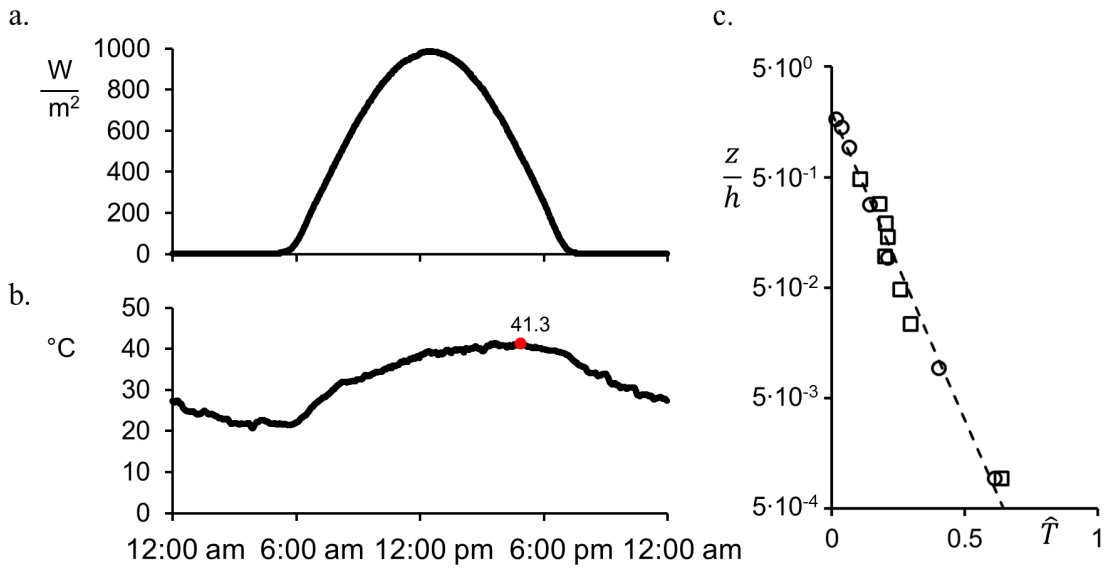

FIGURE 8.6. Characteristic diurnal variation in (*a*) solar insolation and (*b*) air temperature at z = 1 m (maximum air temperature is denoted in red). (*c*) Thermal boundary layer profile at the test site during peak insolation (June 4, 2014).

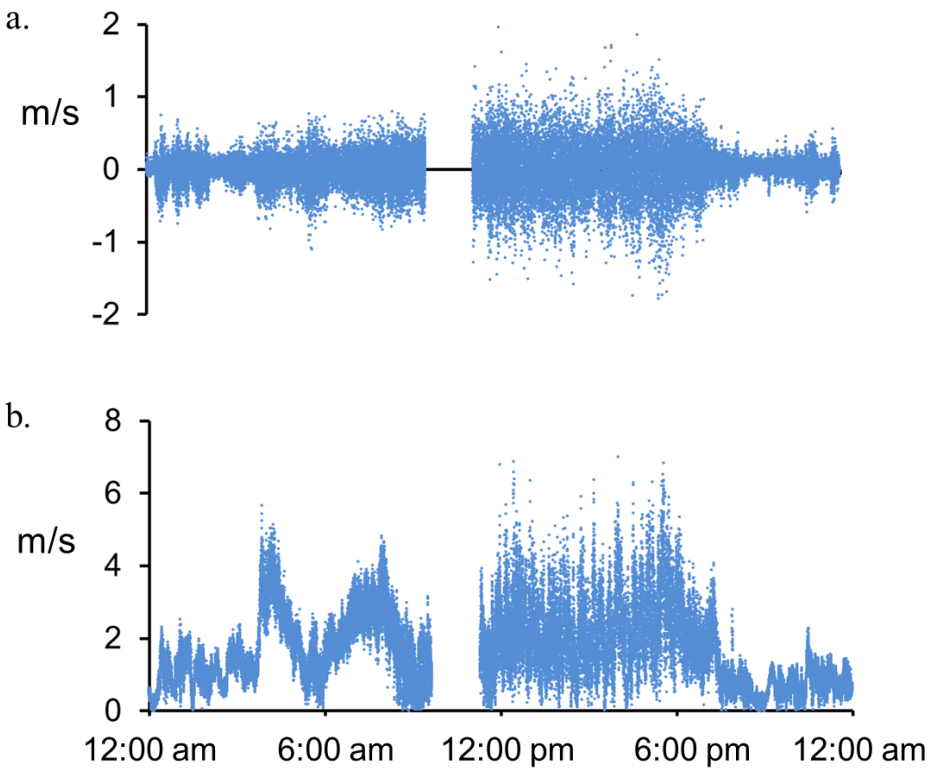

FIGURE 8.7. Diurnal variation of (*a*) vertical and (*b*) horizontal wind speed at z = 1 at the test site (June 4, 2014).

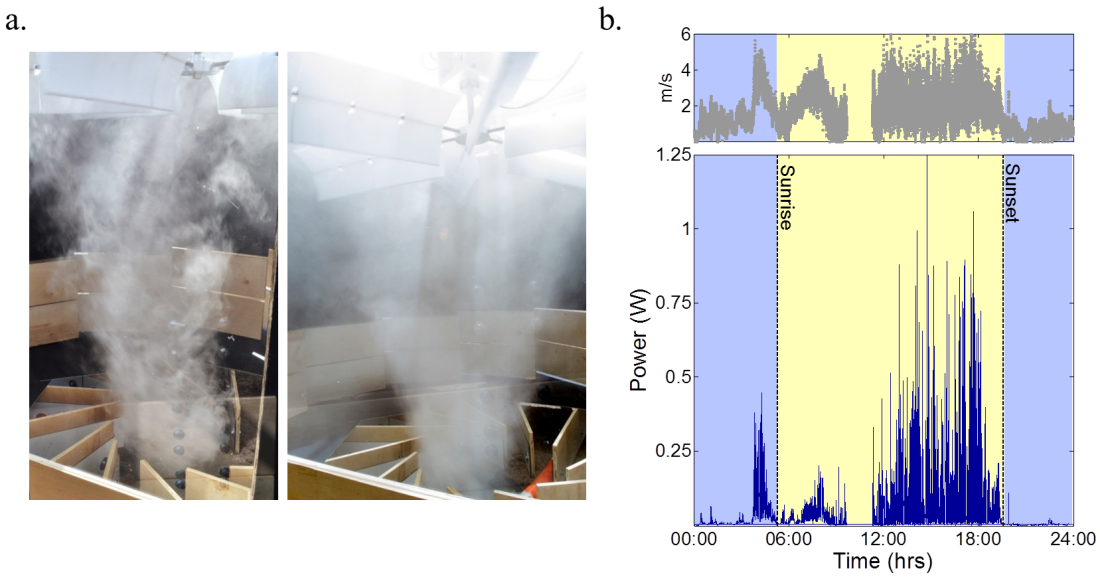

FIGURE 8.8. (*a*) Smoke visualization of the 2 m scale columnar vortex and (*b*) time history of ambient wind speed and power generation from the 2 m scale facility for a 24-hour period.

FIGURE 8.9. Smoke visualization of the D-1 6 m scale columnar vortex demonstrating formation of a buoyancy-induced vortex.

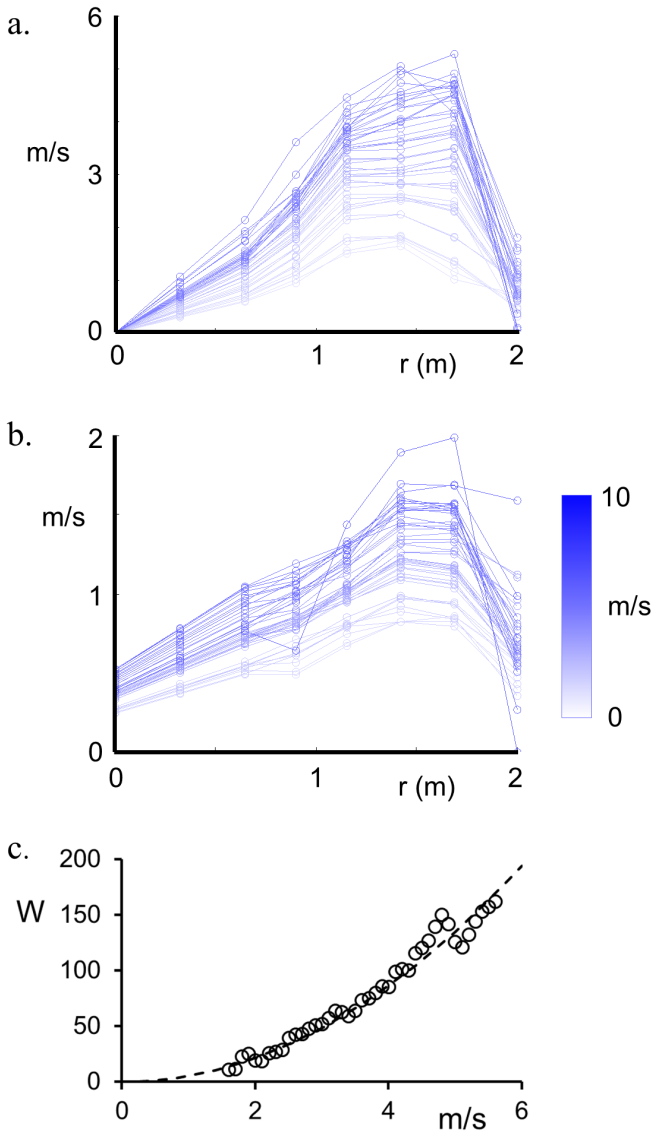

FIGURE 8.10. Time-averaged radial distributions of (*a*) tangential and (*b*) axial velocity binned by ambient wind speed in 0.1 m/s increments. Increasing color darkness corresponds to larger ambient wind speeds. (*c*) D-1 6 m scale mechanical power versus ambient wind speed.

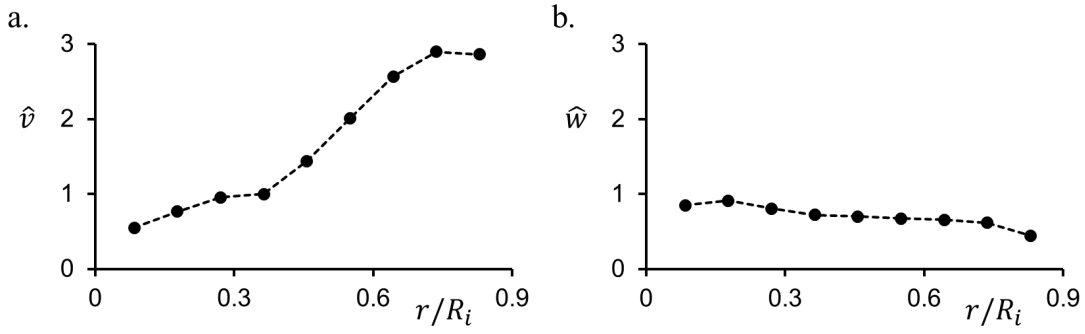

FIGURE 8.11. Time-averaged radial distributions of (*a*) tangential and (*b*) axial velocity for the D-2 6 m scale field facility.

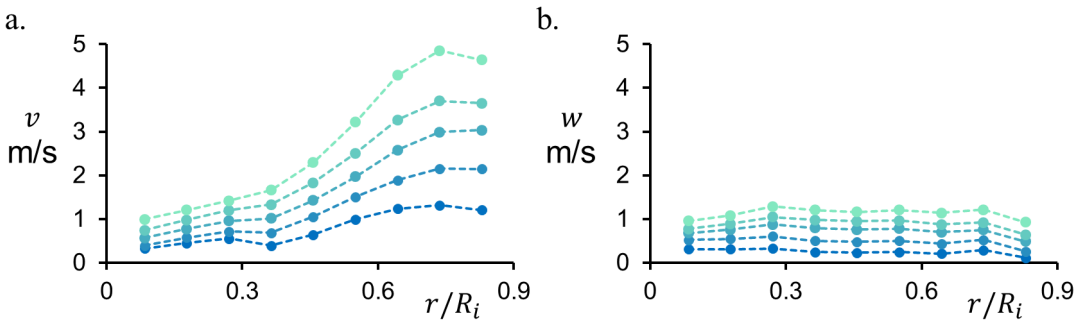

Figure 8.12. Time-averaged radial distributions of (*a*) tangential and (*b*) axial velocity in the D-2 6 m scale field facility for ambient wind speed of 1.2 (●), 2.4 (●), 3.6 (●), 4.8 (●), and 6 (●) m/s.

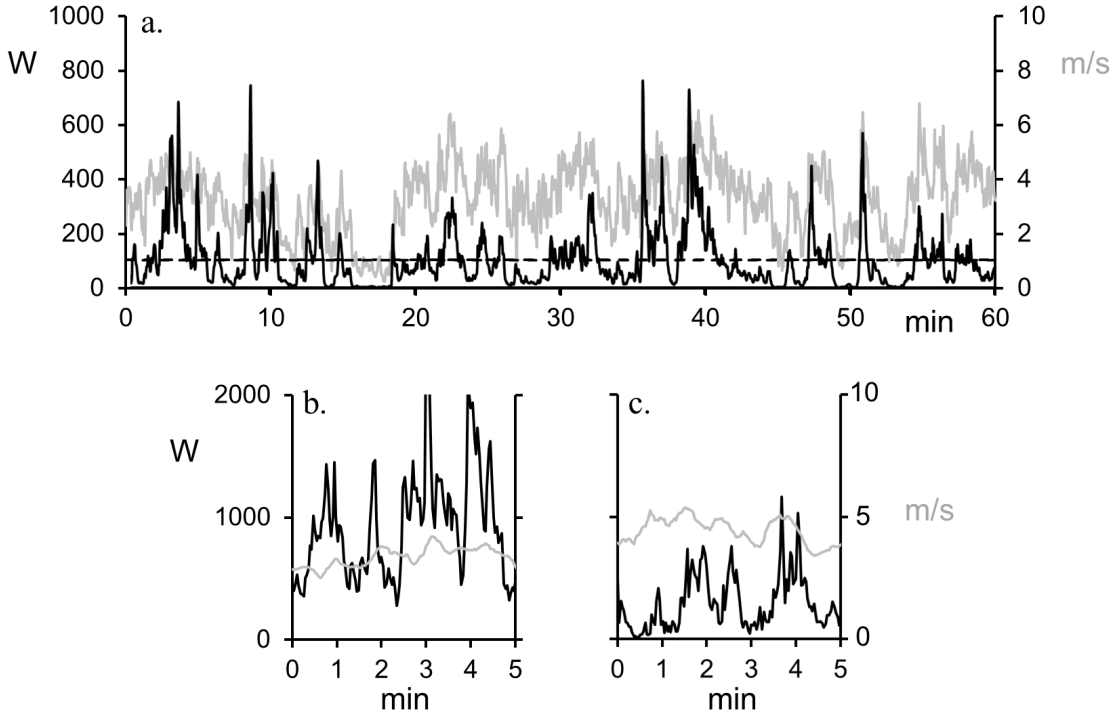

FIGURE 8.13. Time traces of integrated kinetic energy flux (—) for the D-2 6 m scale field facility and of the corresponding ambient wind speed (—).

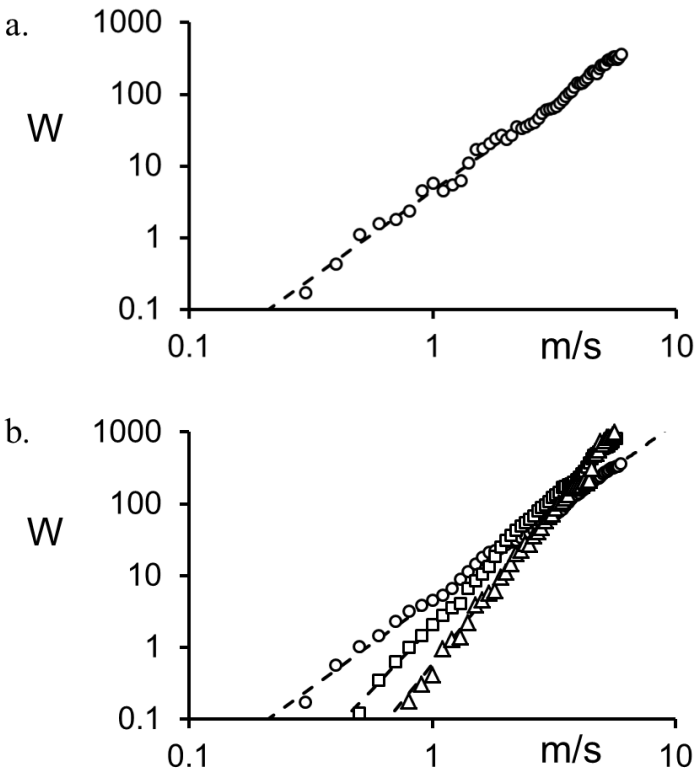

FIGURE 8.14. Variation of D-2 6 m scale field facility power generation with ambient wind speed for (*a*) $\varphi = 51°$ and (*b*) $\varphi = 51°$ (○), 42° (□), and 33° (Δ).

CHAPTER IX

CONCLUDING REMARKS

A variant of a free, naturally occurring buoyant columnar (dust devil) vortex within the unstably stratified air layers over solar-heated terrain, is deliberately triggered and anchored within an array of vertical, stator-like flow vanes with the potential to provide a thermomechanical link for harvesting low-grade waste heat. Laboratory experiments are designed to understand the formation and sustainment of the columnar vortex anchored within an open-top cylindrical enclosure over a heated ground-plane in isolation from the atmospheric environment of free dust devil vortices (albeit at a lower Grashof number). The cylindrical enclosure is bounded by an array of adjustable flow vanes that regulate the magnitude and direction of the flow that is radially entrained by the vortex. The entrained flow acquires tangential momentum as it passes through the vanes, and is heated from below at the ground-plane. The present investigations show that the three-dimensional flow field of the anchored, buoyancy-induced columnar vortex consists of three coupled domains, namely, a spiraling surface momentum boundary layer of ground-heated air, an inner thermally-driven vertical vortex core, and an outer annular flow that is bounded laterally by a helical shear layer and the vanes along its inner and outer edges, respectively, and by the spiraling boundary layer from below.

9.1 The Vortex Core and the Outer Annular Flow

The helical flow within the core of these vortices is characterized by the presence of two stagnation points along the axis of rotation, a primary stagnation point on the

surface and a secondary ("free") stagnation point aloft, where the rising updraft flow driven by surface-heated fluid diverges laterally. Depending on the formation parameters regulating entrainment into the vortex (the Grashof number *Gr* and the vane angle φ), its core can develop a single- or two-cell structure. The core structure is dominated by the balance between the axial pressure variation, affected by the radial pressure gradient of the rotating flow, and the buoyancy force. As shown by detailed SPIV measurements, the core of a single-cell vortex is characterized by helical, buoyancy-driven updraft flow along the vortex axis of rotation that persists from the primary stagnation point to the free stagnation point far above the near-surface flow, and is formed by the vertical turning of the radially-entrained boundary layer. The entrained flow in the outer domain above the spiraling boundary layer does not reach the vortex core, nor is it directly heated by the ground-plane. Rather, it is driven azimuthally through the vanes by the radial pressure gradient imposed by the vortex rotation, and axially by the buoyantly-driven updraft. When the entrainment angle imposed by the vanes and the resulting tangential momentum of the entrained flow are increased, a positive axial pressure gradient along the axis of rotation overcomes the buoyancy force, forming a central recirculating downdraft cell along the axis of rotation, and advecting cool air from aloft, resulting in a two-cell vortex structure. The downdraft cell is bounded from below and circumferentially by the buoyantly-driven updraft cell that affects its momentum and thermal energy. Its vertical elevation, as measured by the free stagnation point, can be regulated by the formation parameters. As the downdraft cell becomes attached to the ground-plane, a central, surface stagnation point is formed and the axial (upward) turning of the surface-heated boundary layer of the updraft cell is pushed radially outwards such

that a bifurcation circle centered about the axis of rotation is formed at the junction of the flow interface between the upward flows in the down- and updraft cells.

The cellular core structure is characterized over a range of formation parameters ($4.8 \cdot 10^7 < Gr < 11.6 \cdot 10^7$, $5^o < \varphi < 55^o$) by mapping the time-averaged axial velocity along the core centerline $w(z; r = 0)$ which is predominantly upward ($w > 0$) in a single-cell vortex, and reverses sign in the presence of the downdraft cell. For a fixed Gr, the depth of the downdraft cell increases with increasing φ which augments the angular momentum and horizontal swirl angle (v/u) of the entrained flow. Although the induced vortex intensifies with increasing Gr (for a given φ) as is evidenced by the magnitude of the up- or downdraft axial velocity and elevation of the free stagnation point, within the present range of Grashof numbers the change from single- to two-cell structure is primarily dominated by the vane angle, and it is shown that single-cell and attached two-cell vortices form for $\varphi \leq 30$ and $\varphi \geq 50°$, respectively. Radial distributions of axial and azimuthal velocity of single-cell and two-cell vortices demonstrate that downdraft along the vortex centerline leads to a radial spreading of the vortex core and reduction in the axial velocity throughout the enclosure. Radial temperature distributions show that the downdraft of cool air from aloft reduces the temperature at the centerline, shifting the radial temperature peak outwards along the flow interface between the cells.

The radial entrainment into either the single- or two-cell vortex is clearly coupled with the vortex-induced pressure field within the vane enclosure. The inner diameter and direction (and therefore azimuthal spacing) of the vanes set the strength and direction of the azimuthal jets that form between them and provide angular momentum to the vortex, and regulate the cyclostrophic balance between the radial pressure and centripetal forces.

This rotation-induced pressure force along the axis of the vortex is lowest near the surface where the tangential velocity has a maximum, and increases with elevation along the vortex centerline (*adverse* axial pressure gradient). The (positive) radial pressure gradient for a single-cell vortex increases monotonically with vane angle, because the increase in angular momentum augments the low pressure at the vortex centerline. This increase is accompanied by an increase in radial entrainment into, and volume flow rate through, the enclosure. However, the onset of the downdraft cell is accompanied by a significant increase in pressure along the centerline and, therefore, decreases the magnitude of the radial pressure gradient. While the downdraft cell progresses from detached to attached with increasing vane angle, these changes in pressure are coupled with a monotonic decrease in the entrained volume flow rate below the levels of the corresponding single-cell vortex (for the same Grashof number). The precipitous decrease in volume flow rate indicates that the potential amplification of the radial pressure gradient that would be associated with the increase in the tangential velocity is offset by the increase in the centerline pressure owing to the presence of the downdraft cell open to flow from aloft. Distributions of the integrated kinetic energy flux within the vortex column show that the bulk of the available power is contributed within the annular domain *outside* of the vortex core. It is remarkable that despite the decrease in volume flow rate with the appearance of the downdraft cell, the integrated kinetic energy flux of the vortex continues to increase with vane angle and ultimately saturates at higher angles. In fact, when the kinetic energy is normalized by the corresponding integrated flux of the gravitational potential energy through the cross-sectional area of the updraft flow (annular, in the presence of the downdraft cell), the integrated energy flux for both the

single- and two-cell vortices vary like $(\tan\varphi)^{1/3}$. Similarly, the regulation of entrainment does not alter the mechanisms of production and sustainment of axial vorticity within the vortex core. The present measurements show that regardless of the cellular structure of the vortex core, the axial circulation of the vortex column increases monotonically [like $(\tan\varphi)^{3/4}$] despite the reduction in entrainment and changes in axial vorticity distribution imposed by the downdraft cell.

9.2 Self-Similarity of the Vortex Column

Analysis of the flow field of the buoyant columnar vortex shows that well above the near-surface formation domain, the flow lends itself to a similarity formulation in which the rate of horizontal entrainment into the vortex core above the ground-plane boundary layer is linearly proportional (through the entrainment coefficient) to the local vertical velocity component, and the core diameter varies linearly with elevation. The dimensionless axial momentum equation depends on two parameters namely, the swirl number (ratio of tangential and axial velocity components), and a modified Froude number (ratio of the axial kinetic energy and the buoyant potential energy). While the flow enclosure that anchors the vortex clearly imposes a global length scale on its evolution, the present investigations show that two stable limits of the vortex structure namely, single- and attached two-cell vortices, are self-similar with only weak dependence on the global scale.

Similarity analysis of the velocity field demonstrates that the measured primary variables of the swirl and Froude numbers, namely, the buoyancy weight function (g'), and the tangential (v) and axial (w) velocity components are nearly spatially self-similar. This finding enables determination of the experimentally-determined functional

dependence of the single-cell vortex on the similarity variables within the cylindrical domain $\eta < 4.5$. It is shown that the nominal buoyant columnar vortex entrains *less* cool ambient fluid along its periphery above the ground-plane than a nonrotating, thermal plume, and, as a result, the centerline weight deficiency (as measured by the air temperature) decreases at a lower axial rate $g' \propto z^{-1/4}$ than in a nonrotating thermal plume ($g' \propto z^{-1/3}$). The peak tangential velocity at $\eta = 1$ decreases linearly with elevation at a rate similar to that for nonbuoyant swirling jets having similar swirl numbers, and its functional dependence on the similarity coordinates follows that for the Lamb-Oseen 2-D viscous vortex model. Owing to the nonzero weight deficiency within the vortex core, the axial flow continues to accelerate well above the near-surface (development) region, although at a lower rate than in a nonrotating thermal plume as a result of the rotation-induced adverse axial pressure gradient (e.g., at $\eta = 1$, w increases like $z^{1/4}$ in the vortex and like $z^{1/3}$ in the plume). This axial acceleration is in contrast to the decay of the axial velocity in nonbuoyant swirling jets ($w \propto z^{-1}$).

The similarity analysis is extended to single- and attached two-cell vortices over a range of the formation parameters. First, it is shown that for a given vane angle, radial variations of the swirl and Froude numbers are invariant with *Gr*, and both increase with vane angle when a single-cell structure is maintained. The radial distributions and magnitudes of the swirl and Froude numbers exhibit several significant differences in the presence of downdraft. The swirl number has a singularity between the downward and upward axial flows in the downdraft cell, and is larger in the two-cell vortex due to the decrease in axial velocity resulting from reversed axial flow. The Froude number is smaller in the two-cell vortex owing to the decrease in axial momentum and increase in

thermal energy, and vanishes at the interface between the downward and upward axial flows. When radial distributions of the time- and azimuthally-averaged tangential and axial velocity components and the weight deficiency (of the single-cell and attached two-cell vortex) are normalized by their respective maxima, the distributions of each collapse to form a single, self-similar distribution for each cellular structure (similarity is not maintained over the different cellular structures). It is reasonable to assume that for the case of the detatched two-cell vortex, the self-similar distributions of the two- and single-cell vortex would also describe the flow field above and below the free stagnation point, respectively. It is noteworthy that while the Grashof number controls the elevation of the free stagnation point for the detached two-cell vortex, once a stable attached recirculating domain is established, the evolution of the attached two-cell vortex becomes self-similar with respect to *Gr*, and that because of the global scale imposed by the diameter of the enclosure, the similarity is not affected by the significant changes in the radial scale.

9.3 Near-Surface Flow and Vorticity Dynamics

The flow within the vortex core is primarily driven by the relatively thin [$z/h \approx O(0.03)$] boundary layer of ground-heated air that is forced to swirl within the enclosure. It is the interaction of this boundary layer with the buoyantly unstable flow near the centerline of the vortex that leads to the conversion of thermal energy of the surface-heated air into mechanical (kinetic) energy within the inner and outer flow of the vortex column. The present investigation shows that as the flow over the heated surface approaches the centerline, it is accelerated by the vortex-induced radial pressure gradient and the cross stream swirl (radial and tangential) velocity distribution becomes

reminiscent of a wall jet with a distinct peak in the radial velocity. In the case of the single-cell vortex, a central, surface stagnation domain dominates the near-surface flow in the vicinity of the centerline, and forces vertical (axial) turning of the swirling flow, and, as a result, an increase in the axial velocity component as the flow spirals upward into the core of the vortex. In the case of the attached two-cell vortex, axial downdraft along the vortex centerline terminates at an attached central stagnation point on the ground-plane. The downdraft turns axially upward within the outer segment of the recirculating cell, and the interface between the recirculating downdraft and updraft cells forms a circular stagnation line or bifurcation circle. The upward-turning downdraft forms a helical jet-like flow bounded on its inner radial surface by the downward flow along the vortex axis and on the outside radial surface by the upward-turning buoyancy-driven updraft cell. Perhaps the most prominent feature of the near-surface flow field of either cellular structure is the formation of a converging-diverging flow tube with a contraction-like throat that leads to a significant increase in the magnitude of the axial velocity component within the updraft cell. This streamtube is bounded radially by the outer flow and is marked by a surface on which the time-average radial velocity component (and hence entrainment) vanishes. The flow of surface-heated air into the vortex column is accompanied by an increase in the temperature of the air within the updraft cell above the surface, intensifying the buoyancy in this domain, and thereby contributing to an increase in the magnitude of the axial velocity.

The formation and sustainment of the buoyancy-induced columnar vortex are associated with the production, and eventual tilting, of spiraling horizontal (azimuthal and radial) vorticity concentrations that are induced within the swirling boundary layer by

the combination of the rotating outer flow above the surface, and by radial entrainment. The present measurements show that spiraling vortex lines within the boundary layer are advected towards the base of the vortex column, and are tilted by radial gradients of the buoyancy-driven axial velocity in the vortex contraction to form axial vorticity within the vortex core. This mechanism is absent in nonrotating plumes, where azimuthal vortex lines form closed circuits about the axis of symmetry. Once tilted axially, the vortex lines expand radially outward above the vortex contraction, and ultimately form a helical pattern as the vortex flow becomes nearly self-similar. In common with a single-cell vortex, axial vorticity within the updraft cell of the two-cell vortex originates from the vertical tilting of near-surface radial vorticity within the swirling momentum boundary layer. Vortex lines spiral helically, and the axial vorticity is stretched by the buoyantly-accelerating flow and tilted radially and azimuthally by axial gradients of the radial and tangential velocity components, respectively, as the vortex core spreads radially with elevation. These effects are intensified significantly with the increased radial spreading affected by the axial migration of the downdraft cell. As the irrotational fluid within the downdraft cell is drawn from aloft, rotation is affected by azimuthal shear with the surrounding updraft cell, and axial vorticity diffuses radially into the recirculating flow domain. Distributions of the axial circulation demonstrate the transition from low to high aspect ratio (axial to radial) cylindrical domains that bound the horizontal vorticity concentrations within the surface boundary layer, and bound the axial vorticity concentrations within the core of the vortex that mark the change from the cross stream scale of the boundary layer to the scale of the core of the vortex. Furthermore, it is shown that the circulation of the radial vorticity measured by the flux

through a cylindrical shell that is centered on the vortex centerline and intersects the surface boundary layer, is equal to the circulation of the axial vorticity within the vortex core, thus confirming that only the radial vorticity component contributes to the formation of axial vorticity within the core of the columnar vortex. Therefore, the production and ultimate tilting of radial vorticity within the swirling boundary layer determines the strength of the columnar vortex regardless of cellular structure, and the formation mechanism does not rely on the presence of ambient axial vorticity or ambient horizontal wind shear as suggested previously. This mechanism enables the columnar vortex to be sustained and regulated as long as the buoyant instability is present. For the single-cell vortex, the variation of the integrated kinetic energy flux with elevation demonstrates that nearly 60% of the measured kinetic energy flux at the top of the enclosure is generated between the heated surface and the top of the vortex contraction during the tilting process of vorticity concentrations within the spiraling boundary layer. This indicates that enhancement of the available kinetic energy can be achieved through augmentation of the near-surface production and tilting of vorticity concentrations.

9.4 Redistribution of Vorticity for Mechanical Enhancement of a Columnar Vortex

Vorticity distribution and transport within the ground-plane boundary layer of the columnar vortex are deliberately manipulated using a low-profile azimuthal array of vertical flat-plate vanes which alter the direction of the boundary layer flow with the goal of optimizing the mechanical properties of the vortex (e.g., kinetic energy flux). The lower-tier vanes redirect and effectively shorten the spiraling trajectory of the entrained flow along the surface, reducing the losses and pressure drop associated with the upper-tier vane array. In the presence of the lower-tier vanes, the radial distribution of axial

velocity indicates that alterations to the entrained flow lead to the detachment of the downdraft cell of the attached two-cell baseline vortex and an upward migration of the free stagnation point along the axis of rotation thereby inducing a 150% increase in the available mechanical power for the *same Gr*. The substantial increase in radial entrainment into the enclosure is induced by the enhancement of the ensuing vortex flow and induced radial pressure gradient at higher elevations manifested by the redirection of the spiraling flow within the surface boundary layer. Perhaps the most salient effect of the hybrid vanes is the redistribution of the axial vorticity to a central concentration within a high intensity core that is surrounded by an annular domain of lower magnitude concentrations. The formation of these two distinct vorticity concentrations indicates that the lower-tier vanes lead to intensification of the radial vorticity within the segmented surface boundary layer, and augment its axial tilting outside of the primary core of the columnar vortex. Despite this redistribution, the net axial circulation for the baseline and hybrid geometries is *nearly identical* and, therefore, for given a given Grashof number the core Reynolds number in the presence of the hybrid vanes is determined by the geometry of the upper-tier vanes.

The changes in vorticity concentrations are brought about by the formation of a streamwise-helical flow formed by the interaction between two air layers that move with different speeds in different directions as they are entrained nominally tangentially and radially between adjacent upper- and lower-tier vanes to form a shear layer. A longitudinal vortex is formed within the converging channel by the lower-tier vanes before it is tilted upward, advected into the bulk rotating flow, and becomes helically wound about the primary vortex column. Despite the substantial increase in the

mechanical energy, the invariance of the total axial circulation implies that it is the redistribution of axial vorticity that ultimately strengthens the anchored vortex, as the helical secondary vortices advect mass and momentum upwards into the annulus between the vortex core and outer flow. Control over the radial extent and position of the annular domain of axial vorticity, and therefore the mechanical properties of the vortex, are affected by modification of the lower-tier vane geometry. While the global axial circulation remains invariant and is set by the geometry of the upper-tier, the distribution and balance of the vorticity concentrations are manipulated through adjustments to the lower-tier angle and height, respectively. This geometry can be used to optimize the mechanical and structural properties of the vortical flow for the efficient extraction of kinetic energy from the induced flow field.

9.5 Field Testing

The thermomechanical link between heat in the ground-heated air, and the flow field of an anchored vortex, was explored for the production of electric power in the natural environment during expeditions to the Arizona desert. Two facilities having 2 and 6 m diameter structure were tested, with the objectives of initiating an anchored, buoyancy-induced columnar vortex and coupling it to a vertical-axis turbine, and investigating the effects of ambient wind on the formation and mechanical characteristics of the formed columnar vortex.

In the first outdoor field test, an anchored vortex column having a nominal diameter of 0.4 m was successfully initiated, maintained, and directly coupled to a spinning rotor in a 2 m facility. The facility was operated and monitored continuously for nearly 24 hours, and the extracted power followed the sun with peak power production

(greater than 1 W) during the afternoon hours. The vortex was formed in the absence and presence of cross-winds or gusts, and daytime power was clearly characterized by strong vortex intensification due to entrainment of heated ambient air. The significant increase in extractable power between day ($\bar{\dot{E}}$ = 173 mW) and night ($\bar{\dot{E}}$ = 25 mW) was clearly due to buoyancy-driven flow induced by the anchored, columnar vortex.

Two vane designs (D-1 and D-2) were tested using a 6-m scale field facility to investigate the coupling of the enclosure and the induced vortex to the ambient wind field. Each design was equiped with a 2 m high contraction cone to mitigate interference of cross-flow ambient wind over the facility with the anchored vortex flow within the enclosure. Field tests of D-1 (6 m scale enclosure, without a rotor) were conducted using flexible vanes that provided the ability to adjust their curvature. A vortex column having a nominal inner diameter of 1.2 m was successfully initiated, maintained, and visualized. The vortex extended through the array of upper- and lower-tier vanes and was significantly enchanced by entrainment of ambient air. The flow field of the vortex within the enclosure was characterized by using a radial array of vane anemometers to measure distributions of the tangential and axial velocity. Similar to natural dust devils, the magnitudes of the azimuthal and tangental velocity components within the enclosure increase signfinicantly with wind speed. It was demonstrated that the mechanical power within the enclosure scales approximately with the square of the ambient wind speed. A peak power of 180 W was realized.

Field tests of a redesigned D-2 enclosure (without a rotor) were conducted to investigate the effect of frontal area and interactions with ambient wind, utilizing vanes protruding *outward* from the enclosure to increase the inlet area into the facility. Due to

the substantial increase in frontal area, the magnitudes of the tangential and axial velocity components and of the volume flow rate through the facility increased significantly with the speed of the ambient wind. The power production averaged over one hour increased to 107 W with peak power of 784 W. Shorter time-samples (e.g., 5 minutes) produced mean power of up to 1 kW. These data show that the fluctuations of mechanical power did not closely follow changes in ambient wind speed. Ambient wind clearly contributes to strengthening the anchored columnar vortex, as for naturally-occurring dust devils. In addition to the significant improvement in extractable mechanical power in these prototype enclosures, the present investigations clearly demonstrated the role of the ambient wind field in the formation of energetic columnar vortices. These investigations have also led to improved understanding of the role of vane design in optimizing the interactions between the enclosed vortex and local wind currents. These insights will be further implemented in the next field tests in summer 2016.

APPENDIX A

INTEGRAL FORM OF THE AXIAL MOMENTUM EQUATION

The axial momentum equation (2.3) [cf. Chapter 2] for a free axisymmetric swirling jet that describes the vertical flow near the centerline and sufficiently far from the ground-plane can be rewritten following the formulation of Rajaratnam (1976). The flow domain is described using cylindrical coordinates (r, θ, z) such that the z-axis coincides with the centerline of the columnar vortex, and the corresponding velocity field is denoted by (u, v, w).

After multiplying through by ρr, equation (2.3) is integrated with respect to r to produce

$$\int_0^\infty \rho u \frac{\partial w}{\partial r} r dr + \int_0^\infty \rho w \frac{\partial w}{\partial z} r dr = -\int_0^\infty \frac{\partial p}{\partial z} r dr + \int_0^\infty \rho g' r dr + \int_0^\infty \frac{\partial (r\tau_{rz})}{\partial r} dr. \quad \text{(A.1)}$$

Using the boundary conditions $\tau_{rz}(r \to \infty, z) = 0$ and $\tau_{rz}(0, z)$ is finite, the final term in equation (A.1) is equivalent to zero, $\int_0^\infty \frac{\partial (r\tau_{rz})}{\partial r} dr = |r\tau_{rz}|_0^\infty = 0$. Rewriting the integrand of the second integral $[w\, \partial w/\partial z = \partial(\frac{1}{2}w^2)/\partial z]$ equation (A.1) becomes

$$\int_0^\infty \rho u \frac{\partial w}{\partial r} r dr + \int_0^\infty \rho \frac{1}{2} \frac{\partial w^2}{\partial z} r dr + \int_0^\infty \frac{\partial p}{\partial z} r dr = \int_0^\infty \rho g' r dr. \quad \text{(A.2)}$$

The first integral can be recast under the assumptions that the radial entrainment decays to zero at infinity $[u(r \to \infty, z) = 0]$ and the radial velocity is equivalent to zero along the centerline $[u(0, z) = 0]$:

$$\int_0^\infty \rho u \frac{\partial w}{\partial r} r dr = |\rho u w r|_0^\infty - \int_0^\infty \rho w \frac{\partial (ru)}{\partial r} dr = -\int_0^\infty \rho w \frac{\partial (ru)}{\partial r} dr. \quad \text{(A.3)}$$

Substituting the continuity equation, $\partial(ru)/\partial r = -\partial(rw)/\partial z$ [cf. equation (2.1)], into equation (A.3), equation (A.2) is rewritten as:

$$\int_0^\infty \rho w \frac{\partial(rw)}{\partial z} dr + \int_0^\infty \rho \frac{1}{2} \frac{\partial w^2}{\partial z} r dr + \int_0^\infty \frac{\partial p}{\partial z} r dr$$

$$= \int_0^\infty \rho \frac{1}{2} \frac{\partial w^2}{\partial z} r dr + \int_0^\infty \rho \frac{1}{2} \frac{\partial w^2}{\partial z} r dr + \int_0^\infty \frac{\partial p}{\partial z} r dr$$

$$= \int_0^\infty \rho \frac{\partial w^2}{\partial z} r dr + \int_0^\infty \frac{\partial p}{\partial z} r dr = \int_0^\infty \rho g' r dr. \quad \text{(A.4)}$$

The right hand side of the equation (A.4) is reorganized such that the derivative is applied before the integration, noting that integral and differential operators are linear and commute. Therefore, (A.4) is rewritten in the form of equation (2.4):

$$\frac{d}{dz} \int_0^\infty (\rho w^2 + p) r dr = \int_0^\infty \rho g' r dr.$$

REFERENCES

ADRIAN, R. J. & WESTERWEEL, J. 2011 Particle Image Velocimetry. *Cambridge University Press.*

BAKER, G. L. 1981 Boundary Layers in Laminar Vortex Flows. *Ph.D. Thesis*, Purdue University.

BARCILON, A. 1967a A Theoretical and Experimental Model for a Dust Devil. *J. Atmo. Sci.*, **24**, 453-466.

BARCILON, A. 1967b Vortex Decay Above a Stationary Boundary. *J. Fluid Mech.*, **27**, 155-175.

BATCHELOR, G. K. 1954 Heat Convection and Buoyancy Effects in Fluids. *Q. J. R. Met. Soc.*, **80**, 339-358.

BELLAMY-KNIGHTS, P. G. 1970 An Unsteady Two-Cell Vortex Solution of the Navier-Stokes Equations. *J. Fluid Mech.*, **41**, 673-687.

BLUESTEIN, H. B., WEISS, C. C. & PAZMAY, A. L. 2004 Doppler Radar Observations of Dust Devils in Texas. *Monthly Weather Rev.*, **132**, 209-224.

BODE, L., LESLIE, L. M. & SMITH, R. K. 1975 A Numerical Study of Boundary Effects on Concentrated Vortices with Application to Tornadoes and Waterspouts. *Q. J. R. Met. Soc.*, **101**, 313-324.

BODE, L & SMITH, R. K. 1975 A Parameterization of the Boundary Layer of a Tropical Cyclone. *Boundary-Layer Meteorology*, **8**, 3-19.

BRADY, R. H. & SZOKE, E. J. 1989 A Case Study of Nonmesocyclone Tornado Development in Northeast Colorado: Similarities to Waterspout Formation. *Monthly Weather Rev.*, **117**, 843-856.

BRANDES, E. A. 1978 Mesocyclone Evolution and Tornadogenesis: Some Observations. *Monthly Weather Rev.,* **106**, 995-1011.

CALLUAUD, D. & DAVID, L. 2004 Stereoscopic Particle Image Velocimetry Measurements on the Flow around a Surface-Mounted Block. *Experiments in Fluids*, **36**, 53-61.

CARRIER, G.F., HAMMOND, A. L. & GEORGE, O. D. 1971 A Model of the Mature Hurricane. *J. Fluid Mech*. **47**, 145-170.

CARROLL, J. J. & RYAN, J. A. 1970 Atmospheric Vorticity and Dust Devil Rotation. *J. Geophys. Res.,* **20**, 5179-5184.

CERMAK, J. E. and ARYA, S. P. S. 1970 Problems of Atmospheric Shear Flows and Their Laboratory Simulation. *Boundary-Layer Meteor*. **1**, 40-60.

CHIGIER, N. A. & CHERVINSKY, A. 1967 Experimental Investigation of Swirling Vortex Motion in Jets. *J. Appl. Mech.*, 443-451.

CHURCH, C R., SNOW, J. T. & AGEE, E. M. 1977 Tornado Vortex Simulation at Purdue Universtiy. *Bull. Am. Met. Soc.*, **58**, 900-908.

CHURCH, C. R., SNOW, J. T., BAKER, G. L. & AGEE, E. M. 1979 Characteristics of Tornado-like Vortices as a Function of Swirl Ratio: A Laboratory Investigation. *J. Atmos. Sci.*, **36**, 1755-1776.

DAVIES-JONES, R. P. 1973 The Dependence of Core Radius on Swirl Ratio in a Tornado Simulator. *J. Atmos. Sci.*, **30**, 1427-1430.

DESSENS, J. 1972 Influence of Ground Roughness on Tornadoes: A Laboratory Simulation. *J. Appl. Meteor.*, **11**, 72-75.

FIEDLER, B. H. & ROTUNNO, R. 1986 A Theory for the Maximum Windspeeds in Tornado-Like Vortices. *J. Atmos. Sci.*, **43**, 2328-2340.

FIEDLER, B. H. 1998 Wind-speed Limits in Numerically Simulated Tornadoes with Suction Vortices. *Q. J. R. Met. Soc.*, **124**, 2377-2392.

FITZJARRALD, D. E. 1973a A Field Investigation of Dust Devils. *J. Appl. Meteor.,* **12**, 808–813.

FITZJARRALD, D. E. 1973b A Laboratory Simulation of Convective Vortices. *J. Atmos. Sci.* **30**, 894-902.

GAYA, M., HOMAR, V., ROMERO, R. & RAMIS, C. 2001 Tornadoes and Waterspouts in the Balearic Islands: Phenomena and Environment Characterization. *Atmospheric Research*, **56**, 253-267.

GLEZER, A. & SIMPSON, M. 2014 Power Generation Using Buoyancy-Induced Vortices. *U.S. Patent 8,875,509*.

GREELY, R., BALME, M. R., IVERSEN, J. D., METZGER, S., MICKELSON, R., PHOREMAN, J. & WHITE, B. 2003 Martian Dust Devils: Laboratory Simulations of Particle Threshold. *J. Geophys. Res.*, **108**, 7-1-7-12.

HALLER, G. 2005 An Objective Definition of a Vortex. *J. Fluid Mech.*, **525**, 1-26.

HARLOW, F. H. & STEIN, L. R. 1974 Structural Analysis of Tornado-Like Vortices. *J. Atmos. Sci.*, **31**, 2081-2098.

HESS, G. D. & SPILLANE, K. T. 1990 Characteristics of Dust Devils in Australia. *J. App. Met.,* **29**, 498-507.

HESS, G. D., SPILLANE, K. T. & LOURENSZ, R. S. 1988 Atmospheric Vortices in Shallow Convection. *J. Appl. Meteor.*, **27**, 305-317.

HOLTON, J. R. 2004 An Introduction to Dynamic Meteorology Fourth Addition. *Elsevier Academic Press*.

HONOHAN, A. M. 2003 The Interaction of Synthetic Jets with Cross Flow and Modification of Aerodynamic Surfaces. *Ph.D. Thesis*, Georgia Institute of Technology.

HOWELLS, P. & SMITH, R. K. 1983a Numerical Simulations of Tornado-like Vortices. Part I: Vortex Evolution. *Geo. & Astro. Fluids*, **27**, 253-284.

HOWELLS, P. & SMITH, R. K. 1983b Numerical Simulations of Tornado-like Vortices. Part II: Two-Cell Vortices. *Geo. & Astro. Fluids*, **27**, 285-298.

JACOBS, E.W. & LASIER, D. D. 1984 Theoretical Analysis of Solar-Driven Natural Convection Energy Conversion Systems. SERI/TR-211-1950. Solar Energy Research Inst., Golden, CO.

JEONG, J. & HUSSAIN, F. 1995 On the Identification of a Vortex. *J. Fluid Mech.*, **285**, 69-94.

KAIMAL, J. C. & BUSIGNER, J. A. 1970 Case Studies of a Convective Plume and a Dust Devil. *J. Appl. Meteor.,* **9**, 612-620.

KANAK, K. M., LILLY, D. K. & SNOW, J. T. 2000 The Formation of Vertical Vortices in the Convective Boundary Layer. *Q. J. R. Met. Soc.*, **126**, 2789-2810.

KANAK, K. M. 2005 Numerical Simulation of Dust Devil-Scale Vortices. *Q. J. R. Met. Soc.*, **131**, 1271-1292.

KARSTENS, C.D., SAMARAS, T.M., LEE, B.D., GALLUS JR., W.A. & FINLEY, C.A. 2010 Near-Ground Pressure and Wind Measurements in Tornados. *Mon. Wea. Rev.*, **138**, 2570-2588.

KAYS, W.M., CRAWFORD, M.E. & WEIGAND, B. 2005 Convective Heat and Mass Transfer 4th Edition. *McGraw Hill*.

KENDALL, W. M. 1978 Unsteady Two-Cell Similarity Solution to a Convective Atmospheric Vortex Model. *Tellus*, **30**, 376-382.

KUO, H. L. 1966 On the Dynamics of Convective Atmospheric Vortices. *J. Atmos. Sci.*, **23**, 25-42.

KURGANSKY, M.V. 2006 Size Distribution of Dust Devils in the Atmosphere. *Atmos. Ocean Phys.*, **42**, 319-325.

KURGANSKY, M. V., MONTECINOS, A., VILLAGRAN, V., & METZGER, S. M. 2011 Micrometeorological Conditions for Dust-Devil Occurrence in Atacama Desert. *Boundary-Layer Meteor.*, **138**, 285-298.

LAMB, H. 1945 Hydrodynamics. *Cambridge University Press*.

LIU, X. & KATZ, J. 2006 Instantaneous Pressure and Material Acceleration Measurements using a Four-Exposure PIV System. *Exp. Fluids*, **41**, 227-240.

LOGAN, S. E. 1971 An Approach to the Dust Devil Vortex. *AIAA Journal*, **9**, 660-665.

LORENZ, R. D. 2009 Power Law of Dust Devil Diameters on Mars and Earth. *Icarus*, **203**, 683-684.

LUCIER, R. E. 1981 System for Converting Solar Heat to Electrical Energy. *U.S. Patent 4275309*.

LUGT, H. J. 1989 Vortex Breakdown in Atmospheric Columnar Vortices. *Bull. Am. Met. Soc.*, **70**, 1526-1537.

MATTSON, J. O., NIHLEN, T. & WANG, Y. 1993 Observations of Dust Devils in a Semi-arid District of Southern Tunisa. *Weather*, **48**, 359-363.

MAXWORTHY, T. 1972 On the Structure of Concentrated, Columnar Vortices. *Astronaut. Acta*, **17**, 363-374.

MAXWORTHY, T. 1973 A Vorticity Source for Large-Scale Dust Devils and Other Comments on Naturally Occurring Columnar Vortices. *J. Atm. Sci.,* **30**, 1717-1722.

MAXWORTHY, T. 1981 The Laboratory Modelling of Atmospheric Vortices: A Critical Review. *Springer*.

MAXWORTHY, T., HOPFINGER, E. J., & REDEKOPP, L. G. 1985 Wave Motions on Vortex Cores. *J. Fluid Mech.*, **151**, 141-163.

METZGER, S. M. 1999 Dust Devils as Aeolian Transport Mechanisms in Southern Nevada and the Mars Pathfinder Landing Site. *Ph.D. thesis*, Univ. of Nev., Reno.

MICHAUD, L.M. 1999 Vortex Process for Capturing Mechanical Energy During Upward Heat-Convection in the Atmosphere. *Appl. Energy,* **62**, 241-251.

MORTON, B. R. 1966 Geophysical Vortices. *Prog. Aeronaut. Sci*., **7**, 145-194.

MORTON, B. R., TAYLOR, G. I. & TURNER, J. S. 1956 Turbulent Gravitational Convection from Maintained and Instantaneous Sources *Pro. Roy. Soc. London. Series A*, **234**, 1-23.

MULLEN, J. B. & MAXWORTHY, T. 1977 A Laboratory Model of Dust Devil Vortices. *Dyn. Atmos. Oceans,* **1**, 181-214.

NEAKRASE, L. D. V. & GREELY, R. 2010 Dust Devils in the Laboratory: Effect of Surface Roughness on Vortex Dynamics. *J. Geophys. Res.*, **115**, E05003.

NIINO, H., NAKANISHI, M. & TANAKA, R. 2006 On the Conditions for a Dust Devil Genesis in a Large Eddy Simulation. *Fourth Int. Symp. Comp. Wind Eng.*

NOLAN, D. S. & FARREL, B. F. 1999 The Structure and Dynamics of Tornado-Like Vortices. *J. Atmos. Sci.*, **56**, 2908-2936.

OHNO, H. & TAKEMI, T. 2010 Mechanisms for Intensification and Maintence of Numerically Simulated Dust Devils. *Atmos. Sci. Let.*, **11**, 27-32.

OKE, A. M. C., TAPPER, N. J. & DUNKERLEY, D. 2007 Willy-Willies in the Australian Landscape: The Role of Key Meteorological Variables and Surface Conditions in Defining Frequency and Spatial Characteristics. *J. Arid. Env.*, **71**, 201-215.

PATHARE, A. V., BALME, M. R., MEZTGER, S. M., SPIGA, A., TOWNER, M. C. & RENNO, N.O. 2010 Assessing the Power Law Hypothesis for the Size—Frequency Distribution of Terrestrial and Martian Dust Devils. *Icarus*, **209**, 851-853.

PERRY, A.E. & CHONG, M.S. 1987 A Description of Eddying Motions and Flow Patterns Using Critical-Point Concepts. *Ann. Rev. Fluid Mech.*, **19**, 125-155.

RAJARATNAM, N. 1976 Developments in Water Science 5: Turbulent Jets. *Elsevier Scientific Publishing Company*.

RENNO, N. O., BURKETT, M. L. & LARKIN, M. P. 1998 A Simple Thermodynamical Theory for Dust Devils. *J. Atmos. Sci.,* **55**, 3244-3252.

RENNO, N. O. & BLUESTEIN, H. B. 2001 A Simple Theory for Waterspouts. *J. Atmos. Sci.*, **58**, 927-932.

RENNO, N. O., ABREU, V. J., KOCH, J., SMITH, P.H., HARTOGENSIS, O.K., DE BRUIN, H.A.R., BUROSE, D., DELORY, G.T., FARRELL, W.M., WATTS, C.J., GARATUZZA, J., PARKER, M. & CARSWELL, A. 2004 MATADOR 2002: A Pilot Field Experiment on Convective Plumes and Dust Devils. *J. Geophys. Res.,* **109**, E07001.

RENNO, N. O. 2008 A Thermodynamically General Theory for Convective Vortices. *Tellus*, **60A**, 688-699.

ROTUNNO, R. 1980 Vorticity Dynamics of a Convective Swirling Boundary Layer. *J. Fluid Mech.*, **97**, 623-640.

ROTUNNO, R. 2013 The Fluid Dynamics of Tornadoes. *Annu. Rev. Fluid Mech.*, **45**, 59-84.

RYAN, J. A. 1972 Relation of Dust Devil Frequency and Diameter to Atmospheric Temperature. *J. Geophys. Res.*, **77**, 7133-7137.

SAFFMAN, P.G. 1992 Vortex Dynamics. *Cambridge University Press*.

SINCLAIR, P. C. 1969 General Characteristics of Dust Devils. *J. App. Meteor*., **8**, 32-45.

SINCLAIR, P. C. 1973 The Lower Structure of Dust Devils. *J. Atm. Sci.,* **30**, 1599-1619.

SMITH, R. K. & LESLIE, L. M. 1976 Thermally Driven Vortices: A Numerical Study with Application to Dust-Devil Dynamics. *Quart. J. R. Met. Soc.*, **102**, 791-804.

SNOW. J. T. 1982 A Review of Recent Advances in Tornado Vortex Dynamics. *Rev. of Geophys. Space Phys.*, **20**, 953-964.

TAYLOR, G. I. 1945 Dynamics of a Mass of Hot Gas Rising in Air. *U.S. Atomic Energy Commission MDDC 919. LADC* 276.

TURNER, J. S. 1962 The 'Starting Plume' in Neutral Surroundings. *J. Fluid Mech.*, **13**, 356-368.

TURNER, J. S. 1969 Buoyant Plumes and Thermals. *Ann. Rev. Fluid Mech.,* **1**, 29-44.

TURNER, J. S. 1973 Buoyancy Effects in Fluids. *Cambridge University Press*.

VAN DEN BREMER, T. S. & HUNT, G. R. 2014 Two-Dimensional Planar Plumes and Fountains. *J. Fluid. Mech.*, **750**, 210-244.

VARAKSIN, A. Y., ROMASH, M. E. & KOPEITSEV, V.N. 2011 Tornado-like Non-stationary Vortices: Experimental Modelling Under Laboratory Conditions. *Natural Science*, **3**, 907-913.

WARD, N. B. 1972 The Exploration of Certain Features of Tornado Dynamics Using a Laboratory Model. *J. Atmos. Sci.*, **29**, 1194-1204.

WILSON, T., & ROTUNNO, R. 1982 Numerical Simulation of a Laminar Vortex Flow. *Comp. Meth. and Exp. Measurements*, 203-215.

WURMAN, J. & SWARNDEEP, G. 2000 Finescale Radar Observations of the Dimmitt, Texas (2 June 1995), Tornado. *Mon. Wea. Rev.*, **128**, 2135-2164.

ZHANG, M., LUO, X., TIANYU, L., MENG, X., KASE, K., WADA, S., YU, C. & GU, Z. 2015 From Dust Devil to Sustainable Swirling Wind Energy, *Scientific Reports*, **5**, 1-5.

ZHAO, Y. Z., GU, X. L., YU, Y. Z., GE, Y., LI, Y. & FENG, X. 2004 Mechanism and Large Eddy Simulation of Dust Devils *Atmos.-Ocean,* **42**, 61-84.